DCE-MRI FOR QUANTIFICATION AND SEGMENTATION OF TUMORS: REFERENCE REGION MODEL AND INDEPENDENT COMPONENT ANALYSIS

by

JOONSANG LEE

(Under the Direction of Qun Zhao)

ABSTRACT

Dynamic contrast-enhanced magnetic resonance imaging (DCE-MRI) has been widely studied as a cancer imaging tool that provides information about blood volume and microvascular permeability by tracking the exchange of contrast agent between the vascular space and extravascular extracellular space. To quantitatively analyze the DCE-MRI data, concentration of the contrast agent in the blood plasma, the so-called arterial input function (AIF), has a very important role in estimating pharmacokinetic parameters accurately. However, the AIF is usually unknown, and it remains very difficult to obtain such information noninvasively. In this study, a reference region (RR) model that does not require information of AIF is used to analyze the kinetic parameters. However, the RR model usually depends on kinetic parameters found in previous studies of a reference region and may generate errors if wrong values are assigned from previous studies for the reference region. In this work, we proposed two pharmacokinetic parameter ratios between the tissue of interest (TOI) and the reference region to overcome these problems. To more accurately analyze DCE-MRI data, an analytical approach is introduced. This analytical method can estimate parameters more accurately than numerical analysis over various SNRs and temporal resolutions.

In the studies of tumor segmentation using MR data, partial volume effect (PVE) is one of the major difficulties and may result in inaccurate segmentation results due to inherent low spatial resolution of images. In this study, we introduced the temporal independent component analysis (ICA) to solve partial volume effect (PVE) in tumor segmentation.

INDEX WORDS: Magnetic Resonance Imaging, Dynamic Contrast Enhanced MRI (DCE-MRI), Reference Region Model, Pharmacokinetic Parameter Ratio, Analytical and Numerical Analysis, Segmentation, Independent Component Analysis, Temporal ICA, Spatial ICA

DCE-MRI FOR QUANTIFICATION AND SEGMENTATION OF TUMORS: REFERENCE REGION MODEL AND INDEPENDENT COMPONENT ANALYSIS

by

JOONSANG LEE

B.S., Sangji University, S. Korea, 1998

A Dissertation Submitted to the Graduate Faculty of The University of Georgia in Partial Fulfillment of the Requirements for the Degree

DOCTOR OF PHILOSPHY

ATHENS, GEORGIA

2013

DCE-MRI FOR QUANTIFICATION AND SEGMENTATION OF TUMORS: REFERENCE REGION MODEL AND INDEPENDENT COMPONENT ANALYSIS

by

JOONSANG LEE

Major Professor: Qun Zhao

Committee: Uwe Happek
Inseok Song

Electronic Version Approved:

Maureen Grasso
Dean of the Graduate School
The University of Georgia
August 2013

DEDICATION

To my parents for their never-ending love and support

ACKNOWLEDGEMENTS

I would like to thank Dr. Qun Zhao for his guidance and support throughout my graduate studies. I would also like to express my gratitude to my dissertation advisory committee members: Dr. Uwe Happek and Dr. Inseok Song for being my committee members and taking their time. I would like to thank to Mrs Kim Mason for collecting MRI data for my research. I would like to thank my fellow graduate students: Dr. Jason Langley, Dr. William Potter, and Mr. Luning Wang for their helpful discussion on MR physics. In particular, I'd like to thank Dr. Sunbok Lee for his help and giving me a better understanding of statistics. I would also like to express my gratitude to Dr. Howard Lee and Dr. Mark "Marty" Pagel for providing me a recommendation letter and consultation. Finally, I would like to thank to the Department of Physics and Astronomy at The University of Georgia for all supports.

TABLE OF CONTENTS

Page

ACKNOWLEDGEMENTS v

LIST OF TABLES ix

LIST OF FIGURES x

CHAPTER

1 INTRODUCTION 1

1.1 References 3

2 LITERATURE REVIEW 6

2.1 Magnetic Resonance Imaging (MRI) 7

2.2 Dynamic Contrast Enhanced Magnetic Resonance Imaging (DCE-MRI) 17

2.3 Contrast Agent in MRI 17

2.4 Pharmacokinetic Modeling 18

2.5 Data Acquisition and Analysis 19

2.6 Arterial Input Function (AIF) 21

2.7 Data Analysis and Analysis 22

2.8 References 23

3 AN ANALYSIS OF THE PHARMACOKINETIC PARAMETER RATIOS IN DCE-MRI USING THE REFERENCE REGION MODEL 30

3.1 Abstract 31

3.2 Introduction 32

3.3 Theory 34
3.4 Methods 37
3.5 Results 43
3.6 Discussion 46
3.7 Acknowledgements 52
3.8 Appendix 53
3.9 References 54
4 COMPARISON OF ANALYTICAL AND NUMERICAL ANALYSIS OF THE REFERENCE REGION MODEL FOR DCE-MRI 60
4.1 Abstract 61
4.2 Introduction 62
4.3 Theory 63
4.4 Methods 65
4.5 Results 69
4.6 Discussion 76
4.7 References 78
5 TUMOR SEGMENTATION USING TEMPORAL INDEPENDENT COMPONENT ANALYSIS FOR DCE-MRI 83
5.1 Abstract 84
5.2 Introduction 85
5.3 Theory 88
5.4 Materials and Methods 89
5.5 Results 94

5.6 Discussion 98

5.6 References 102

6 CONCLUSIONS 108

6.1 An analysis of the pharmacokinetic parameter ratios in DCE-MRI 108

6.2 Analytical analysis of DCE-MRI 109

6.3 Tumor Segmentation using temporal ICA for DCE-MRI 110

LIST OF TABLES

Page

Table 3.1: Canine brain lesions analysis results of K_R and V_R 50

Table 3.2: Kruskal Wallis ANOVA Table for K_R and V_R 50

Table 3.3: KS test for K_R 51

Table 3.4: KS test for V_R 52

Table 4.1: Results of simulated dataset for K_R (Table 4.1A) and V_R (Table 4.1B), with different SNRs (in columns) and temporal resolutions (in rows) 72

Table 4.2: Results of K_R and V_R and Kruskal-Wallis test for in vivo dataset 77

Table 5.1: Segmented Area 97

Table 5.2: Overlap (%), Difference (%), and Pearson Correlations between three methods 97

Table 5.3: Pearson's correlation coefficient between two enhancing time curves 101

LIST OF FIGURES

Page

Figure 2.1: The proton spins (a) in the absence of an external magnetic filed B_0 and (b) in the presence of an external magnetic field B_0. Once B_0 is applied, the net magnetization M_0 is produced and aligned with the external magnetic filed B_0. 11

Figure 2.2: (a) The net magnetization M_0 has the same direction as the external magnetic field B_0. (b) After 90° RF pulse applied, the entire magnetization M_0 is flipped into the x-y plane, which is called a 90° flip. 12

Figure 2.3: The T1 relaxation or longitudinal relaxation curve. 15

Figure 2.4: The T2 relaxation or transverse relaxation curve. 15

Figure 2.5: A two-compartment model in DCE-MRI. $C_p(t)$ and $C_{TOI}(t)$ represent the concentration of the contrast agent in blood plasma and the tissue of interest, respectively. K^{trans} and k_{ep} represent the volume transfer constant and flux rate constant, respectively.....19

Figure 3.1: A two-compartment model diagram for the reference region model. $C_p(t)$, $C_{TOI}(t)$, and $C_{RR}(t)$ represent the concentration of the contrast agent in blood plasma, the tissue of interest and the reference region, respectively. K^{trans} and k_{ep} represent the volume transfer constant and flux rate constant, respectively. Contrast agent from the blood plasma diffuses from the intravascular space to the extravascular-extracellular space of the tissue of interest and vice versa.....35

Figure 3.2: Simulation study, where the simulated time curve for the concentration of CA in the blood plasma (C_p), TOI ($C_{t,TOI}$), and RR ($C_{t,RR}$) is displayed in (A) and the R_1 time curve converted from the simulated C_p time curve using Eq. [3.6] in (B). 38

Figure 3.3: R_1 simulation curve for the TOI, the RR and the results of fitting the RR model to simulated TOI curves, respectively. Gaussian noise is added to the simulated R_1 TOI curves at different levels, with (A) 0%, (B) 5%, and (C) 10%. 40

Figure 3.4: A plot of the ratio between K^{trans} in the TOI and in the RR calculated from the simulated data. $K^{trans,TOI}$ was extracted, while $K^{trans,RR}$ in the RR value was assigned from 0.1 to 1.0 min^{-1}. (A) The ratio K_R is 1.497 in the absence of noise, 1.340 when 5% noise was added and 1.144 when 10% noise was added. (B) The calculated ratio V_R is 2.000 without noise, 1.996 in 5% noise data and 1.995 in 10% noise data. 44

Figure 3.5: The results of the RR model fitting to data from the TOI using the five in vivo canine datasets. Each curve is plotted from one representative voxel randomly selected from the dataset. The red dot and the blue star represent the $R_{1,TOI}$ dataset and the $R_{1,RR}$ dataset, respectively, whicle the solid line indicates the $R_{1,TOI}$ model and the dotted line indicates the $R_{1,RR}$ model created by regression analysis. The r^2 values of the curves for the TOI and the RR are (A) 0.71 and 0.09, (B) 0.93 and 0.21, (C) 0.91 and 0.16, (D) 0.94 and 0.17, and (E) 0.71 and 0.03, respectively.....46

Figure 3.6: The plot for the pharmacokinetic parameter ratio between the RR and the TOI of the five canine datasets. (A) The ratio KR is between K^{trans} in the RR and the TOI. (B) The ratio V_R is between v_e in the RR and the TOI. 47

Figure 3.7: The box plot for the five canine datasets using the Kruskal-Wallis test for (a) K_R and for (b) V_R indicating the smallest observation (minimum), lower quartile (25^{th}

percentiles), the median (red horizontal line), upper quartile (75^{th} percentiles), and the largest observation (maximum). There is a significant difference between the datasets for K_R and V_R. 49

Figure 4.1: Simulated DCE-MRI data. (A) Simulated time curve for the concentration of CA in the blood plasma (C_p) of the TOI and RR, and the concentrations of CA in the TOI ($C_{t,TOI}$), and RR ($C_{t,RR}$), and (B) the R_1 time curve for TOI and RR converted from the C_p time curve.....66

Figure 4.2: The pharmacokinetic parameter ratios K_R (first column) and V_R (second column) were estimated from the simulation study as a function of various temporal sampling rates of 6 sec. (first row), 30 sec. (second row), and 60 sec. (third row) and SNR levels. The x-axis displays the SNR levels (SNR decreases from left to right), where "Inf" represents that no noise was added. The horizontal solid line labeled as "true value" represents the value used to construct the simulation. 70

Figure 4.3: Seven canine brain images with 3 cases (A, C, and D) of presumptive glioma, 2 cases (B and D) of presumptive meningloma, 1 case (E) of meningloma, and 1 case (G) of multilobulated tumor of bone. The enhanced tumor area in each case was pointed with an arrow. The presumptive diagnosis was reached based on the MRI characteristics of the lesion including anatomic location, discrete margins, singal intensity on T_1-weighted images, and enhancement pattern after administration of contrast medium. Data 1 through Data 7 in Table 4.3 correspond to Fig. 4.3A through Fig. 4.3G. (a~g) Representative R_1 curves corresponding to each canine dataset for TOI and RR (A~G). Each R_1 curve is plotted from one representative voxel randomly selected from the dataset.....74

Figure 4.4: Representative R_1 curves corresponding to each canine dataset for TOI and RR in Fig. 4.3 (A~G). Each R_1 curve is plotted from one representative voxel randomly selected from the dataset. 75

Figure 5.1: The results of each segmentation method: (a1~g1) expert's delineation segmentation, (a2~g2) spatial ICA segmentation, and (a3~g3) temporal ICA segmentation. 93

Figure 5.2: (a) Original canine brain tumor image. (b) A small frame that contains tumor and normal brain tissue. (c) a_{11} map from temporal ICA. (d) Binary map from the weighting coefficient ratio, a_{11}/a_{12}, which is bigger than 1. (e) Final segmented mask from temporal ICA. (f) a_{11} profile plot at the horizontal center of TOI showing that the values of the coefficient of tumor tissue a_{11} have high values and low values at the normal brain tissues. 95

Figure 5.3: a_{11} profile plots at the horizontal and vertical cross section of TOI for dataset 2 (a~c) and dataset 3 (d~f). It is shown that the values of a_{11} at the border between tumor and normal brain tissues increase or decrease gradually indicating that the PVE occurs at the border of tumors. 96

Figure 5.4: (a) Three enhancing curves from tumor, muscle, and normal brain tissues. (b) The scatter plot of the independent components S1 (tumor) and S2 (normal brain tissue). (c) The scatter plot of the independent components S1 and S3 (muscle tissue). 100

CHAPTER 1

INTRODUCTION

This chapter introduces the dynamic contrast enhanced magnetic resonance imaging (DCE-MRI) and describes the structure and significance of each study of this dissertation. This dissertation consists of six chapters: an introductory chapter, a literature review, three journal article style chapters, and a concluding chapter.

DCE-MRI has been widely studied as a cancer imaging tool with a low molecular weight contrast agent. DCE-MRI provides a way of tracking of these low molecular weight contrast agents through blood vessels. Angiogenesis is the physiological process in growth and development of a tumor through which new blood vessels form from pre-existing vessels. These new blood vessels in the tumor are permeable, which improves the perfusion of nutrients into the tumor. This vascular permeability in tumors can be examined by DCE-MRI (1). When a contrast agent is injected into the body, it circulates through the blood stream and then perfuses into the tumor and normal tissues. Pharmacokinetic parameters such as K^{trans} and k_{ep}, which is the rate of perfusion of the contrast agent into the tumor from capillaries (K^{trans}) and out of the tumor back to the capillaries (k_{ep}), can be estimated using DCE-MRI. By analyzing the pharmacokinetics of how the contrast agent going into a specific tumor, it is possible to measure alterations in blood flow and extracellular volumes including vascular permeability. This is very important in the development of cancer drugs that inhibit new blood vessel formation or disrupt existing blood vessels. However, there are a couple of problems in current DCE-MRI studies about accurately

estimating AIF, i.e., modeling for better estimation of the kinetic parameters, and imaging with both high temporal and spatial resolution. Among the two problems, estimating AIF is the most important issue in the current DCE-MRI studies. When analyzing DCE-MRI data to estimate the kinetic parameters, accurate knowledge of AIF is essential but it is usually unknown and it remains very difficult to obtain such information noninvasively. Several approaches have been studied to estimate accurate AIF such as measurements from the blood samples or directly estimate AIF from the DCE-MRI data itself (2). However, these approaches are still technically challenging and they present a significant source of variability in estimating physiological parameters.

An alternative approach to estimate pharmacokinetic parameters without information of AIF was introduced, based on a reference region model (3). The reference region model usually uses kinetic parameters found in previous studies of a reference region (e.g., muscle). However, both the assignment of reference region parameters and the selection of the reference region itself may confound the results obtained by the reference region model. The purpose of this study is to study tumors without pre-assignment of any pharmacokinetic parameters in the reference region. As a result, new pharmacokinetic parameter ratios, K_R and V_R, between TOI and RR, are introduced and studied both in simulation and in vivo datasets (4) to overcome this problem.

In quantification of DCE-MRI, quantitative physiological parameters can be estimated by fitting dynamic contrast-enhanced MRI data to an appropriate pharmacokinetic model (5). Numerical analysis method has long been used in the quantification of pharmacokinetic parameters (3). However, a numerical analysis usually produces systematic errors especially when temporal resolutions are low (6,7). For the goal of this study, an analytical approach on the analysis of DCE-MRI data is proposed and compared with numerical analysis to estimate

parameters without introducing systematic errors from numerical analysis. With a high sensitivity, DCE-MRI has been widely applied to improve tumor detection and diagnosis (8). In particular, tissue classification and anatomical segmentation are increasingly studied through MRI. Due to a growing amount of MRI data, an automated method is required to develop accurate and reliable image analysis for classifying image regions. As a result, several automated computer-aided methods are proposed such as the region-growing method to segment lesions (9), automated segmentation methods based on artificial intelligence techniques (10), segmentation based on statistical pattern recognition techniques (11), a semiautomatic algorithm based on the fuzzy c-means clustering (12), a user-interaction-threshold method to extract the region of interest (ROI) (13), and a detection of deviations from normal brains using a multi-layer Markov random field framework (14), etc.

In the studies of tumor segmentation using MR data, partial volume effect (PVE) is one of the major difficulties which may result in inaccurate segmentation results due to inherent low spatial resolution of images (15). PVE occurs when more than one tissue type present in a voxel and it blurs the intensity distinction at the border of two tissues such as the tumor and normal tissues. In chapter 5, in order to segment tumor and overcome PVE problem, an automated segmentation using temporal independent component analysis (ICA) is introduced and compared with spatial ICA method and an expert's manual delineation method.

1.1 References

1. Tofts PS. Modeling tracer kinetics in dynamic Gd-DTPA MR imaging. J Magn Reson Imaging 1997;7(1):91-101.
2. Benjaminsen IC, Brurberg KG, Ruud EB, Rofstad EK. Assessment of extravascular extracellular space fraction in human melanoma xenografts by DCE-MRI and kinetic modeling. Magn Reson Imaging 2008;26(2):160-70.
3. Yankeelov TE, Luci JJ, Lepage M, Li R, Debusk L, Lin PC, Price RR, Gore JC. Quantitative pharmacokinetic analysis of DCE-MRI data without an arterial input function: a reference region model. Magn Reson Imaging 2005;23(4):519-29.
4. Lee J, Platt S, Kent M, Zhao Q. An analysis of the pharmacokinetic parameter ratios in DCE-MRI using the reference region model. Magn Reson Imaging 2012;30(1):26-35.
5. Tofts PS, Brix G, Buckley DL, Evelhoch JL, Henderson E, Knopp MV, Larsson HB, Lee TY, Mayr NA, Parker GJ and others. Estimating kinetic parameters from dynamic contrast-enhanced T(1)-weighted MRI of a diffusable tracer: standardized quantities and symbols. J Magn Reson Imaging 1999;10(3):223-32.
6. Cardenas-Rodriguez J, Howison CM, Pagel MD. A linear algorithm of the reference region model for DCE-MRI is robust and relaxes requirements for temporal resolution. Magn Reson Imaging 2012.
7. Larsson C, Kleppesto M, Rasmussen I, Jr., Salo R, Vardal J, Brandal P, Bjornerud A. Sampling requirements in DCE-MRI based analysis of high grade gliomas: Simulations and clinical results. J Magn Reson Imaging 2013;37(4):818-29.
8. Renz DM, Bottcher J, Diekmann F, Poellinger A, Maurer MH, Pfeil A, Streitparth F, Collettini F, Bick U, Hamm B and others. Detection and classification of contrast-

enhancing masses by a fully automatic computer-assisted diagnosis system for breast MRI. J Magn Reson Imaging 2012;35(5):1077-88.

9. Chen W, Giger ML, Lan L, Bick U. Computerized interpretation of breast MRI: investigation of enhancement-variance dynamics. Med Phys 2004;31(5):1076-82.

10. Clark MC, Hall LO, Goldgof DB, Velthuizen R, Murtagh FR, Silbiger MS. Automatic tumor segmentation using knowledge-based techniques. IEEE Trans Med Imaging 1998;17(2):187-201.

11. Kaus MR, Warfield SK, Nabavi A, Chatzidakis E, Black PM, Jolesz FA, Kikinis R. Segmentation of meningiomas and low grade gliomas in MRI. Medical Image Computing and Computer-Assisted Intervention, Miccai'99, Proceedings 1999;1679:1-10.

12. Chen W, Giger ML, Bick U. A fuzzy c-means (FCM)-based approach for computerized segmentation of breast lesions in dynamic contrast-enhanced MR images. Acad Radiol 2006;13(1):63-72.

13. Liney GP, Sreenivas M, Gibbs P, Garcia-Alvarez R, Turnbull LW. Breast lesion analysis of shape technique: semiautomated vs. manual morphological description. J Magn Reson Imaging 2006;23(4):493-8.

14. Gerig G, Styner M, Chakos M, Lieberman JA. Hippocampal shape alterations in schizophrenia: Results of a new methodology. Schizophrenia Research 2002;53(3):102-103.

15. Kumazawa S, Yoshiura T, Honda H, Toyofuku F, Higashida Y. Partial volume estimation and segmentation of brain tissue based on diffusion tensor MRI. Med Phys 2010;37(4):1482-90.

16. Kozlowski P, Chang SD, Jones EC, Berean KW, Chen H, Goldenberg SL. Combined diffusion-weighted and dynamic contrast-enhanced MRI for prostate cancer diagnosis--correlation with biopsy and histopathology. J Magn Reson Imaging 2006;24(1):108-13.

CHAPTER 2

LITERATURE REVIEW

2.1 Magnetic Resonance Imaging (MRI)

MRI stands for magnetic resonance imaging that is a medical imaging technique using a powerful magnetic field, radio frequency pulses, and a computer to visualize detailed internal body structures such as organs, soft tissues, blood vessels, and bones. Different from ultrasound scan, computed tomography (CT), and CAT scanning, MRI does not use a sound wave or x-ray but still can provide us with much higher detail in the soft tissues. MR images allow physicians to better evaluate various parts of the body and determine the presence of certain diseases or monitor treatment for conditions such as brain tumors (1), lung cancers (2), certain types of heart problems (3), diseases of the liver (4), diseases of the kidney (5) breast cancer and implants (6) fetal assessment in pregnant women (7), etc. The benefits of an MRI scan, which is a noninvasive, clinical imaging technique, relate to its high accuracy in detecting structural abnormalities of the body without known side effects.

For MRI studies, there are various methods that provide additional information. Some specialized MRI techniques include, but are not limited to, diffusion MRI, DCE-MRI, functional MRI (fMRI), magnetic resonance angiography (MRA), and magnetic resonance spectroscopy (MRS). Diffusion MRI is a method that allows mapping of diffusion process of molecules, generally water molecules, in biological tissues. It provides information of the microstructure of the tissue either in a normal or an abnormal state. This method has been used primarily with

brain pathology. DCE-MRI is a noninvasive, clinical imaging technique that uses a continuous series of images taken before, during and after injection of low molecular weight contrast agent (CA) and provides the tracking of a CA through blood vessels. It is applied to access the microvascular status of tumor tissue and characterize tumor response to antiangiogenic treatment. fMRI is another type of MRI technique that can be used to study the change in blood flow related to neural activity in the brain. It allows us to detect brain areas that are involved in a process, a task, or an emotion. In addition to the anatomical information, fMRI provides information about biological function by measuring the blood-oxygenation-level-dependent (BOLD) signal. MRA is a type of MRI scan that can image blood vessels. It is used to generate images of the arteries in or near the brain, neck, abdomen, or legs and find the problems with the blood vessels that may be causing reduced blood flow. MRS is used to measure the levels of different metabolites in body tissues.

In 1820, Hans Christian Oersted (1777-1851 Danish) discovered that electric currents create magnetic fields (8). He demonstrated that a compass needle deflected from magnetic north when a wire carrying an electric current. There are two sources that magnetism arises. One is from moving electric charges and the other is from nonzero intrinsic magnetic moments in many particles. When some materials or substances placed in a magnetic field, they get magnetized with various degree of magnification. This degree refers to the magnetic susceptibility of a substance, which is a measure of how magnetized they get, and it is defined as

$$\chi = \frac{M}{H}, \text{ or } M = \chi H \qquad [2.1]$$

where M is the magnetization of the substance and H is the magnetic field strength. Some materials with unpaired electrons will have a net magnetic field and will react more to an external field. In MRI, there are three different types of substances, paramagnetism,

diamagnetism, and ferromagnetism, which have different magnetic susceptibility. Paramagnetic materials are attracted to external magnetic fields and have a small, positive susceptibility. When the external field is removed, paramagnetic material does not retain the magnetic properties. Diamagnetic materials are slightly repelled by a magnetic field and have a weak, negative susceptibility to magnetic fields. Also, it does not retain the magnetic properties when the external field is removed. Diamagnetic materials have no unpaired orbital electrons while paramagnetic materials have unpaired orbital electrons. Ferromagnetic materials are strongly attracted by a magnetic field and have a large positive susceptibility. Ferromagnetic materials retain the magnetic properties even when the external field is removed.

In 1922, O. Stern (1888-1969 German) and W. Gerlach (1889-1979 German) performed an experiment, called Stern-Gerlach experiment, on the deflection of particle that is often used to illustrate basic principle of quantum mechanics (9). In the Stern-Gerlach experiment, a beam of silver (Ag) atoms was sent through an inhomogeneous magnetic field produced by a pair of pole pieces, and meanwhile their deflection was observed. The intrinsic angular momentum of the silver atom is associated a magnetic moment, proportional to the spin. The observation showed that the silver atoms were deflected upwards or downwards, according to the component of their spin. This demonstrates that particles possess an intrinsic angular momentum that takes only certain quantized values. In MRI, all tissues are made up of atoms with nuclei containing protons and neutrons. The atoms are characterized by the atomic number and the mass number. Atomic number is the number of protons in the nucleus of an atom and the mass number is the total number of protons and neutrons in the nucleus. Normally, the number of neutrons and protons in a nucleus are balanced so that the mass number is an even number but in some case, there are slightly more or fewer neutrons than protons. These atoms are called isotopes and they result in

an odd mass number, which is important in MRI. In general, hydrogen turns out to be the most important element for MRI because of its nuclear properties that it consists of a single proton, and has a significant magnetic moment, and because of its abundance in the human body.

In 1929, Isidor Rabi (1898-1988 American) began studying the magnetic properties of atomic nuclei, and further developed Stern's molecular beam method to great precision for the nuclear spin of atoms, including hydrogen and deuterium (10). Magnetic moments tend to align either parallel or antiparallel to an external magnetic field and precess about the direction of the magnetic field with a frequency that depends on the magnetic field strength and the atom's nuclear magnetic moment. In quantum theory, atomic nuclei have specific energy levels related to spin quantum number S. In hydrogen, a proton has two energy states, which aligned in opposite directions, i.e., -½ and ½. They can generate a net magnetic field or a magnetic dipole moment to the nucleus when unpaired proton exists (i.e., odd number of protons), and they are spinning about their axis. Each of those nuclei with an odd number of protons can be used for MRI. The ratio between the angular momentum and the magnetic moment gives us a constant known as the gyromagnetic ratio (in unit of rad $s^{-1}T^{-1}$), which is specific to each magnetically active nucleus.

In 1937, Rabi predicted that the magnetic moments of nuclei could be induced to flip their orientation if they absorbed energy from an electromagnetic wave of the same frequency, and they can also emit this amount of energy if falling back to the lower energy orientation. In 1938, Rabi observed the first magnetic resonance absorption with beam of lithium chloride molecules (11). This magnetic resonance method became the basis for magnetic resonance imaging.

In 1946, Felix Bloch (1905-1983 Swiss) and Edward Purcell discovered the magnetic resonance phenomena independently and were awarded the Nobel Prize in 1952. They found that certain nuclei absorbed energy when they were placed in a magnetic field and emit this energy when the nuclei returned to their original equilibrium state (12,13). Purcell's group used a two-pound block of paraffin wax as their hydrogen source, while Bloch's group used a few drops of water contained in a glass sphere for their experiments. Their experiments demonstrated what is technically known as nuclear magnetic resonance in condensed matter as distinguished from Rabi's discovery of molecular beam magnetic resonance.

In order to perform MRI, we first need a strong external magnetic field B_0 (in unit of Tesla). Once a subject or patient lies on a scanning table in a magnetic field B_0, unpaired spinning protons in the body will line up with this magnetic filed B_0. For a proton, there are two possible spin energy states in an external magnetic filed, spin-up and spin-down. At thermal equilibrium under a normal room temperature, there are slightly more spins in the lower state. This small portion of property produces the net magnetization M_0 in the direction of B_0 (Figure 2.1).

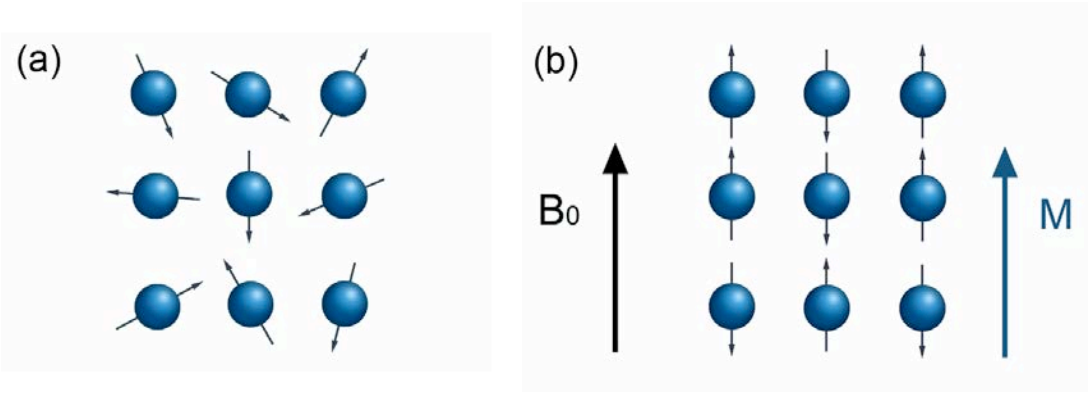

Figure 2.1 The proton spins (a) in the absence of an external magnetic filed B_0 and (b) in the presence of an external magnetic field B_0. Once B_0 is applied, the net magnetization M_0 is produced and aligned with the external magnetic filed B_0.

In order to observe the net effect of the magnetization M_0, we need to introduce radio frequency (RF) field B_1 to excite the spins. In MRI, an RF pulse need to be applied perpendicular to B_0 and applied at the resonant frequency of the spins. When an RF pulse is applied into the patient in a specific frequency, then some spins will change their alignment. As a result, in the rotating frame at this frequency, M_0 will move towards the transverse plane (x-y plane) as shown in Figure 2.2.

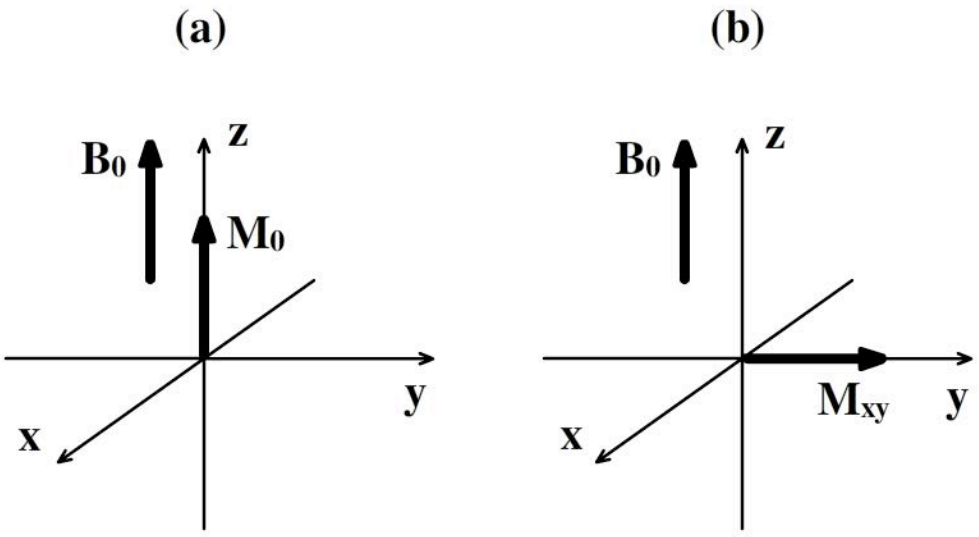

Figure 2.2 (a) The net magnetization M_0 has the same direction as the external magnetic field B_0. (b) After 90° RF pulse applied, the entire magnetization M_0 is flipped into the x-y plane, which is called a 90° flip.

The RF pulse is applied at a specific frequency, referred to as Larmor frequency, which is the same as the precessional frequency of proton. The Larmor frequency is proportional to the external magnetic field and given as Eq. [2.2],

$$\omega = \gamma B_0 \qquad [2.2]$$

where ω is an angular frequency of proton, γ is a gyromagnetic ratio, and B_0 is the external magnetic field. After the RF pulse is turned off, the magnetization will return to their original alignment (z-direction) from the x-y plane. The time from a non-equilibrium state to the equilibrium state is called relaxation time and there are two different types of relaxation times corresponding to the recovery of the z component and x-y component of the magnetization. T_1 relaxation involves recovery of the z component of the magnetization while T_2 relaxation involves decay of a coherence of the transverse nuclear spin magnetization.

In 1950, Erwin L. Hahn (1921- American) discovered spin-echo effect that is the refocusing of spin magnetization by a pulse of resonant electromagnetic radiation, and further developed a method to study molecular diffusion in liquids by the spin-echo method (14). In 1971, Raymond Damadian (1936- American) measured T_1 and T_2 relaxation times of normal and cancerous tissue and found that tumor and normal tissue can be distinguished by their different relaxation time.

The magnetization $\boldsymbol{M}$ as a function of time can be calculated with the longitudinal relaxation time, denoted by T_1 which is the decay constant for the recovery of the z component of the proton spin magnetization, M_z, and the transverse relaxation time denoted by T_2, the x-y component of the magnetization, M_{xy} (or $M_\perp$). This can be expressed as a Bloch equation,

$$\frac{d\boldsymbol{M}(t)}{dt} = \boldsymbol{M}(t) \times \gamma \boldsymbol{B}(t) - \frac{M_\perp(t)}{T_2} - \frac{M_z(t) - M_0}{T_1}\hat{z} \qquad [2.3]$$

where $\boldsymbol{M}(t)=(M_x\ (\mathrm{t}),\ M_y\ (\mathrm{t}),\ M_z(\mathrm{t}))$, $\boldsymbol{B}(t)=(B_x(t),\ B_y(t),\ B_0+\Delta B_z(t))$, and $M_\perp=(M_x,\ M_y)$. It is noted that this Bloch equation is not for describing the equation of motion of individual nuclear magnetic moments. It is a macroscopic equation that describes the motion of macroscopic nuclear magnetization obtained in the bulk sample.

For the longitudinal relaxation, the magnetization, M_z, can be calculated by following equation:

$$M_z(t) = M_0 - \left(M_0 - M_z(0)\right)e^{-t/T_1} \quad [2.4]$$

For the case of a 90°-flip (i.e., when **M** has been tilted into the x-y plane, $M_z(0)=0$),

$$M_z(t) = M_0\left(1 - e^{-t/T_1}\right) \quad [2.5]$$

The T_1 relaxation time is also called spin-lattice relaxation time, which is the time it takes for the longitudinal magnetization to recover about 63% of its initial value after being flipped into the x-y plane (Figure 2.3). Different tissues have different T_1 values. For instance, water based tissues are in the 400~1200 ms range and fat based tissues are in the 100~150 ms range.

For the transverse relaxation, the magnetization, M_{xy}, can be calculated by following equation:

$$M_{xy}(t) = M_{xy}(0)e^{-t/T_2} \quad [2.6]$$

The T_2 relaxation time is also called transverse relaxation time or spin-spin relaxation time, which is the time it takes for the transverse component of the magnetization to reach about 37% of its initial value after being flipped into the transverse plane (Figure 2.4). The T_2 relaxation results from an intrinsic process that corresponds to a decoherence of the transverse nuclear spin magnetization. In real MRI experiment, the transverse magnetization decays much faster due to inhomogeneities in the main external magnetic field B_0. The external magnetic field inhomogeneity makes protons in different locations precess at different frequencies and these small differences in frequency result in spin dephasing. This relaxation rate can be denoted by T_2^* and written by

$$\frac{1}{T_2^*} = \frac{1}{T_2} + \frac{1}{T_2'} \quad [2.7]$$

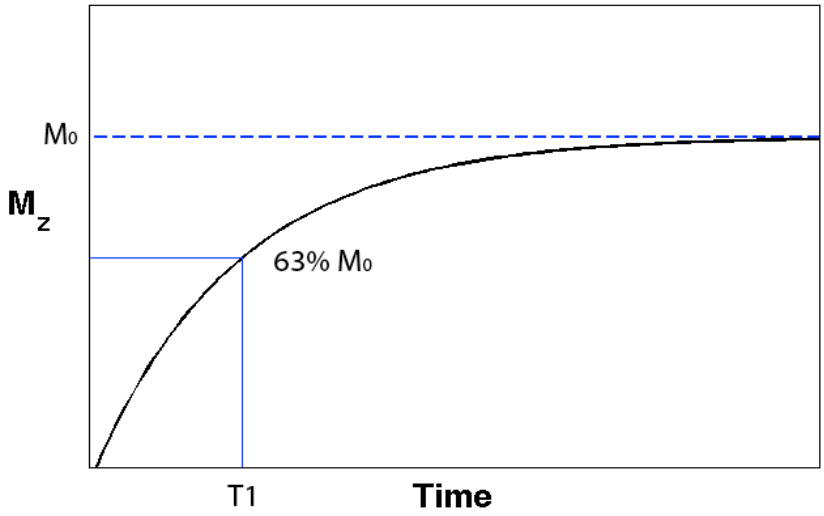

Figure 2.3 The T1 relaxation or longitudinal relaxation curve.

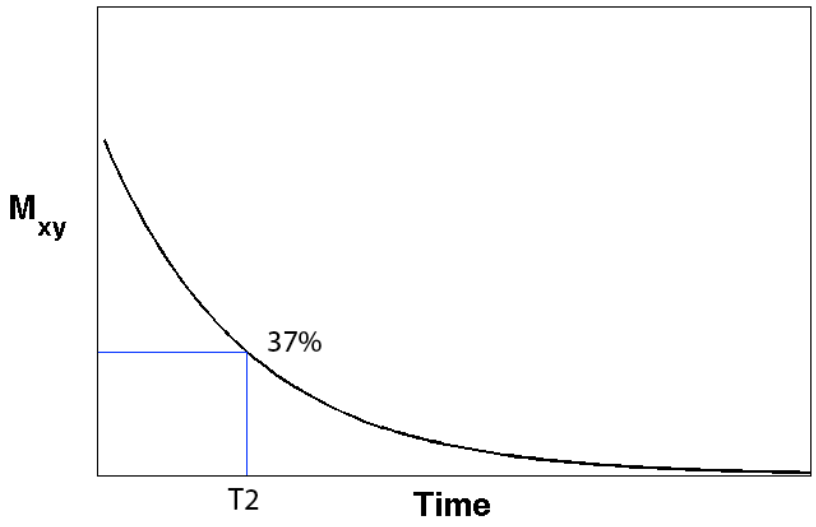

Figure 2.4 The T2 relaxation or transverse relaxation curve.

where $1/T_2'$ represents the relaxation rate due to magnetic field inhomogeneities. After the RF transmitter is turned off, the signal vector is continuously decaying in magnitude as it is precessing around the x-y plane and the net magnetization returns to equilibrium. This process is called a free induction decay (FID).

So far, we have discussed the concept of dephasing with a single RF pulse. In distinction to the FID with a single RF pulse, we will talk about a spin echo (SE), which is the refocusing of spin magnetization by an additional 180° RF pulse. The first 90° RF pulse flips the spins into the x-y plane and generates an FID signal. The FID will rapidly diphase due to the T_2^* effect. If we apply a second 180° RF pulse at time τ after the first pulse, the magnetic resonance signal will reappear at time 2τ as a spin echo. We call 2τ the echo delay time or time to echo (TE) and the 180° RF pulse is called a refocusing or rephrasing pulse.

In the 1970s, Paul C. Lauterbur (1929-2007 American) contributed to the development of MRI by introducing gradients in the magnetic field that allows for determining the origin of the radio waves emitted from the nuclei of the object. This spatial information is encoded to make two-dimensional images. Spatial encoding uses magnetic field gradients in x, y and z direction to obtain spatial information in that direction. Depending on their orientation axis they are called the slice-select gradient, the frequency-encoding gradient, and the phase-encoding gradient. This effect is achieved by using a gradient coil that produces magnetic field that varies over the volume of the object in a linear manner.

In 1975, Richard Ernst described the use of Fourier transform of phase and frequency encoding to reconstruct 2D images. Fourier transform is a fundamental mathematic tool widely used in signal analysis including MR image formation. Joseph Fourier (1768-1830 French) initiate the investigation of Fourier series and Fourier transform was named in his honor. In MRI,

Fourier transform converts the signal from the time domain to the spatial-frequency domain. Basically, the Fourier transform represents a function in the frequency domain whose amplitude varies with the frequencies present in the signal. This technique is the basis of today's MRI.

2.2 Dynamic Contrast-Enhanced Magnetic Resonance Imaging (DCE-MRI)

Recent molecular understanding of the processes of tumor development and metastasis has led to a number of new targets being identified for potential anti-cancer treatments (15). DCE-MRI techniques combines the use of low molecular contrast media with optimized image acquisition techniques. DCE-MRI has been widely studied as a cancer imaging tool, which is a noninvasive, clinical imaging technique that is applied to access the microvascular status of tumor tissue and characterize tumor response to antiangiogenic treatment (16,17). DCE-MRI is performed by obtaining sequential MRI images before, during, and after the injection of a contrast agent. Basically, DCE-MRI provides the tracking of a contrast agent between the vascular space and extravascular extracellular space (EES), and provides information about blood volume and microvascular permeability.

2.3 Contrast Agent in MRI

The contrast agents in MRI are a group of contrast media used to improve the visibility of internal body structures in MR images. There are two different types of contrast agents based on the effect on the values of T_1 and T_2. The most commonly used T_1-based compounds for contrast enhancement are gadolinuium diethylene triamine pentaacetate (Gd-DTPA). The characteristics of Gd-DTPA was described and introduced as the first Gadolinium-based contrast agent in MRI in 1987 (18). It is a paramagnetic low molecular weight contrast agent that increases the intensity

of the tissue on T_1-weighted MR images. In general, gadolinium-based contrast media are used to shorten T_1 relaxation time of protons located nearby. Different Gd-based compounds have different tumbling rates affecting the T_1 relaxation rate. This is referred to as the relaxivity of the contrast agent and measured in unit of $mM^{-1}s^{-1}$. Normally, Gd-DTPA has longitudinal relaxivity values in plasma of around 4 $mM^{-1}s^{-1}$ at 1.5 T (19). The most commonly used T_2-based contrast agents are superparamagnetic iron oxide nanoparticles that have a much higher T_2 relaxation rate than T_1-based contrast agents. This contrast agents increase the T_2 relaxation rate and best used with T_2 weighted imaging.

2.4 Pharmacokinetic Modeling

Pharmacokinetics models are simple mathematical schemes that represent the mechanisms of absorption and distribution of an administered drug or agent. The most commonly used pharmacokinetic models are the one-compartment model and two-compartment model developed by Tofts. In addition to Tofts model (20,21), several other models are also available (20,22,23). It was investigated which model can be used in a clinical setting by simulating a range of sampling rates and noise levels. For a one-compartment model, all drugs initially distribute into a central compartment before distributing into the peripheral compartment. One-compartment model can use only one volume term, the apparent volume of distribution, if a drug rapidly equilibrates throughout the tissue compartment.

The most widely used model in DCE-MRI is the two-compartment model, which uses pharmacokinetic parameters to describe the exchange of contrast agent between the blood plasma and the extravascular extracellular space (EES) (24). A simple two-compartment model is shown

in Figure 2.5. In this model, contrast agent diffuses from the blood plasma into EES for the tissue of interest (TOI).

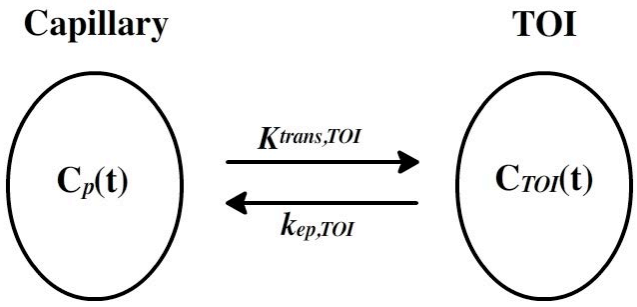

Figure 2.5 A two-compartment model in DCE-MRI. $C_p(t)$ and $C_{TOI}(t)$ represent the concentration of the contrast agent in blood plasma and the tissue of interest, respectively. K^{trans} and k_{ep} represent the volume transfer constant and flux rate constant, respectively.

Pharmacokinetic parameters can be estimated from DCE-MRI data using a differential equation for this two-compartment model defined and standardized by Tofts:

$$\frac{dC_t}{dt} = K^{trans}C_p - k_{ep}C_t \qquad [2.8]$$

where C_t and C_p are the concentration of the contrast agent in the EES and plasma space, respectively, and K^{trans} and k_{ep} represent the volume transfer constant and flux rate constant, respectively.

2.5 Data Acquisition and Analysis

DCE-MRI relies on MRI sequences and is obtained before, during, and after the rapid intravenous administration of a contrast agent. Each image acquired corresponds to one time

point, and each pixel in each image set gives rise to its own time course. DCE-MRI is aimed at investigating such contrast agent effects over time. The pharmacokinetic parameters and intrinsic tissue properties may be extracted by fitting these time courses. The first step of quantitative DCE-MRI data acquisitions is to obtain a map of the native T_1 before administration of the contrast agent. In a multiple flip angles method, the signal intensity as a function of the flip angle is given by

$$S = S_0 \left(\frac{\sin\theta\left(1 - e^{-TR/T_1}\right)e^{-TE/T_2^*}}{\cos\theta\left(1 - e^{-TR/T_1}\right)} \right) \qquad [2.9]$$

where θ is the flip angle, S_0 is a constant describing the proton density, TR is the repetition time, TE is the echo time, and T_2^* is the transverse relaxation time due to both molecular interactions and inhomogeneities in the external magnetic field. In general, TE << T_2^* so that the final exponential term can be approached to 1. The Multiple flip angles method can be used for obtaining a map of T_1 before administering the contrast agent. Alternatively, a pre-contrast T_1 map can be obtained using gradient or spin echo images obtained by multiple repetition times (25). Once the pre-contrast T_1 map is acquired, dynamic T_1-weighted images need to be acquired before and after the administration of the contrast agent.

The two-compartment model in pharmacokinetics is the most widely used model in DCE-MRI to estimate pharmacokinetic parameters such as blood volume and permeability that are associated with tumors (20,26). In this model, it is commonly assumed that within each compartment, capillory and tissue of interest, the contrast agent is homogeneously distributed (27). Pharmacokinetic parameters such as K^{trans} and k_{ep} can be estimated by Eq. [2.8]. K^{trans} is the volume transfer constant representing diffusion of the contrast agent from capillaries to the TOI. Similarly, k_{ep} is the flux rate constants from the TOI back to the capillaries.

2.6 Arterial Input Function (AIF)

To estimate the kinetic parameters derived from the pharmacokinetic model, accurate knowledge of concentration of the contrast agent in the blood plasma as a function of time, $C_p(t)$, is very important. The $C_p(t)$ is also known as the arterial input function (AIF). However, the AIF is usually unknown, and it remains very difficult to obtain such information noninvasively.

In general, there are three approaches to estimate the AIF in DCE-MRI. The first approach is the sampling method using an arterial catheter, which involves sampling blood during the imaging process (29,30). There is an advantage and disadvantage of this approach. The advantage of this sampling method is that the AIF obtained by each arterial blood sample can be estimated from standard chemical analytic method allowing for very accurate characterization of the AIF. However, there are disadvantages due to its invasive nature, poor temporal resolution, and inaccurate drawn blood sampling time. A second approach uses an averaged AIF from the small cohort of subjects using the blood sampling method and then uses this averaged AIF for subsequent studies by assuming that the AIF is similar for all subjects (31,32). Since this method uses an averaged AIF for all subjects, it is very simple in both data acquisition and data analysis. However, this approach has a disadvantage of the influences of both inter- and intra-subject variations in AIF that may introduce large errors in AIF characterization and pharmacokinetic analysis (32). A third approach is that the AIF can be estimated directly from the DCE-MRI data and several studies for this approach have been proposed (33,34). These methods have advantages of measuring the AIF on an individual basis and it is completely noninvasive. However, it requires the presence of a large vessel within the field of view (FOV). Also, determining the AIF can be technically challenging, and can be a significant source of variability in the physiological parameters estimated from DCE-MRI

results. In addition to these approaches to estimate accurate AIF, as an alternative approach, there is a reference region (RR) model that does not require the AIF and instead uses the concentration of the CA in the reference region, such as muscle, to estimate pharmacokinetic parameters (27,35). Without knowledge of the AIF, reference region (RR) model can be applied by using literature values for the reference region to analyze the kinetic parameters. However, this method has a systematic error in estimating the kinetic parameters caused by incorrect assignments of the parameters for the reference regions. To overcome this problem, new pharmacokinetic parameter ratios, K_R and V_R, between TOI and RR can be used for the reference region model without the information about the AIF (36).

2.7 Applications of DCE-MRI

DCE-MRI can be used to assess treatment response of angiogenesis inhibitors that involves the study of tumor angiogenesis (37) and in the development and trial assessment of antiangiogenic and vascular disrupting compounds (38). Also, the studies of DCE-MRI includes, but are not limited to, noninvasive assessment of tumor microenvironment (39), predictors of clinical outcomes including treatment response to chemotherapy (40,41), detection of rheumatoid arthritis (42,43), differentiation of tumor histopathology (44,45), and analysis of the pharmacokinetic parameters (36). There are several DCE-MRI studies combined with other imaging techniques. Recently, the studies have shown that DCE-MRI with fluorodeoxyglucose positron emission tomography computed tomography (FDG-PET/CT) could assess the evaluation of response to chemotherapy with bevacizumab (46).

Combination of the diffusion weighted imaging (DWI) and DCE-MRI provides higher sensitivity in diagnosing prostate cancer than either technique alone (47). Also, DCE-MRI with

diffusion tensor imaging (DTI) has been studied to improve accuracy in prostate cancer diagnosis (48).

2.8 References

1. Jia Z, Geng D, Xie T, Zhang J, Liu Y. Quantitative analysis of neovascular permeability in glioma by dynamic contrast-enhanced MR imaging. J Clin Neurosci 2012;19(6):820-3.
2. Kelly RJ, Rajan A, Force J, Lopez-Chavez A, Keen C, Cao L, Yu Y, Choyke P, Turkbey B, Raffeld M and others. Evaluation of KRAS mutations, angiogenic biomarkers, and DCE-MRI in patients with advanced non-small-cell lung cancer receiving sorafenib. Clin Cancer Res 2011;17(5):1190-9.
3. Biglands J, Magee D, Boyle R, Larghat A, Plein S, Radjenovic A. Evaluation of the effect of myocardial segmentation errors on myocardial blood flow estimates from DCE-MRI. Phys Med Biol 2011;56(8):2423-43.
4. Saito K, Ledsam J, Sourbron S, Otaka J, Araki Y, Akata S, Tokuuye K. Assessing liver function using dynamic Gd-EOB-DTPA-enhanced MRI with a standard 5-phase imaging protocol. J Magn Reson Imaging 2012.
5. Lietzmann F, Zollner FG, Attenberger UI, Haneder S, Michaely HJ, Schad LR. DCE-MRI of the human kidney using BLADE: a feasibility study in healthy volunteers. J Magn Reson Imaging 2012;35(4):868-74.
6. Schmidt MA, Borri M, Scurr E, Ertas G, Payne G, O'Flynn E, Desouza N, Leach MO. Breast dynamic contrast-enhanced examinations with fat suppression: Are contrast-agent uptake curves affected by magnetic field inhomogeneity? Eur Radiol 2012.

7. Anblagan D, Deshpande R, Jones NW, Costigan C, Bugg G, Raine Fenning N, Gowland PA, Mansell P. Measurement of Fetal Fat in Utero in Normal and Diabetic Pregnancy using Magnetic Resonance Imaging. Ultrasound Obstet Gynecol 2013.
8. Ørsted HC. Electricity and magnetic needles. Philosophy 1820;16(4):273-276.
9. Gerlach W, Stern O. Das magnetische moment des silberatoms. Zeitschrift für Physik A Hadrons and Nuclei 1922;9(1):353-355.
10. Rabi I. Refraction of beams of molecules. Nature 1929;123:163-164.
11. Rabi I, Millman S, Kusch P, Zacharias J. The Molecular Beam Resonance Method for Measuring Nuclear Magnetic Moments. Phys. Rev 1938;53(495):318.
12. Bloch FH, W.; Packard, M.;. Nuclear infraction. Phys rev 1946;69:127.
13. Purcell ET, H.; Pound, R.;. Resonance absorption by nuclear magnetic moments in a solid. Phys rev 1946;69:37-8.
14. Hahn EL. Spin Echoes. Physical Review 1950;80(4):580-594.
15. Buolamwini JK. Novel anticancer drug discovery. Curr Opin Chem Biol 1999;3(4):500-9.
16. Padhani AR, Leach MO. Antivascular cancer treatments: functional assessments by dynamic contrast-enhanced magnetic resonance imaging. Abdom Imaging 2005;30(3):324-41.
17. Miller JC, Pien HH, Sahani D, Sorensen AG, Thrall JH. Imaging angiogenesis: applications and potential for drug development. J Natl Cancer Inst 2005;97(3):172-87.
18. Weinmann HJ, Brasch RC, Press WR, Wesbey GE. Characteristics of Gadolinium-Dtpa Complex - a Potential Nmr Contrast Agent. American Journal of Roentgenology 1984;142(3):619-624.

19. Rohrer M, Bauer H, Mintorovitch J, Requardt M, Weinmann HJ. Comparison of magnetic properties of MRI contrast media solutions at different magnetic field strengths. Invest Radiol 2005;40(11):715-724.

20. Tofts PS, Brix G, Buckley DL, Evelhoch JL, Henderson E, Knopp MV, Larsson HB, Lee TY, Mayr NA, Parker GJ and others. Estimating kinetic parameters from dynamic contrast-enhanced T(1)-weighted MRI of a diffusable tracer: standardized quantities and symbols. J Magn Reson Imaging 1999;10(3):223-32.

21. Tofts PS, Kermode AG. Measurement of the blood-brain barrier permeability and leakage space using dynamic MR imaging. 1. Fundamental concepts. Magn Reson Med 1991;17(2):357-67.

22. Kety SS. The theory and applications of the exchange of inert gas at the lungs and tissues. Pharmacological Reviews 1951;3(1):1-41.

23. Brix G, Semmler W, Port R, Schad LR, Layer G, Lorenz WJ. Pharmacokinetic parameters in CNS Gd-DTPA enhanced MR imaging. J Comput Assist Tomogr 1991;15(4):621-8.

24. Tofts PS. Modeling tracer kinetics in dynamic Gd-DTPA MR imaging. J Magn Reson Imaging 1997;7(1):91-101.

25. Gossmann A, Helbich TH, Kuriyama N, Ostrowitzki S, Roberts TP, Shames DM, van Bruggen N, Wendland MF, Israel MA, Brasch RC. Dynamic contrast-enhanced magnetic resonance imaging as a surrogate marker of tumor response to anti-angiogenic therapy in a xenograft model of glioblastoma multiforme. J Magn Reson Imaging 2002;15(3):233-40.

26. Tofts PS, Kermode AG. Measurement of the Blood-Brain-Barrier Permeability and Leakage Space Using Dynamic Mr Imaging .1. Fundamental-Concepts. Magnetic Resonance in Medicine 1991;17(2):357-367.

27. Yankeelov TE, Luci JJ, Lepage M, Li R, Debusk L, Lin PC, Price RR, Gore JC. Quantitative pharmacokinetic analysis of DCE-MRI data without an arterial input function: a reference region model. Magn Reson Imaging 2005;23(4):519-29.

28. Aad G, Abbott B, Abdallah J, Abdel Khalek S, Abdelalim AA, Abdesselam A, Abdinov O, Abi B, Abolins M, Abouzeid OS and others. Search for Pair Production of a New b^{'} Quark that Decays into a Z Boson and a Bottom Quark with the ATLAS Detector. Physical Review Letters 2012;109(7):071801.

29. Larsson HB, Stubgaard M, Frederiksen JL, Jensen M, Henriksen O, Paulson OB. Quantitation of blood-brain barrier defect by magnetic resonance imaging and gadolinium-DTPA in patients with multiple sclerosis and brain tumors. Magn Reson Med 1990;16(1):117-31.

30. Fritz-Hansen T, Rostrup E, Larsson HB, Sondergaard L, Ring P, Henriksen O. Measurement of the arterial concentration of Gd-DTPA using MRI: a step toward quantitative perfusion imaging. Magn Reson Med 1996;36(2):225-31.

31. Weinmann HJ, Laniado M, Mutzel W. Pharmacokinetics of GdDTPA/dimeglumine after intravenous injection into healthy volunteers. Physiol Chem Phys Med NMR 1984;16(2):167-72.

32. Simpson NE, Evelhoch JL. Deuterium NMR tissue perfusion measurements using the tracer uptake approach: II. Comparison with microspheres in tumors. Magn Reson Med 1999;42(2):240-7.

33. Rijpkema M, Kaanders JH, Joosten FB, van der Kogel AJ, Heerschap A. Method for quantitative mapping of dynamic MRI contrast agent uptake in human tumors. J Magn Reson Imaging 2001;14(4):457-63.

34. van Osch MJ, Vonken EJ, Viergever MA, van der Grond J, Bakker CJ. Measuring the arterial input function with gradient echo sequences. Magn Reson Med 2003;49(6):1067-76.

35. Yang C, Karczmar GS, Medved M, Stadler WM. Estimating the arterial input function using two reference tissues in dynamic contrast-enhanced MRI studies: fundamental concepts and simulations. Magn Reson Med 2004;52(5):1110-7.

36. Lee J, Platt S, Kent M, Zhao Q. An analysis of the pharmacokinetic parameter ratios in DCE-MRI using the reference region model. Magn Reson Imaging 2012;30(1):26-35.

37. Zwick S, Strecker R, Kiselev V, Gall P, Huppert J, Palmowski M, Lederle W, Woenne EC, Hengerer A, Taupitz M and others. Assessment of vascular remodeling under antiangiogenic therapy using DCE-MRI and vessel size imaging. J Magn Reson Imaging 2009;29(5):1125-33.

38. O'Connor JP, Jackson A, Parker GJ, Jayson GC. DCE-MRI biomarkers in the clinical evaluation of antiangiogenic and vascular disrupting agents. Br J Cancer 2007;96(2):189-95.

39. Jansen JF, Schoder H, Lee NY, Wang Y, Pfister DG, Fury MG, Stambuk HE, Humm JL, Koutcher JA, Shukla-Dave A. Noninvasive assessment of tumor microenvironment using dynamic contrast-enhanced magnetic resonance imaging and 18F-fluoromisonidazole positron emission tomography imaging in neck nodal metastases. Int J Radiat Oncol Biol Phys 2010;77(5):1403-10.

40. Evelhoch J, Garwood M, Vigneron D, Knopp M, Sullivan D, Menkens A, Clarke L, Liu G. Expanding the use of magnetic resonance in the assessment of tumor response to therapy: workshop report. Cancer Res 2005;65(16):7041-4.

41. Ahmed A, Gibbs P, Pickles M, Turnbull L. Texture analysis in assessment and prediction of chemotherapy response in breast cancer. J Magn Reson Imaging 2012.

42. Workie DW, Dardzinski BJ, Graham TB, Laor T, Bommer WA, O'Brien KJ. Quantification of dynamic contrast-enhanced MR imaging of the knee in children with juvenile rheumatoid arthritis based on pharmacokinetic modeling. Magn Reson Imaging 2004;22(9):1201-10.

43. Li X, Yu A, Virayavanich W, Noworolski SM, Link TM, Imboden J. Quantitative characterization of bone marrow edema pattern in rheumatoid arthritis using 3 Tesla MRI. J Magn Reson Imaging 2012;35(1):211-7.

44. Zhao Q, Lee S, Kent M, Schatzberg S, Platt S. Dynamic contrast-enhanced magnetic resonance imaging of canine brain tumors. Vet Radiol Ultrasound 2010;51(2):122-9.

45. Selnaes KM, Heerschap A, Jensen LR, Tessem MB, Schweder GJ, Goa PE, Viset T, Angelsen A, Gribbestad IS. Peripheral zone prostate cancer localization by multiparametric magnetic resonance at 3 T: unbiased cancer identification by matching to histopathology. Invest Radiol 2012;47(11):624-33.

46. De Bruyne S, Van Damme N, Smeets P, Ferdinande L, Ceelen W, Mertens J, Van de Wiele C, Troisi R, Libbrecht L, Laurent S and others. Value of DCE-MRI and FDG-PET/CT in the prediction of response to preoperative chemotherapy with bevacizumab for colorectal liver metastases. Br J Cancer 2012;106(12):1926-33.

47. Kozlowski P, Chang SD, Jones EC, Berean KW, Chen H, Goldenberg SL. Combined diffusion-weighted and dynamic contrast-enhanced MRI for prostate cancer diagnosis--correlation with biopsy and histopathology. J Magn Reson Imaging 2006;24(1):108-13.

48. Kozlowski P, Chang SD, Meng R, Madler B, Bell R, Jones EC, Goldenberg SL. Combined prostate diffusion tensor imaging and dynamic contrast enhanced MRI at 3T--quantitative correlation with biopsy. Magn Reson Imaging 2010;28(5):621-8.

CHAPTER 3

AN ANALYSIS OF THE PHARMACOKINETIC PARAMETER RATIOS IN DCE-MRI USING THE REFERENCE REGION MODEL[1]

[1] Lee J, Platt S, Kent M, Zhao Q. *Magn Reson Imaging* 2012;30(1):26-35.
Reprinted here with permission of the publisher.

3.1 Abstract

Dynamic contrast-enhanced magnetic resonance imaging (DCE-MRI) is performed by obtaining sequential MRI images, before, during, and after the injection of a contrast agent. It is usually used to observe the exchange of contrast agent between the vascular space and extravascular extracellular space (EES), and provide information about blood volume and microvascular permeability. To estimate the kinetic parameters derived from the pharmacokinetic model, accurate knowledge of the arterial input function (AIF) is very important. However, the AIF is usually unknown, and it remains very difficult to obtain such information noninvasively. In this paper, without knowledge of the AIF, we applied a reference region (RR) model to analyze the kinetic parameters. The RR model usually depends on kinetic parameters found in previous studies of a reference region. However, both the assignment of reference region parameters (inter-subject variation) and the selection of the reference region itself (intra-subject variation) may confound the results obtained by RR methods. Instead of using literature values for those pharmacokinetic parameters of the reference region, we proposed to use two pharmacokinetic parameter ratios between the tissue of interest (TOI) and the reference region. Specifically, one parameter K_R is calculated as the ratio between the volume transfer constant K^{trans} of the TOI and RR. Similarly another parameter V_R is calculated as the ratio between the extravascular extracellular volume fraction v_e of the TOI and RR. To investigate the consistency of the two ratios, the K^{trans} of the RR was varied ranging from 0.1 to 1.0 min^{-1}, covering the cited literature values. A simulated dataset with different levels of Gaussian noises and an *in vivo* dataset acquired from five canine brains with spontaneous occurring brain tumors were used to study the proposed ratios. It is shown from both datasets that these ratios are independent of K^{trans} of the RR, implying that there is potentially no need to

obtain information about literature values from the reference region for future pharmacokinetic modeling and analysis.

3.2 Introduction

Dynamic contrast-enhanced magnetic resonance imaging (DCE-MRI) has been widely studied as a cancer imaging tool. It is a noninvasive, clinical imaging technique that is applied to access the microvascular status of tumor tissue and characterize tumor response to antiangiogenic treatment (1,2). Applications of DCE-MRI include, but are not limited to, detection of rheumatoid arthritis (3), differentiation of tumor histopathology (4), noninvasive assessment of tumor microenvironment (5), and predictors of clinical outcomes, including treatment response to chemotherapy (6).

DCE-MRI require repeated acquisition of T_1-weighted images of a particular region-of interest (ROI) before, during and after an intravenous administration of a bolus of a paramagnetic contrast agent (CA), typically a low-molecular-weight gadolinium (Gd) compound. The MR signal in a ROI or voxel can reveal information about blood flow, capillary leakage, and related physiological parameters such as the volume transfer constant (K^{trans}) and extravascular extracellular volume fraction (v_e). These parameters are usually extracted by fitting DCE-MRI data to a model (7,8). Several pharmacokinetic models have been proposed to analyze DCE-MRI (9-11). The most widely used model in DCE-MRI is the two-compartment model (11,12), which uses pharmacokinetic parameters (13) to describe the exchange of contrast agent between the blood plasma compartment and extravascular extracellular space (EES). In this model, contrast agent enters through the vascular space by perfusion, and diffuses between the vascular space and EES of the tumor.

In a typical DCE-MRI study, analysis of the data requires knowledge of the concentration of the CA in the blood plasma as a function of time, denoted C_p, also referred to as arterial input function (AIF). It is difficult to estimate the kinetic parameters such as the K^{trans} and v_e without knowledge of the AIF. Traditionally AIF is obtained by direct blood sampling from an artery (14). However, this procedure is very difficult and invasive. Furthermore, because of the characteristics of blood, direct measurement of the arterial blood concentration of contrast is not always accurate. Many efforts have been made to estimate the AIF for obtaining accurate pharmacokinetic parameters without the invasive procedure of sampling the blood. One approach is that AIF can be obtained from the DCE-MRI data sets (15) by measuring signal intensity changes in both the blood and tissue. Other approaches for estimating the AIF include modeling (16,17), temporal fitting methods (18), perfusion measurement based methods (19), multiple reference region methods (7), phase-based methods (19-21), and extraction of an AIF from various parts of the body in DCE-MRI (22). However, errors in these methods arise from many factors, including T_2^* effects (23), partial volume effects (24), low signal to noise ratio (SNR) when sampling smaller arteries, and the fast flow of blood in the artery (7). Also a major artery may not be in the field of view (FOV) in most DCE-MRI studies (25) .

To overcome the problem associated with direct measurement of the AIF, a reference region model was introduced (1,7,8,26-29). This method uses a reference region, such as muscle, to estimate pharmacokinetic parameters without obtaining the information that the AIF has to offer. For example, the reference region method proposed by Yankeelov *et al*. (8) used a single reference region to extract quantitative estimates of the pharmacokinetic parameters. Yang *et al*. applied multiple reference regions in the analysis (28). Further improvements of the reference region model include incorporation of the effects of transcytolemmal water exchange (30) and a

vascular term in the reference region model (29). The results from the estimation of the kinetic parameters using the reference region model accord well with the pharmacokinetic parameters obtained using the AIF (31). Furthermore, the reference region model has been used for quantitative pharmacokinetic analysis in positron emission tomography (PET) (32).

One limitation of the reference region model is that it requires information about the K^{trans} value for reference regions. The K^{trans} parameter can vary from subject to subject even for a well characterized reference region (8). In this paper, without knowledge of the AIF, we applied the reference region model to analyze the kinetic parameters. Instead of using literature values for the reference region, we proposed two pharmacokinetic parameter ratios between the tissue of interest (TOI) and a reference region (RR). Specifically, the first ratio K_R is calculated by using the volume transfer constant K^{trans} of the TOI and RR, and similarly the second ratio, V_R, is calculated by using the extravascular extracellular volume fraction v_e of the TOI and RR. To investigate the consistency of the two ratios, K^{trans} of the RR was varied ranging from 0.1 to 1.0 min^{-1}, covering the cited literature values. A simulated dataset and *in vivo* data sets acquired from five canine brains with spontaneous occurring brain tumors were analyzed to calculate the proposed pharmacokinetic parameter ratios.

3.3 Theory

The two-compartment model (11,12) is the most widely used kinetic model for DCE-MRI to estimate pharmacokinetic parameters such as blood volume and permeability that are associated with tumors. A simple two-compartment model is shown in Fig. 3.1. In this model, CA diffuses from the blood plasma into EES for the TOI and the RR, respectively. Pharmacokinetic parameters that can be estimated from DCE-MRI data were defined and

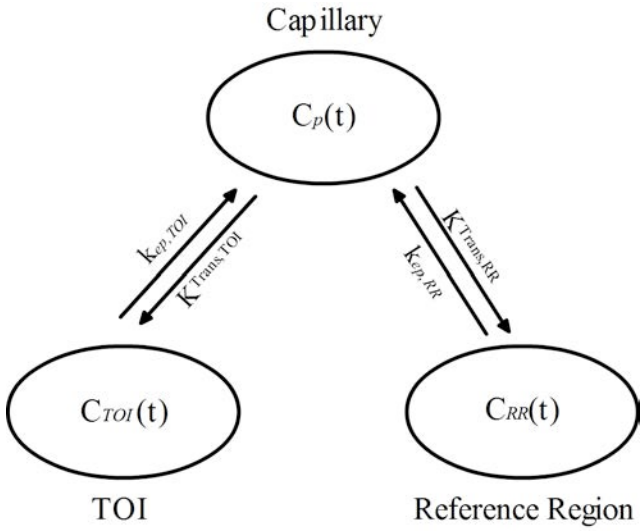

Figure 3.1 A two-compartment model diagram for the reference region model. $C_p(t)$, $C_{TOI}(t)$, and $C_{RR}(t)$ represent the concentration of the contrast agent in blood plasma, the tissue of interest and the reference region, respectively. K^{trans} and k_{ep} represent the volume transfer constant and flux rate constant, respectively. Contrast agent from the blood plasma diffuses from the intravascular space to the extravascular-extracellular space of the tissue of interest and vice versa.

standardized by Tofts *et al*. by using a differential equation for this two compartment model (13) as

$$\frac{dC_t}{dt} = K^{trans}C_p - k_{ep}C_t \qquad [3.1]$$

where C_t and C_p are the concentration of the contrast agent in the EES and plasma space respectively, and the flux rate constant, $k_{ep} = K^{trans}/v_e$. Similarly, differential equations for a multiple region system (i.e. the TOI and RR) are given as Eq. [3.2] and [3.3];

$$\frac{dC_{TOI}(t)}{dt} = K^{trans,TOI}C_p(t) - k_{ep,TOI}C_{TOI}(t) \qquad [3.2]$$

$$\frac{dC_{RR}(t)}{dt} = K^{trans,RR}C_p(t) - k_{ep,RR}C_{RR}(t) \qquad [3.3]$$

where C_{TOI} and C_{RR} are the concentrations of contrast agent in the TOI and the RR. $K^{trans,TOI}$ and

$K^{trans,RR}$ are the volume transfer constants, representing diffusion of the contrast agent from capillaries to the TOI and the RR, respectively. Similarly, $k_{ep,TOI}$ and $k_{ep,RR}$ are the flux rate constants from the TOI and the RR back to the capillaries, respectively. We can eliminate the C_P term by combining these two equations. The combined equation, Eq. [3.4], and the solution for this combined equation can be expressed in the following form,

$$\frac{d}{dt}\left[C_{TOI}(t)\cdot \mathrm{e}^{\frac{K^{trans,TOI}}{v_{e,RR}}t} \right] = \frac{K^{trans,TOI}}{K^{trans,RR}} \frac{dC_{TOI}(t)}{dt} \mathrm{e}^{\frac{K^{trans,TOI}}{v_{e,RR}}t} + \frac{K^{trans,TOI}}{v_{e,RR}} C_{RR}(t) \mathrm{e}^{\frac{K^{trans,TOI}}{v_{e,RR}}t} \qquad [3.4]$$

$$C_{TOI}(t) = K_R \cdot C_{RR}(t) + K_R \left(k_{ep,RR} - k_{ep,TOI} \right) \times \int_0^t C_{RR}(t) \mathrm{e}^{-\frac{K^{trans,TOI}}{v_{e,RR}}(t-t')} dt' \qquad [3.5]$$

where K_R is defined as a ratio between the two volume transfer constants, $K^{trans,TOI}$ and $K^{trans,RR}$. Note that we cannot measure C_t, the concentration of CA, directly from the intensity of a DCE-MRI image. However, when the C_t is relatively low, there is a linear relationship between the concentration of CA and the longitudinal relaxation rate constant 1.

$$R_1 = r_1 C_t + R_{10} \qquad [3.6]$$

where $R_1 = 1/T_1$, r_1 is the relaxivity (in $mM^{-1}s^{-1}$), and R_{10} is the 'native' relaxation rate (i.e., the value of R_1 without presence of the CA). The final solution with Eq. [3.6] is given as Eq. [3.7] (8).

$$R'_{1,TOI} = K_R R'_{1,RR} + K_R V_R \left(\frac{K^{trans,RR}}{v_{e,TOI}} - \frac{1}{V_R{}^2} \frac{K^{trans,TOI}}{v_{e,RR}} \right) \times \int_0^t R'_{1,RR} \exp\left[-k_{ep,TOI}(t-t') \right] dt' \qquad [3.7]$$

where $R'_{1,TOI} = R_{1,TOI} - R_{10,TOI}$ and $R'_{1,RR} = R_{1,RR} - R_{10,RR}$. Similar to the above defined K_R, V_R is the ratio between v_e for the TOI and the RR. The two ratios, K_R and V_R, can be derived through a curve fitting procedure using Eq. [3.7]. To investigate consistency of the two ratios, we used a simulated data set and in vivo data sets acquired from five canine brains with spontaneous

occurring brain tumors. In the following, $K^{trans,RR}$ was assigned a value ranging from 0.1 to 1.0 min^{-1}, covering the values reported by other groups (33).

3.4 Methods

Simulated datasets

We simulated the AIF curve using the following Eq. [3.8] (8).

$$C_p(t) = A \cdot t \cdot e^{-B \cdot t} + C\left(1 - e^{-D \cdot t}\right)e^{-E \cdot t} \quad [3.8]$$

where A = 0.6 $mMmin^{-1}$, B = 0.18 min^{-1}, C = 0.45 mM, D = 0.5 min^{-1}, and E = 0.013 min^{-1}. This AIF curve agrees with that of Simpson et al.34. The C_t curves were then generated for the TOI and RR using the following Eq. [3.9] (6)

$$C_t(t) = K^{trans} \int_0^t C_P(t)\, \mathrm{e}^{-k_{ep}(t-t')}\, dt' \quad [3.9]$$

where K^{trans} = 0.20 min^{-1} and v_e = 0.20 were assigned for the $C_{t,RR}$ and K^{trans} = 0.3 min^{-1} and v_e = 0.40 were assigned for the $C_{t,TOI}$. The curves are shown in Fig. 3.2 (a) where the time scale was discretized with 1 min temporal resolution, range from 0 to 40 min. The C_t curves were then converted to R_1 curves using Eq. [3.6], where R_{10} for the TOI and the RR was assigned a value of 0.7 s^{-1} and 0.55 s^{-1} , and r_1 was assigned the value 3.6 $mM^{-1}s^{-1}$. The R_1 curves are shown in Fig. 3.2 (b).

Direct input of simulated R_1 data from TOI and RR into Eq. [3.7] was attempted but it turned out that the results had a lot of variation due to bad fitting. Instead a nonlinear regression analysis was adopted for modeling and analyzing variables. We applied the nonlinear regression analysis on the simulated R_1 data for the reference region, and then the regression model to Eq. [3.7] for the TOI. The detailed procedure is: first, substituting the Eq. [3.8] and Eq. [3.9] into Eq.

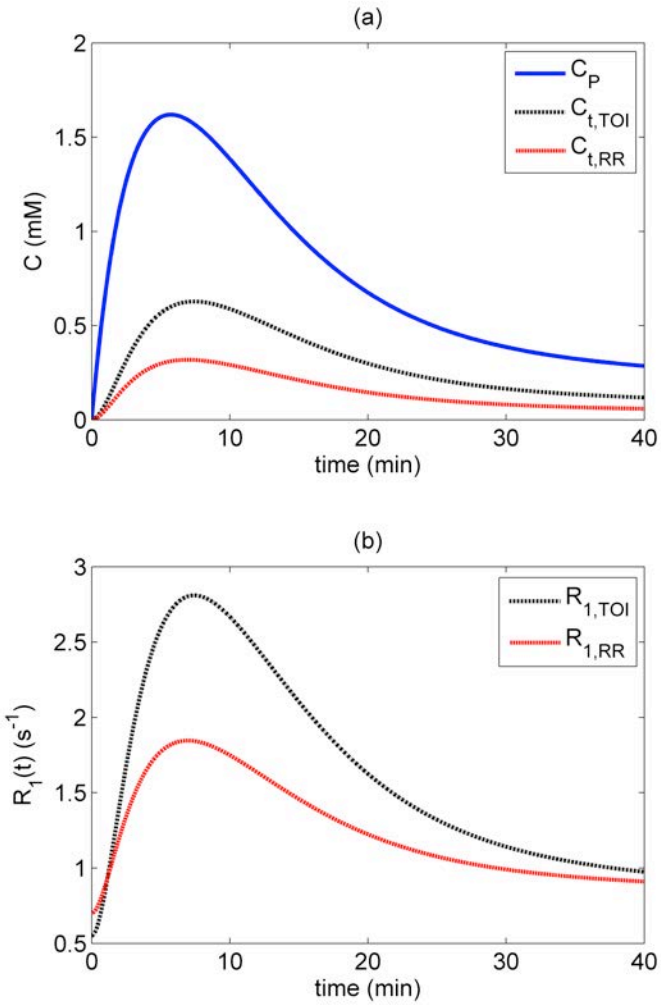

Figure 3.2 Simulation study, where the simulated time curve for the concentration of CA in the blood plasma (C_p), TOI ($C_{t,TOI}$), and RR ($C_{t,RR}$) is displayed in (A) and the R_1 time curve converted from the simulated C_p time curve using Eq. [3.6] in (B).

[3.6] to get the R_1 model (see Appendix)

$$R_1(t) = r_1 \cdot A_6 \cdot e^{-A_7 \cdot t}\left[\frac{A_1 \cdot t}{A_7 - A_2} e^{(A_7 - A_2)t} - \frac{1}{(A_7 - A_2)^2}\left(e^{(A_7 - A_2)t} - 1\right)\right.$$

$$\left. + \frac{A_3}{A_7 - A_5}\left(e^{(A_7 - A_5)t} - 1\right) - \frac{A_3}{A_7 - A_4 - A_5}\left(e^{(A_7 - A_4 - A_5)t} - 1\right)\right] \qquad [3.10]$$

where A_1, A_2, A_3, A_4, A_5, A_6, and A_7 are parameters that can be extracted from a nonlinear regression analysis using a least square method. Next, we applied this R_1 model to Eq. [3.7] and then applied a curve–fitting routine to extract the pharmacokinetic parameters, K^{trans} and v_e for the TOI, and v_e for the RR, while K^{trans} for the RR was assigned from 0.1 min^{-1} to 1.0 min^{-1}. Then we calculated the ratios K_R and V_R between the TOI and the RR. To further test the accuracy of the model, 2%, 5%, and 10% random Gaussian noise were added to the R_1 TOI curves. The noise level is defined as, n% noise = (mean R_1 TOI value) × (n/100), where the mean R_1 TOI was obtained by averaging the R_1 TOI dataset while a maximum value of R_1 TOI was employed in the reference (8). The noise corrupted R_1 curves are shown in Fig. 3.3. In Fig. 3.3, the dotted curve is the simulated R_1 TOI by plugging the Eq. [3.8] into Eq. [3.9] and then to Eq. [3.6]. And the red curve is obtained from putting Eq. [3.10] into Eq. [3.7] with a curve fitting in a nonlinear regression framework.

Experimental datasets

Five canine brains with spontaneous occurring brain tumors were imaged using a 3.0 Tesla GE SIGNA HDX MR scanner (GE Medical Systems, Milwaukee, WI) and a transmit/receive coil. A spoiled gradient echo sequence with variable flip angles of 15^0, 30^0, 45^0, 60^0 and 75^0 was scanned before contrast agent was injected at the repetition time (TR) of 400 ms and echo time (TE) of 2.24 ms. The paramagnetic contrast agent, gadopentetate dimeglumine or Gd-DTPA, was injected intravenously (IV) as a bolus (0.2 mMol/kg) after the first acquisition pulse. The DCE-MRI protocol employed a standard T_1-weighted, 2-D Gradient refocused echo (GRE)

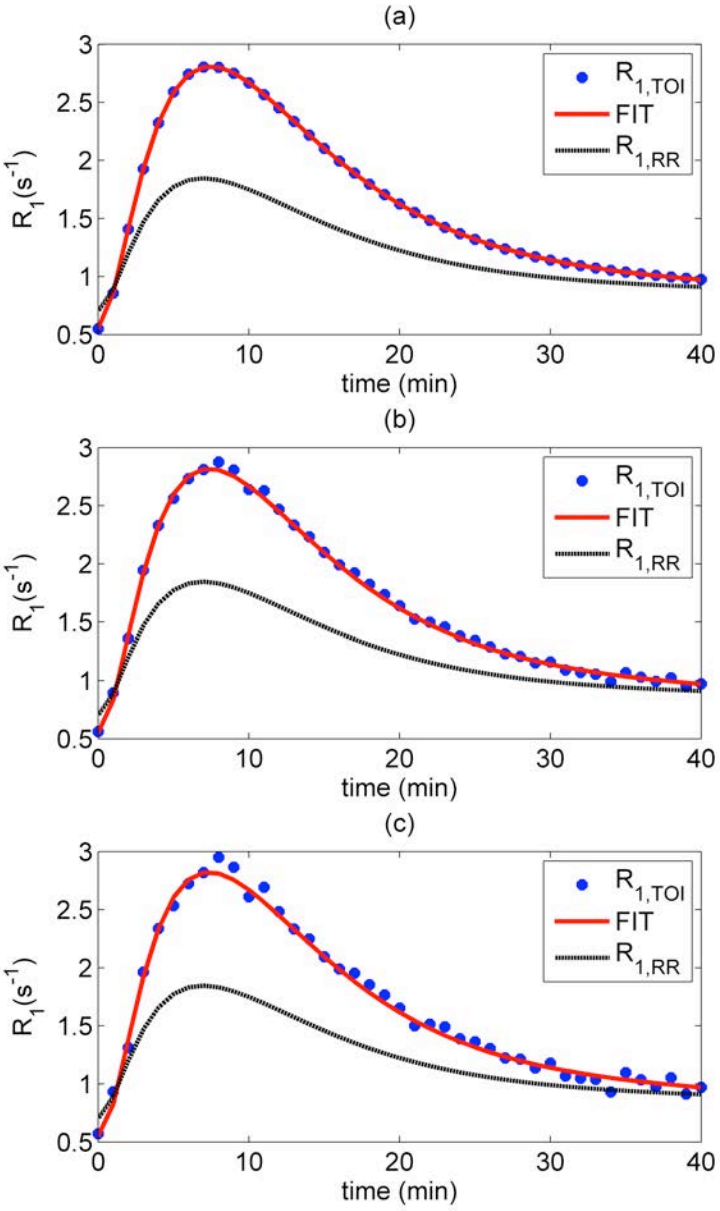

Figure 3.3 R_1 simulation curve for the TOI, the RR and the results of fitting the RR model to simulated TOI curves, respectively. Gaussian noise is added to the simulated R_1 TOI curves at different levels, with (A) 0%, (B) 5%, and (C) 10%.

sequence to obtain 41 serial images. TR was 34 ms, TE was 2.78 ms with a 35^0 flip angle, slice thickness of 3 mm, and NEX=1. The matrix size is 192×192, with a field of view (FOV) of 182.25 cm^2.

The acquired variable flip angle data was used to estimate the initial R_{10} map. The signal as a function of the flip angle is given by Eq. [3.11] and the values for the R_{10} before the injection of the CA can be obtained using following Eq. [3.11] with the variable flip angle data.

$$\rho(\theta) = \rho_0 e^{-T_E/T_2^*}\left[\left(1-e^{-T_R\cdot R_1}\right)\sin\theta / \left(1-e^{-T_R\cdot R_1}\cos\theta\right)\right] \quad [3.11]$$

where θ is flip angle and ρ_0 is proton density. By assuming that $T_E << T_2^*$ 8, the term $exp(-T_E/T_2^*)$ can be neglected from Eq. [3.10] and it can be rewritten into Eq. [3.12]

$$\rho(\theta) = \rho_0\left[\left(1-e^{-T_R\cdot R_1}\right)\sin\theta / \left(1-e^{-T_R\cdot R_1}\cos\theta\right)\right] \quad [3.12]$$

Then relaxation time courses were estimated by using the R_{10} map. The Relaxation time courses are given by Eq. [3.13] (35)

$$R_1(t) = \frac{1}{T_R}\ln\left[\left(\rho_0\sin\theta - \rho(t)\cos\theta\right)/\left(\rho_0\sin\theta - \rho(t)\right)\right] \quad [3.13]$$

where ρ_0 represents fully relaxed magnetization for a given voxel and is obtained from Eq. [3.14]

$$\rho_0 = \rho_{ss}\left[\left(1-e^{-TR\cdot R_{10}}\cos\theta\right)/\left(1-e^{-TR\cdot R_{10}}\right)\right] \quad [3.14]$$

where ρ_s is the steady-state voxel-averaged intensity before CA was injected.

Thirty voxels were selected manually from suspected lesion tissue as the TOI and thirty voxels from normal brain tissue as the RR, respectively, for dataset 1 through 4, and twelve voxels were selected for dataset 5 because of a smaller size of lesion compared to other datasets. First, the R_1 datasets are generated by Eq. [3.13] for lesion tissue and normal brain tissue. We

then applied a nonlinear regression analysis to the R_1 dataset for the reference region to substitute in place of the raw R_1 dataset so that a model, Eq. [3.15], could be applied to the reference region model. Eq. [3.15] is a nonlinear regression model used to obtain a regularized, well-behaved $R_{1,RR}(t)$ curve from Eq. [3.13]. In other words, Eq. [3.15] is acquired by parameterized curve fitting in a nonlinear regression framework. For the experimental data analysis, we use the equation as a model from the signal enhancement equation from Brix *et. al*. (13,18,36).

$$R_{1,RR}(t) = \frac{C_1}{C_2 - C_3}\left[e^{-C_3(t-C_4)} - e^{-C_2(t-C_4)}\right] \qquad [3.15]$$

where C_1, C_2, C_3, and C_4 are parameters replaced from the flux rate constants on the signal enhancement equation from Brix *et. al.* (13,18,36). These parameters can be extracted from a nonlinear regression analysis. This R_1 model was substituted into the reference region model Eq. [3.7], and a least square method was applied to Eq. [3.7] to estimate pharmacokinetic parameters, K^{trans} and v_e for the TOI, and v_e for the RR, while K^{trans} for the RR was varied between 0.1 and 1.0 min^{-1}.

Since the distribution of the canine lesion datasets is unknown, the Kruskal Wallis test (37), a non-parametric method for testing equality of population medians among groups was used to determine if the lesions differed significantly from each other by using the proposed two ratios. The Kruskal-Wallis test starts by arranging the data of all samples in a single series in ascending order to assign rank according to the K_R and V_R values. It then substitutes that rank into the overall data set for each K_R and V_R value. In this Kruskal-Wallis one-way analysis of variance (ANOVA), the chi-square statistic is used to evaluate differences in mean ranks to assess the null hypothesis that the populations, from which the samples originate, have the same median. The purpose of ANOVA is to find out whether data from five canine datasets have a

common mean or not. In the ANOVA table, several parameters are usually given including sum of square (SS), degree of freedom (df), mean square (MS), chi-square which is one of the most widely used probability distributions in inferential statistics, and probability. In this manuscript, the mean values of K_R and V_R were used, where the different values of K_R and V_R were obtained by varying K^{trans} from the RR for each voxel. The sum of the ranks is calculated for each group then the test statistic is calculated. Following the Kruskal Wallis test, a two-sample Kolmogorov-Smirnov test (KS test) was used to determine if any two lesions differed significantly. The KS test, a non-parametric pairwise method, does not require the assumption about the distribution of data. A p-value equal or close to 1 implies the two datasets of the ratios compared come from the same distribution, while a p-value of zero implies that they have different distributions.

3.5 Results

Simulations

The ratios K_R and V_R were calculated based on the simulated datasets and are shown in Fig. 3.4. We applied a curve-fitting routine written in MATLAB software program to extract three parameters, K^{trans} and v_e for the TOI, and v_e for the RR, while K^{trans} for the RR was assigned from 0.1 min^{-1} to 1.0 min^{-1}. For the dataset without noise, the results from the simulation gave the ratios K_R=1.497 and V_R= 2.000 compared to the known values of K_R=1.5 and V_R= 2.0. Then, 5% and 10% noise was added to the data to check the two ratios' sensitivity to noise. For the 5% noise case, the ratios are K_R=1.339 and V_R= 1.996. For the 10% noise case, the ratio are K_R=1.144 and V_R=1.995. Fig. 3.4 shows these values with K_R and V_R as the slope of fitted lines. In Fig. 3.4 (a) for the case of zero noise, K_R was shown to have a slope very close to the calculated value of 1.5. For the case of added noise, there is a small difference between the

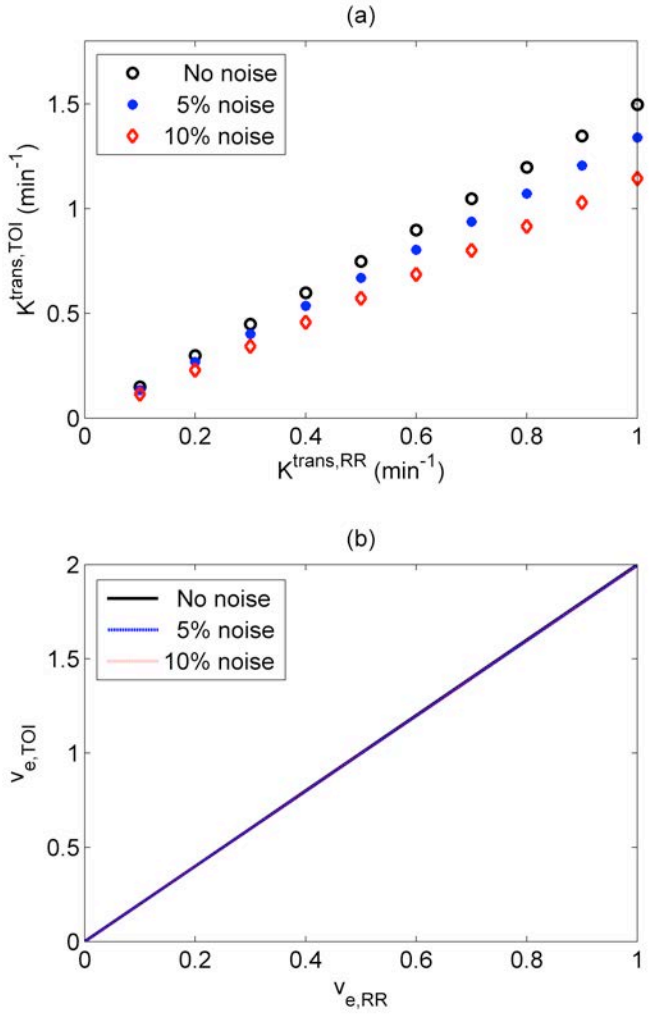

Figure 3.4 A plot of the ratio between K^{trans} in the TOI and in the RR calculated from the simulated data. $K^{trans,TOI}$ was extracted, while $K^{trans,RR}$ in the RR value was assigned from 0.1 to 1.0 min^{-1}. (A) The ratio K_R is 1.497 in the absence of noise, 1.340 when 5% noise was added and 1.144 when 10% noise was added. (B) The calculated ratio V_R is 2.000 without noise, 1.996 in 5% noise data and 1.995 in 10% noise data.

values. In Fig. 3.4 (b), the values of V_R are very close to the calculated value, no matter noise was added or not.

Experiments

For the in vivo experiments, representative R_1 curves of a single voxel from the five brain lesion datasets were analyzed and shown in Fig. 3.5. In Fig. 3.5, a red dot represents an $R_{1,TOI}$ data point and a blue star denotes an $R_{1,RR}$ data point. The dashed line indicates an $R_{1,RR}$ model created by regression analysis and the solid line represents the results of the fitting routines. The time scale, discretized with a temporal resolution of approximate 8 seconds, had a range from 0 to 320 seconds. The R_1 curves in the TOI rapidly increased while the R_1 curves in the RR were almost flat in most of the canine brain lesion datasets.

The data were analyzed on a voxel-by-voxel basis to construct pharmacokinetic parameters $K^{trans,TOI}$, $v_{e,TOI}$, and $v_{e,RR}$ while $K^{trans,RR}$ was assigned a value ranging from 0.1 to 1.0 min^{-1}. Then, K_R and V_R were calculated and the results are shown in Fig. 3.6. The mean and standard deviations of K_R and V_R are listed in Table 3.1.

Fig. 3.7(a) displays box plots for K_R of the five lesion datasets. It shows that there is a significantly different K_R value between the five datasets except for data 1, data 3, and data 4. In Fig. 3.7(b), there is a significantly different V_R value between the five datasets except for data 1 and data 5. The Kruskal Wallis analysis of variance result is listed in Table 3.2, where the value of probability is close to zero for both K_R and V_R, implying that there is a significant difference among all five datasets.

The results for the KS test are shown in the Table 3.3, where each component in the table is a p-value. The p-values for K_R between data 1 and data 3, data 1 and data 4, and data 3 and data 4 are 0.2667, 0.34020, and 0.5372, respectively, implying that there is no significant difference between data 1, data 3, and data 4. The p-values for V_R between datasets have a value of zero or < 0.05 implying that they come from different distribution.

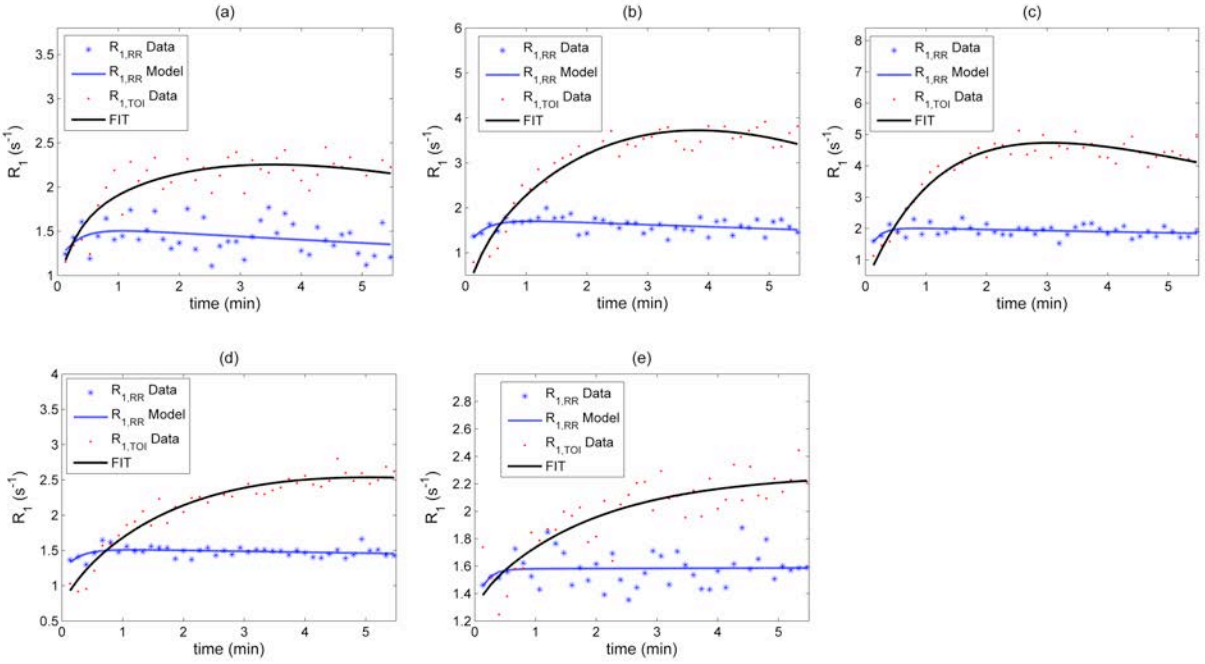

Figure 3.5 The results of the RR model fitting to data from the TOI using the five in vivo canine datasets. Each curve is plotted from one representative voxel randomly selected from the dataset. The red dot and the blue star represent the $R_{1,TOI}$ dataset and the $R_{1,RR}$ dataset, respectively, whicle the solid line indicates the $R_{1,TOI}$ model and the dotted line indicates the $R_{1,RR}$ model created by regression analysis. The r^2 values of the curves for the TOI and the RR are (A) 0.71 and 0.09, (B) 0.93 and 0.21, (C) 0.91 and 0.16, (D) 0.94 and 0.17, and (E) 0.71 and 0.03, respectively.

3.6 Discussion

Several pharmacokinetic models have been previously proposed to analyze DCE-MRI data. However, they require information about the concentration of the CA in the blood plasma. Alternatively, methods using reference regions were proposed without direct measurement of the AIF. In the reference region model, two assumptions are required. First, the AIF in both RR and TOI should be the same. Variations in AIFs of the two regions will make estimation errors. Second, both pharmacokinetic parameters, $K^{trans,RR}$ and $v_{e,RR}$, are required from the previous

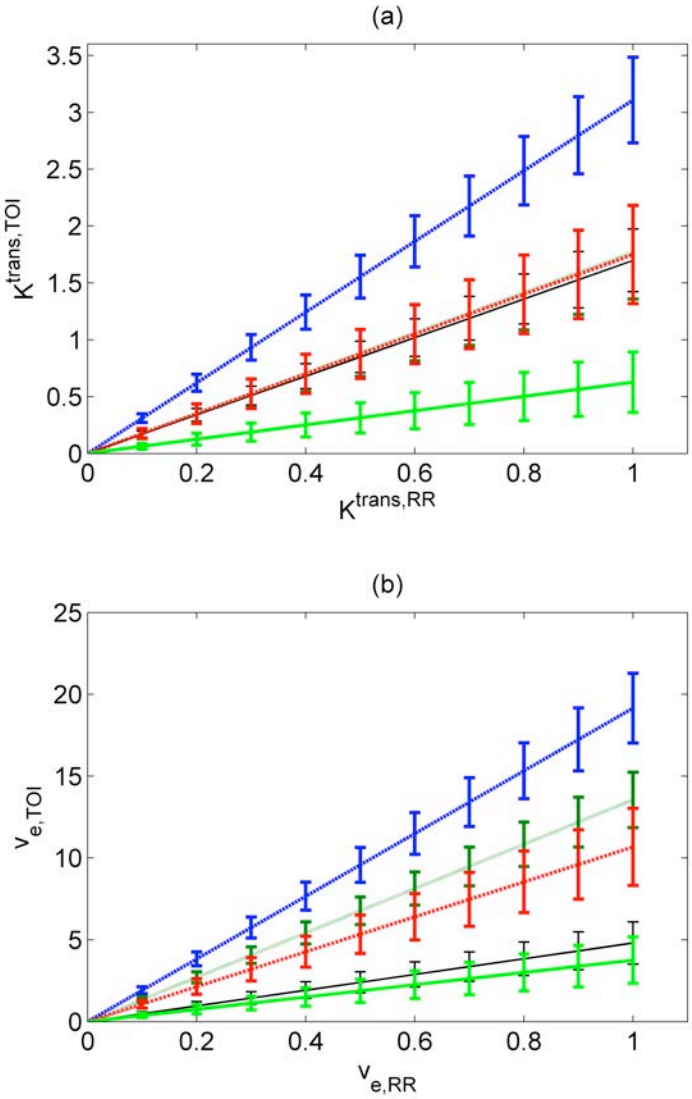

Figure 3.6 The plot for the pharmacokinetic parameter ratio between the RR and the TOI of the five canine datasets. (A) The ratio KR is between K^{trans} in the RR and the TOI. (B) The ratio V_R is between v_e in the RR and the TOI.

literature. However, both simulations and experimental data revealed that systematic error in the kinetic parameters of some TOI may be caused by incorrect assignments of the parameters for the reference regions. This is because both intra- and inter-subject (animal or human) variation in

RR parameter values may introduce errors. The assignment of reference region parameters (inter-subject variation) and the selection of the reference region itself (intra-subject variation) may confound the results obtained by traditional reference region methods.

In this paper, we have presented a method that calculated pharmacokinetic parameter ratios, K_R and V_R, between the TOI and the RR. The first attempt of direct input of simulated R_1 data from TOI and RR into Eq. [3.7] failed due to the fitting difficulty. We next adopted a regression analysis on the simulated R_1 data for the reference region, and then applied this regression model to the reference region model for the TOI. This gave us very good results as shown in Fig. 3.3 when no noise was involved. The regression model for the simulation comes directly from Eq. [3.8] and it fits well the data. For the experimental data, the regression model was adopted from the signal enhancement equation from Brix *et al*. (13,18,36) since this model works very well for the experimental datasets. In Fig. 3.5, it is seen that the R^2 values look normal for the $R_{1,\ TOI}$ data, but are very low for the $R_{1,\ RR}$ curves. This is because the R_{1_TOI} curves are showing a regular enhancing pattern, but the R_{1_RR} curves have a slow enhancing trend, instead they are almost flat in most of the datasets. Our results obtained from both simulation and *in vivo* datasets indicated that the parameter ratios K_R and V_R are independent of parameters of the reference regions, $K^{trans,RR}$ and $v_{e,RR}$. This allows one to eliminate the requirement of a given value from the literature when considering the ratios.

It is noted here that relative K^{trans} and v_e maps were previously proposed by Yankeelov et al. (8). This could potentially reduce systematic error from incorrect RR parameter assignments. According to their method, by replacing $K^{trans,TOI}/K^{trans,RR}$ with R^1, $K^{trans,RR}/v_{e,RR}$ with R^2, and

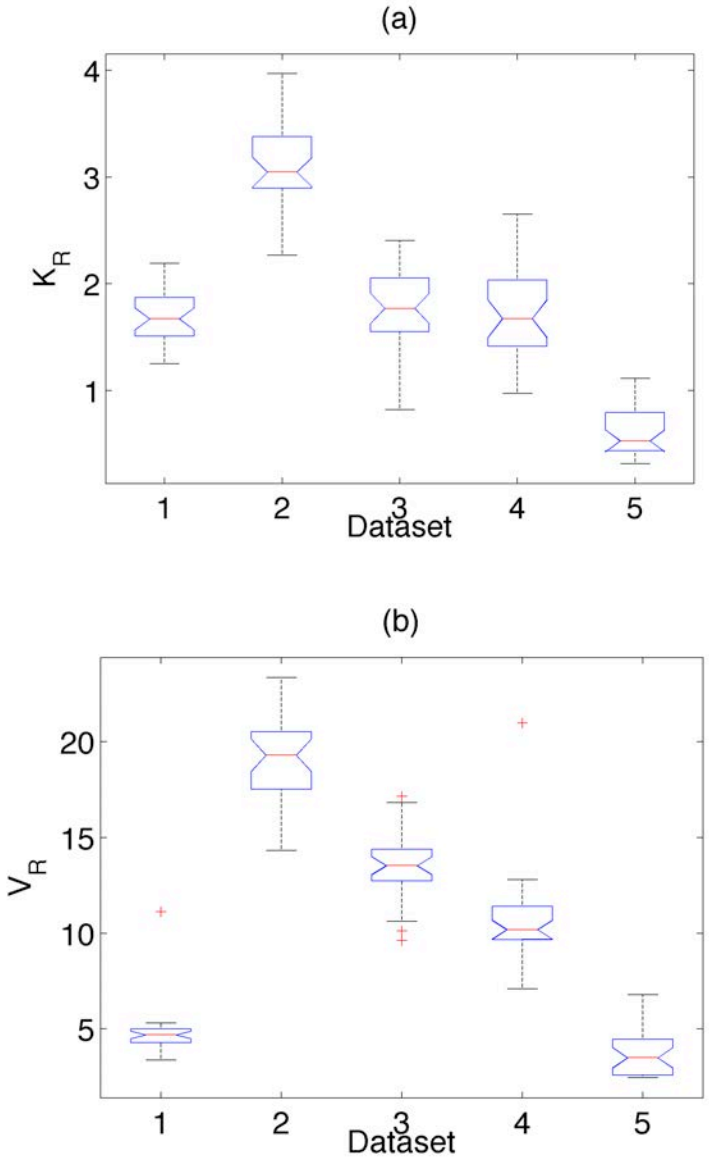

Figure 3.7 The box plot for the five canine datasets using the Kruskal-Wallis test for (a) K_R and for (b) V_R indicating the smallest observation (minimum), lower quartile (25th percentiles), the median (red horizontal line), upper quartile (75th percentiles), and the largest observation (maximum). There is a significant difference between the datasets for K_R and V_R.

$K^{trans,TOI}/v_{e,TOI}$ with R^3, Yankeelov et al, used the reference region model [3.7] to provide a three-parameter fit to DCE-MRI time courses to extract R^1, R^2, and R^3. They extracted the three

Table 3.1. Canine brain lesions analysis results of K_R and V_R

Ratio	Canine brain tumor				
	Data 1	Data 2	Data 3	Data 4	Data 5
K_R	1.6980 ±0.2749	3.1085 ±0.3767	1.7695 ±0.4106	1.7492 ±0.4324	0.6269 ±0.2658
V_R	4.8038 ±1.2831	19.1557 ±2.1316	13.5476 ±1.6953	10.6719 ±2.3525	3.7552 ±1.4142

relative parameters directly from the fitting algorithm, and then the reference region model [3.7] was used to conduct a full four parameter fit, subject to the results of the relative parameter values. They suggested that this might eliminate the requirement for assumptions on the RR.

In the present study similar kinetic parameter ratios were proposed with the assignment of various $K^{trans,RR}$ values. Different from the work in 8, in our method we assign the $K^{trans,RR}$ value from 0.1 to 1.0 min^{-1} and extract three parameters ($K^{trans,TOI}$, $v_{e,TOI}$, and $v_{e,RR}$) to calculate pharmacokinetic parameter ratio K_R and V_R. We have shown that these ratios K_R and V_R are very consistent with various $K^{trans,RR}$ values. As seen from the simulation results (Fig. 3.4), the

Table 3.2. Kruskal Wallis ANOVA Table for K_R and V_R

Parameter	Source	SS	df	MS	Chi-sq	Prob
	Columns	212520.2	4	53130.05	112.6	2.030×10^{-23}
K_R	Error	68702.3	145	473.81		
	Total	281222.5	149			
	Columns	249203.3	4	62300.8	132.04	1.429×10^{-27}
V_R	Error	32019.2	145	220.8		
	Total	281222.5	149			

Table 3.3. KS test for K_R

Canine lesion	Data 1	Data 2	Data 3	Data 4	Data 5
Data 1	1	0	0.2667	0. 3420	0
Data 2	0	1	0	0	0
Data 3	0.2667	0	1	0. 5372	0
Data 4	0. 3420	0	0. 5372	1	0
Data 5	0	0	0	0	1

Two-sample KS test were performed. Each component in the table is a P-value that implies the two datasets of the ratios compared come from the same distribution if a value is equal to 1 or close to 1, while a value of zero implies that they have different distributions.

estimated pharmacokinetic parameter ratios K_R and V_R are very close to the true values when no noise is present. As the noise is increased to 5% and 10%, the K_R degrades gradually but the V_R has little change.

From the results obtained by applying the Kruskal Wallis test to the pharmacokinetic parameter ratios K_R and V_R, a significant difference was found for all data sets analyzed in this work. We then applied a pair-wise two-sample Kolmogorov Smirnov test (KS test) to determine if any two lesions differed significantly. Similar to the Kruskal Wallis test, the KS test does not need any assumption about the distribution of data. Since the KS test is sensitive to differences in both location and shape of the empirical cumulative distribution function of two samples, it is one of the most useful and general nonparametric methods for comparing two samples. We can conclude that there is a significantly difference between any two given data distributions. Given these results, it might be possible to assist a differentiation of tumor histopathology from the pharmacokinetic parameter ratios K_R and V_R. Future studies will be conducted to verify the correlation between tumor histopathology and the pharmacokinetic parameter ratios K_R and V_R.

Table 3.4. KS test for V_R

Canine Lesion	Data 1	Data 2	Data 3	Data 4	Data 5
Data 1	1	0	0	0	0.0044
Data 2	0	1	0	0	0
Data 3	0	0	1	0	0
Data 4	0	0	0	1	0
Data 5	0.0044	0	0	0	1

One drawback of the proposed method is that the regression model for the reference region data cannot fit the R_1 curve in the TOI well, when the R_1 curves of the TOI and the reference region do not follow the same trend (both increasing or decreasing). This is likely due to the cases when the TOI and reference regions do not share the same artery for blood supply. In this case, the kinetic parameter ratios will fail to represent the true information.

In conclusion, we have proposed pharmacokinetic parameter ratios, K_R and V_R, between TOI and RR using the reference region model without the information about the AIF. We have shown that the pharmacokinetic parameter ratios K_R and V_R have a slight variation among cases of different level of noises. It was shown that, from both simulation and in vivo data sets, the ratios are independent of $K^{trans,RR}$, implying that there is potentially no need to acquire the information about literature values from reference regions for future pharmacokinetic modeling.

3.7 Acknowledgments

The Authors would like to thank Dr. T. Yankeelov of Vanderbilt University for helpful communication, also thank Dr. Jason Langley, Mr. William Potter, Mr. Sunbok Lee, and Dr. Cheolwoo Park for their help and consultation.

3.8 Appendix

This appendix gives an outline of the mathematical details for the R_1 model (Eq. [3.10]) obtained from Eq. [3.6], Eq. [3.8], and Eq. [3.9]. Eq. [3.10] is a 7-parameter curve-fitting of the raw $R_{1,\,RR}$ (t) curve in the nonlinear regression framework solved with a least squares approach. To obtain it, first plug Eq. [3.8] into Eq. [3.9] as follows

$$C_t(t) = A_6 \int_0^t \left[A_1 \cdot t' \cdot e^{-A_2 \cdot t'} + A_3 \left(1 - e^{-A_4 \cdot t'}\right) e^{-A_5 \cdot t'} \right] \mathrm{e}^{-A_7 (t - t')}\, dt'$$

$$= \mathrm{e}^{-A_7 t}\, A_6 \left[A_1 \int_0^t t' \cdot e^{-A_2 \cdot t'}\, \mathrm{e}^{A_6 t'}\, dt' + A_3 \int_0^t \left(1 - e^{-A_4 \cdot t'}\right) e^{-A_5 \cdot t'}\, \mathrm{e}^{A_6 t'}\, dt' \right]$$

$$= \mathrm{e}^{-A_6 t}\, A_7 \left[A_1 \int_0^t t' \cdot \mathrm{e}^{(A_6 - A_2) t'}\, dt' + A_3 \int_0^t \left(1 - e^{-A_4 \cdot t'}\right) \mathrm{e}^{(A_6 - A_5) t'}\, dt' \right] \qquad \text{[A3.1]}$$

where A_1, A_2, A_3, A_4, and A_5 are the parameters replaced from A, B, C, D, and E in Eq. [3.8]. A_6 and A_7 were replaced from K^{trans} and k_{ep}, respectively.

The first integral in Eq. [A3.1] is

$$\int_0^t t' \cdot \mathrm{e}^{(A_7 - A_2) t'}\, dt' = \frac{t'}{(A_7 - A_2)} \mathrm{e}^{(A_7 - A_2) t'} \Bigg|_0^t - \frac{1}{(A_7 - A_2)} \int_0^t \mathrm{e}^{(A_7 - A_2) t'}\, dt'$$

$$= \frac{t}{(A_7 - A_2)} \mathrm{e}^{(A_7 - A_2) t} - \frac{1}{(A_7 - A_2)^2} \left(e^{(A_7 - A_2) t} - 1 \right) \qquad \text{[A3.2]}$$

and the second integral in Eq. [A3.3] is

$$\int_0^t \left(1 - e^{-A_4 \cdot t'}\right) \mathrm{e}^{(A_7 - A_5) t'}\, dt' = \int_0^t \mathrm{e}^{(A_7 - A_5) t'}\, dt' - \int_0^t \mathrm{e}^{(A_7 - A_4 - A_5) t'}\, dt' \qquad \text{[A3.3]}$$

$$= \frac{1}{A_7 - A_5} \left(e^{(A_7 - A_5) t} - 1 \right) - \frac{1}{A_7 - A_4 - A_5} \left(e^{(A_7 - A_4 - A_5) t} - 1 \right) \qquad \text{[A3.4]}$$

Now, we can express the R_1 model in terms of the parameters A_1, A_2,…, and A_7 by substituting the results from Eq.[A3.2] and Eq.[A3.4] into Eq.[A3.1] and then by substituting

Eq.[A3.1] into Eq. [3.6]

$$R_1(t) = r_1 \cdot A_6 \cdot e^{-A_7 \cdot t}\left[\frac{A_1 \cdot t}{A_7 - A_2} e^{(A_7 - A_2)t} - \frac{1}{(A_7 - A_2)^2}\left(e^{(A_7 - A_2)t} - 1\right)\right.$$

$$\left. + \frac{A_3}{A_7 - A_5}\left(e^{(A_7 - A_5)t} - 1\right) - \frac{A_3}{A_7 - A_4 - A_5}\left(e^{(A_7 - A_4 - A_5)t} - 1\right)\right] + R_{10} \qquad \text{[A3.5]}$$

where R_{10} was assumed to be zero for this simulation.

3.9 References

1. Padhani AR, Leach MO. Antivascular cancer treatments: functional assessments by dynamic contrast-enhanced magnetic resonance imaging. Abdom Imaging 2005;30(3):324-41.
2. Miller JC, Pien HH, Sahani D, Sorensen AG, Thrall JH. Imaging angiogenesis: applications and potential for drug development. J Natl Cancer Inst 2005;97(3):172-87.
3. Workie DW, Dardzinski BJ, Graham TB, Laor T, Bommer WA, O'Brien KJ. Quantification of dynamic contrast-enhanced MR imaging of the knee in children with juvenile rheumatoid arthritis based on pharmacokinetic modeling. Magnetic Resonance Imaging 2004;22(9):1201-10.
4. Zhao Q, Lee S, Kent M, Schatzberg S, Platt S. Dynamic contrast-enhanced magnetic resonance imaging of canine brain tumors. Vet Radiol Ultrasound 2010;51(2):122-9.
5. Jansen JF, Schoder H, Lee NY, Wang Y, Pfister DG, Fury MG, Stambuk HE, Humm JL, Koutcher JA, Shukla-Dave A. Noninvasive assessment of tumor microenvironment using dynamic contrast-enhanced magnetic resonance imaging and 18F-fluoromisonidazole

positron emission tomography imaging in neck nodal metastases. Int J Radiat Oncol Biol Phys 2010;77(5):1403-10.

6. Evelhoch J, Garwood N, Vigneron D, Knopp N, Sullivan D, Menkens A, Clarke L, Liu GY. Expanding the use of magnetic resonance in the assessment of tumor response to therapy: Workshop report. Cancer Research 2005;65(16):7041-7044.

7. Yang C, Karczmar GS, Medved M, Stadler WM. Estimating the arterial input function using two reference tissues in dynamic contrast-enhanced MRI studies: fundamental concepts and simulations. Magn Reson Med 2004;52(5):1110-7.

8. Yankeelov TE, Luci JJ, Lepage M, Li R, Debusk L, Lin PC, Price RR, Gore JC. Quantitative pharmacokinetic analysis of DCE-MRI data without an arterial input function: a reference region model. Magnetic Resonance Imaging 2005;23(4):519-529.

9. Kuwatsuru R, Shames DM, Muhler A, Mintorovitch J, Vexler V, Mann JS, Cohn F, Price D, Huberty J, Brasch RC. Quantification of tissue plasma volume in the rat by contrast-enhanced magnetic resonance imaging. Magn Reson Med 1993;30(1):76-81.

10. Su MY, Jao JC, Nalcioglu O. Measurement of vascular volume fraction and blood-tissue permeability constants with a pharmacokinetic model: studies in rat muscle tumors with dynamic Gd-DTPA enhanced MRI. Magn Reson Med 1994;32(6):714-24.

11. Tofts PS, Brix G, Buckley DL, Evelhoch JL, Henderson E, Knopp MV, Larsson HB, Lee TY, Mayr NA, Parker GJ and others. Estimating kinetic parameters from dynamic contrast-enhanced T(1)-weighted MRI of a diffusable tracer: standardized quantities and symbols. J Magn Reson Imaging 1999;10(3):223-32.

12. Tofts PS, Kermode AG. Measurement of the Blood-Brain-Barrier Permeability and Leakage Space Using Dynamic Mr Imaging .1. Fundamental-Concepts. Magnetic Resonance in Medicine 1991;17(2):357-367.

13. Tofts PS. Modeling tracer kinetics in dynamic Gd-DTPA MR imaging. J Magn Reson Imaging 1997;7(1):91-101.

14. Benjaminsen IC, Brurberg KG, Ruud EB, Rofstad EK. Assessment of extravascular extracellular space fraction in human melanoma xenografts by DCE-MRI and kinetic modeling. Magnetic Resonance Imaging 2008;26(2):160-70.

15. van Osch MJ, Vonken EJ, Viergever MA, van der Grond J, Bakker CJ. Measuring the arterial input function with gradient echo sequences. Magn Reson Med 2003;49(6):1067-76.

16. de Rochefort L, Nguyen T, Brown R, Spincemaille P, Choi G, Weinsaft J, Prince MR, Wang Y. In vivo quantification of contrast agent concentration using the induced magnetic field for time-resolved arterial input function measurement with MRI. Med Phys 2008;35(12):5328-39.

17. Orton MR, d'Arcy JA, Walker-Samuel S, Hawkes DJ, Atkinson D, Collins DJ, Leach MO. Computationally efficient vascular input function models for quantitative kinetic modelling using DCE-MRI. Physics in Medicine and Biology 2008;53(5):1225-39.

18. Hoffmann U, Brix G, Knopp MV, Hess T, Lorenz WJ. Pharmacokinetic mapping of the breast: a new method for dynamic MR mammography. Magn Reson Med 1995;33(4):506-14.

19. Fritz-Hansen T, Rostrup E, Larsson HB, Sondergaard L, Ring P, Henriksen O. Measurement of the arterial concentration of Gd-DTPA using MRI: a step toward quantitative perfusion imaging. Magn Reson Med 1996;36(2):225-31.

20. Ribot EJ, Thiaudiere E, Roulland R, Brugieres P, Rahmouni A, Voisin P, Franconi JM, Miraux S. Application of MRI phase-difference mapping to assessment of vascular concentrations of BMS agent in mice. Contrast Media Mol Imaging 2008;3(2):53-60.

21. Akbudak E, Norberg RE, Conturo TE. Contrast-agent phase effects: an experimental system for analysis of susceptibility, concentration, and bolus input function kinetics. Magn Reson Med 1997;38(6):990-1002.

22. Mlynash M, Eyngorn I, Bammer R, Moseley M, Tong DC. Automated method for generating the arterial input function on perfusion-weighted MR imaging: validation in patients with stroke. AJNR Am J Neuroradiol 2005;26(6):1479-86.

23. Kotys MS, Akbudak E, Markham J, Conturo TE. Precision, signal-to-noise ratio, and dose optimization of magnitude and phase arterial input functions in dynamic susceptibility contrast MRI. J Magn Reson Imaging 2007;25(3):598-611.

24. van Osch MJ, van der Grond J, Bakker CJ. Partial volume effects on arterial input functions: shape and amplitude distortions and their correction. J Magn Reson Imaging 2005;22(6):704-9.

25. Kim YR, Rebro KJ, Schmainda KM. Water exchange and inflow affect the accuracy of T1-GRE blood volume measurements: implications for the evaluation of tumor angiogenesis. Magn Reson Med 2002;47(6):1110-20.

26. Gunn RN, Lammertsma AA, Hume SP, Cunningham VJ. Parametric imaging of ligand-receptor binding in PET using a simplified reference region model. Neuroimage 1997;6(4):279-87.

27. Acton PD, Kushner SA, Kung MP, Mozley PD, Plossl K, Kung HF. Simplified reference region model for the kinetic analysis of [99mTc]TRODAT-1 binding to dopamine transporters in nonhuman primates using single-photon emission tomography. Eur J Nucl Med 1999;26(5):518-26.

28. Yang C, Karczmar GS, Medved M, Stadler WM. Multiple reference tissue method for contrast agent arterial input function estimation. Magn Reson Med 2007;58(6):1266-75.

29. Faranesh AZ, Yankeelov TE. Incorporating a vascular term into a reference region model for the analysis of DCE-MRI data: a simulation study. Physics in Medicine and Biology 2008;53(10):2617-31.

30. Yankeelov TE, Luci JJ, DeBusk LM, Lin PC, Gore JC. Incorporating the effects of transcytolemmal water exchange in a reference region model for DCE-MRI analysis: theory, simulations, and experimental results. Magn Reson Med 2008;59(2):326-35.

31. Yankeelov TE, Cron GO, Addison CL, Wallace JC, Wilkins RC, Pappas BA, Santyr GE, Gore JC. Comparison of a reference region model with direct measurement of an AIF in the analysis of DCE-MRI data. Magn Reson Med 2007;57(2):353-61.

32. Lammertsma AA, Bench CJ, Hume SP, Osman S, Gunn K, Brooks DJ, Frackowiak RS. Comparison of methods for analysis of clinical [11C]raclopride studies. J Cereb Blood Flow Metab 1996;16(1):42-52.

33. Padhani AR, Hayes C, Landau S, Leach MO. Reproducibility of quantitative dynamic MRI of normal human tissues. NMR Biomed 2002;15(2):143-53.

34. Simpson NE, He Z, Evelhoch JL. Deuterium NMR tissue perfusion measurements using the tracer uptake approach: I. Optimization of methods. Magn Reson Med 1999;42(1):42-52.

35. Landis CS, Li X, Telang FW, Coderre JA, Micca PL, Rooney WD, Latour LL, Vetek G, Palyka I, Springer CS, Jr. Determination of the MRI contrast agent concentration time course in vivo following bolus injection: effect of equilibrium transcytolemmal water exchange. Magn Reson Med 2000;44(4):563-74.

36. Brix G, Semmler W, Port R, Schad LR, Layer G, Lorenz WJ. Pharmacokinetic parameters in CNS Gd-DTPA enhanced MR imaging. J Comput Assist Tomogr 1991;15(4):621-8.

37. Kruskal WH, Wallis WA. Use of Ranks in One-Criterion Variance Analysis. Journal of the American Statistical Association 1952;47(260):583-621.

CHAPTER 4

COMPARISON OF ANALYTICAL AND NUMERICAL ANALYSIS OF THE REFERENCE REGION MODEL FOR DCE-MRI[1]

[1] Lee J, Cárdenas J, Platt S, Kent M, Pagel M, and Zhao Q. Submitted to *Magn Reson Imaging*

4.1 Abstract

This study compared three methods for analyzing DCE-MRI data with a reference region (RR) model: a linear least-square fitting with numerical analysis (LLSQ-N), a nonlinear least-square fitting with numerical analysis (NLSQ-N), and an analytical analysis (NLSQ-A). The accuracy and precision of estimating the pharmacokinetic parameter ratios K_R and V_R using each analysis method was assessed using simulations under various signal-to-noise ratios (SNRs) and temporal resolutions (4s, 6s, 30s, and 60s). Seven in vivo DCE-MRI datasets from spontaneously occurring canine brain tumors were analyzed with each method. For the simulations, when no noise was added and the temporal resolution was decreased from 4s to 60s, the mean percent error (MPE) of K_R and V_R for LLSQ-N and NLSQ-N all increased, while the NLSQ-A method maintained a very high accuracy. When noise was added and the temporal resolution was decreased, both numerical analysis methods degraded more severally by underestimating ratios K_R and V_R than the analytical counterpart. In vivo results correlated well with this trend at a similar SNR level between 10 and 20. In this study, we have shown that the NLSQ-A method can estimate pharmacokinetic parameter ratios more accurately than the NLSQ-N and LLSQ-N methods over various SNRs and temporal resolutions.

4.2 Introduction

Dynamic contrast-enhanced magnetic resonance imaging (DCE-MRI) is used to study the exchange of a contrast agent (CA) between the vascular space and extravascular extracellular space (EES), and it provides information about blood volume and microvascular permeability (1). It can be applied to access the microvascular status of tumor tissue and characterize tumor response to antiangiogenic treatment (2,3). DCE-MRI is also used for the differentiation of tumor histopathology (4), detection of rheumatoid arthritis (5), noninvasive assessment of tumor microenvironment (6) and prediction of clinical outcomes, including treatment response to chemotherapy (7).

DCE-MRI requires a serial acquisition of T_1-weighted images of a selected tissue of interest (TOI). As the CA is transported into the TOI, the MR signal intensity in the TOI changes and reveals information about blood flow, capillary leakage and related physiological parameters such as the volume transfer constant (K^{trans}) and extravascular extracellular volume fraction (v_e) by analyzing the MR signal time course. Quantitative physiological parameters can be estimated by fitting dynamic contrast-enhanced MRI data to an appropriate pharmacokinetic model (1). However, obtaining the arterial input function (AIF) by direct blood sampling from an artery (8) is very difficult and invasive. Several approaches for estimating AIF directly from the DCE-MRI data have been proposed (9,10). These methods have advantages of measuring the AIF on an individual basis. As an alternative approach, a reference region (RR) model does not require the AIF, and instead uses the concentration of the CA in the reference region, such as muscle, to estimate pharmacokinetic parameters (11,12).

A nonlinear least squares method with a numerical analysis (NLSQ-N) has been widely used for the analysis of DCE-MRI data using the RR model, (11,13-15). A linear least squares

method with a numerical analysis (LLSQ-N) was recently introduced and compared with the NLSQ-N method (15,16). This LLSQ-N method can estimate the kinetic parameters faster than the NLSQ-N method. However, both LLSQ-N and NLSQ-N method produce systematic error when temporal resolution is low (16,17). Planey *et al.* recommended a temporal resolution faster than 35.6 seconds to observe an error that is less than 20% in the estimated parameter using the reference region model with NLSQ-N (18).

Evaluations of the accuracy and precision of various analysis methods are critically needed to properly implement the RR model for DCE-MRI studies. The numerical analysis method has long been used in the quantification of pharmacokinetic parameters in DCE-MRI. However, a numerical analysis produces systematic error especially when temporal resolutions are low. An analytical analysis can estimate pharmacokinetic parameters accurately without representing systematic errors over various temporal resolutions (18,19). In this study, we compared LLSQ-N and NLSQ-N with an analytical nonlinear least squares method (NLSQ-A). These methods were tested with both simulation and in vivo DCE-MRI datasets. Simulated MR data were generated using an AIF model with various signal-to-noise ratios (SNRs) and temporal resolutions. In vivo DCE-MRI data were acquired from an in vivo canine model of spontaneously occurring brain tumors.

4.3 Theory

Details of the RR model have been explained previously (11,12,19). Briefly, the differential equation to estimate pharmacokinetic parameters for the two-compartment model is described by Eq. [4.1] (20,21).

$$\frac{dC_t}{dt} = K^{trans} C_p - k_{ep} C_t \qquad [4.1]$$

where C_t and C_p are the concentrations of the contrast agent in the EES and plasma space respectively, and k_{ep} is the flux rate constant ($k_{ep} = K^{trans}/v_e$). For the RR model, two differential equations of C_{TOI} (concentration in the TOI) and C_{RR} (concentration in the RR) are combined to eliminate the C_p term. The combined differential equation and its solution can be expressed in the following form:

$$\frac{dC_{TOI}(t)}{dt} = \frac{K^{trans,TOI}}{K^{trans,RR}}\frac{dC_{RR}(t)}{dt} + \frac{K^{trans,TOI}}{v_{e,RR}}C_{RR}(t) - k_{ep,TOI}C_{TOI}(t) \quad [4.2]$$

$$C_{TOI}(t) = K_R \cdot C_{RR}(t) + K_R\left(k_{ep,RR} - k_{ep,TOI}\right)\int_0^t C_{RR}(t')e^{-k_{ep,TOI}(t-t')}\,dt' \quad [4.3]$$

where K_R is defined as a ratio between the two volume transfer constants, $K^{trans,TOI}$ and $K^{trans,RR}$ (19). The concentration of CA, C_t, can be converted to the longitudinal relaxation rate constant using a linear relationship [3.4].

$$R_1 = r_1 C_t + R_{10} \quad [4.4]$$

where $R_1 = 1/T_1$, r_1 is the relaxivity (in $mM^{-1}s^{-1}$) of the CA, and R_{10} is the 'native' relaxation rate (i.e., the value of R_1 without presence of the CA). We assumed that r_1 was the same in both the TOI and RR. Substituting Eq. [4.4] into Eq. [4.3] results in the final solution for the nonlinear reference region model:

$$R'_{1,TOI}(t) = K_R R'_{1,RR}(t) + K_R V_R\left(\frac{K^{trans,RR}}{v_{e,TOI}} - \frac{1}{V_R^2}\frac{K^{trans,TOI}}{v_{e,RR}}\right)\int R'_{1,RR}(t')\cdot e^{-k_{ep,TOI}(t-t')}\,dt' \quad [4.5]$$

where $R'_{1,TOI} = R_{1,TOI} - R_{10,TOI}$ and $R'_{1,RR} = R_{1,RR} - R_{10,RR}$. Similar to K_R, V_R is the ratio between v_e for the TOI and the RR (19). The two ratios, K_R and V_R, can be derived through a nonlinear least-square curve fitting (NLSQ) according to Eq. [4.5]. Alternatively, a LLSQ-N method can be used to estimate the two ratios. The linear model for the reference region model can be obtained by integrating both side of Eq. [4.2] with Eq. [4.4]

$$R'_{1,TOI}(t) = K_R R'_{1,RR}(t) + \frac{K^{trans,TOI}}{v_{e,RR}} \int_0^t R'_{1,RR}(t')dt' - k_{ep,TOI} \int_0^t R'_{1,TOI}(t')dt' \quad [4.6]$$

This linear reference region model, Eq. [4.6], can be given in a matrix form as

$$\vec{A} = \vec{B} \cdot \vec{C}$$

where

$$\vec{A} = \begin{pmatrix} R'_{1,TOI}(t_1) \\ R'_{1,TOI}(t_2) \\ \vdots \\ R'_{1,TOI}(t_n) \end{pmatrix}, \ \vec{B} = \begin{pmatrix} K_R \\ \dfrac{K^{trans,TOI}}{v_{e,RR}} \\ k_{ep,TOI} \end{pmatrix}, \ \vec{C} = \begin{pmatrix} R'_{1,RR}(t_1) & \int_0^{t_1} R'_{1,RR}(t')dt' & -\int_0^{t_1} R'_{1,TOI}(t')dt' \\ R'_{1,RR}(t_2) & \int_0^{t_2} R'_{1,RR}(t')dt' & -\int_0^{t_2} R'_{1,TOI}(t')dt' \\ \vdots & \vdots & \vdots \\ R'_{1,RR}(t_n) & \int_0^{t_n} R'_{1,RR}(t')dt' & -\int_0^{t_n} R'_{1,TOI}(t')dt' \end{pmatrix} \quad [4.7]$$

4.4 Methods

Simulation

We used simulated data sets to investigate the accuracy and precision of all three fitting methods in calculating K_R and V_R. First, we simulated the AIF using the following equation (11):

$$C_p(t) = A \cdot t \cdot e^{-Bt} + C\left(1 - e^{-Dt}\right)e^{-Et} \quad [4.8]$$

where A=30.0 mM min^{-1}, B=4.0 min^{-1}, C=0.65 mM, D=5.0 min^{-1} and E=0.04 min^{-1} (18). The C_t curves for TOI and RR were then generated using Eq. [4.9].

$$C_t(t) = K^{trans} \int_0^t C_p(t') \cdot e^{-k_{ep,TOI}(t-t')} dt' \quad [4.9]$$

where K^{trans}=0.25 min^{-1} and v_e=0.4032 were assigned for the C_{TOI}, and K^{trans}=0.10 min^{-1} and v_e=0.10 were assigned for the C_{RR} (9). This results in a value of 2.50 for K_R and 4.03 for V_R. The simulated C_p and C_t for the TOI and RR are shown in Fig. 4.1A, and R_1 time curves converted from the simulated C_p using Eq. [4.4] are shown in Fig. 4.1B.

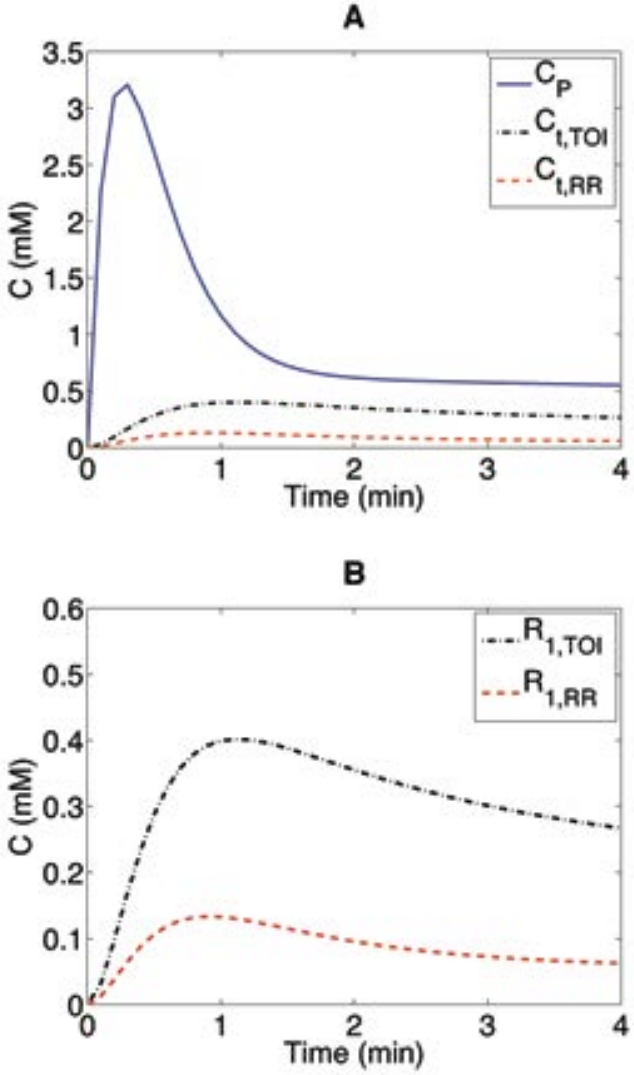

Figure 4.1 Simulated DCE-MRI data. (A) Simulated time curve for the concentration of CA in the blood plasma (C_p) of the TOI and RR, and the concentrations of CA in the TOI ($C_{t,TOI}$), and RR ($C_{t,RR}$), and (B) the R_1 time curve for TOI and RR converted from the C_p time curve.

To test precision of the three methods, we conducted the simulation process with three temporal resolutions and four signal-to-noise ratios (SNR). The original AIF and C_t curves were

discretized with a sampling rate of 4, 6, 30, and 60 seconds, respectively. The SNR was set at 50, 20, 10, and 7 where $SNR = \mu / \sigma$, μ is the signal mean and σ is the standard deviation of the noise. For each setting this entire process was repeated one hundred times to produce means and standard deviations for the two ratio parameters. To investigate the effect of temporal resolutions on accuracy, we also evaluated the mean percentage error (MPE) for K_R and V_R.

$$MPE = \frac{1}{N}\left(\sum_{j=1}^{N}\frac{\hat{P}_j - P}{P}\right)\times 100\% \qquad [4.10]$$

where $\hat{P}_j$ and P are the estimated and known values of K_R and V_R, and $N=100$ is the number of simulations performed.

The linear reference region model method (Eq. [4.6]) estimates the two ratio parameters, K_R and V_R, using LSQ methods and numerical integration with the trapezoidal rule. The nonlinear reference region model method (Eq. [4.5]) extracts the two ratio parameters by using NLSQ integrated with either a numerical analysis or an analytical analysis. For the NLSQ-A method, we first applied the nonlinear regression analysis on the simulated R_1 data for the RR. The relaxation rate, R_1, for RR can be obtained by substituting Eq. [4.8] into Eq. [4.9] and then into Eq. [4.4]

$$\begin{aligned} R_1(t) = r_1 \cdot A_6 \cdot e^{-A_7 \cdot t}\Bigg[& \frac{A_1 \cdot t}{A_7 - A_2} e^{(A_7 - A_2)t} - \frac{1}{(A_7 - A_2)^2} \\ & \times\left(e^{(A_7 - A_2)t} - 1\right) + \frac{A_3}{A_7 - A_5}\left(e^{(A_7 - A_5)t} - 1\right) \\ & - \frac{A_3}{A_7 - A_4 - A_5}\left(e^{(A_7 - A_4 - A_5)t} - 1\right)\Bigg] \end{aligned} \qquad [4.11]$$

where A_1 through A_7 are parameters that can be extracted from a nonlinear regression analysis using a NLSQ method. Next, we applied this R_1 model to Eq. [4.5] and then applied a curve-

fitting routine to extract the parameters K^{trans} and v_e for the TOI and v_e for the RR, while K^{trans} for the RR was assigned a value of 1.0 min^{-1}. Then we calculated the ratios K_R and V_R between the TOI and the RR. The details about this NLSQ-A method were introduced and explained previously (19).

In vivo Experiments

Seven canines with spontaneous occurring brain tumors were imaged using a 3.0 Tesla GE SIGNA HDX MR scanner (GE Medical Systems, Milwaukee, WI, USA). A spoiled gradient echo sequence was scanned before contrast agent was injected to measure tissue relaxation rate, R_{10}, with the following parameters: variable flip angles of 15^0, 30^0, 45^0, 60^0 and 75^0, repetition time (TR) of 400 ms and echo time (TE) of 2.24 ms. The DCE-MRI protocol employed a standard T_1-weighted, 2-D gradient refocused echo sequence to obtain dynamic serial images with the following parameters: TR of 34 ms, TE of 2.78 ms, 35° flip angle, matrix size of 192×192, field of view (FOV) of 182.25 cm^2, a total of 5 slices, slice thickness of 3 mm, and NEX=1, scan time of 5.9 minutes (a total of 41 acquisitions and a temporal resolution of 8.7 seconds). The relaxation time courses were estimated by using the R_{10} map, given by the following Eq. [4.12] (22).

$$R_1(t) = \frac{1}{T_R} \ln\left[\left(\rho_0 \sin\theta - \rho(t)\cos\theta\right) / \left(\rho_0 \sin\theta - \rho(t)\right)\right] \qquad [4.12]$$

where ρ is signal intensity and ρ_0 is fully relaxed magnetization for a given voxel.

For six of the seven datasets, thirty voxels were selected manually from suspected lesion tissue as the TOI and thirty voxels from bilateral normal brain tissue as the RR, respectively. For dataset 4, twelve voxels were selected because the lesion had a small size. The temporal

resolution was approximately 8.7 seconds and the MR scan took 5 minutes 56 seconds for the first 5 datasets and 5 minutes 4 seconds for the last 2 datasets. The average SNR was 14.1 for all *in-vivo* datasets.

The Kruskal-Wallis test (KW) test (23), a nonparametric method for testing equality of population medians among groups, was used to determine whether the methods differed significantly from each other using the two ratios, *KR* and *VR*, for in vivo datasets by comparing the distribution of all voxel within the ROI. Following the KW test, a nonparametric pairwise two-sample Kolmogorov-Smirnov (KS) test was used to determine whether any two methods differed. The null hypothesis for this test is that two datasets are from the same continuous distribution, implying that two datasets from each method are not different.

4.5 Results

Simulations

Values of K_R and V_R were estimated using each method with five SNR levels (infinitive, 50, 20, 10, and 7, where the infinitive SNR represents that no noise was included in the simulated signal) and three temporal resolutions (4 sec, 6 sec, 30 sec, and 60 sec) (Fig. 4.2). For the dataset without noise and at a high temporal resolution of 4 seconds, K_R was estimated to be 2.47, 2.44, and 2.50 by the LLSQ-N, NLSQ-N, and NLSQ-A methods, respectively, which all agreed well with the value of 2.50 used in construct the simulated data. Similarly, V_R was estimated to

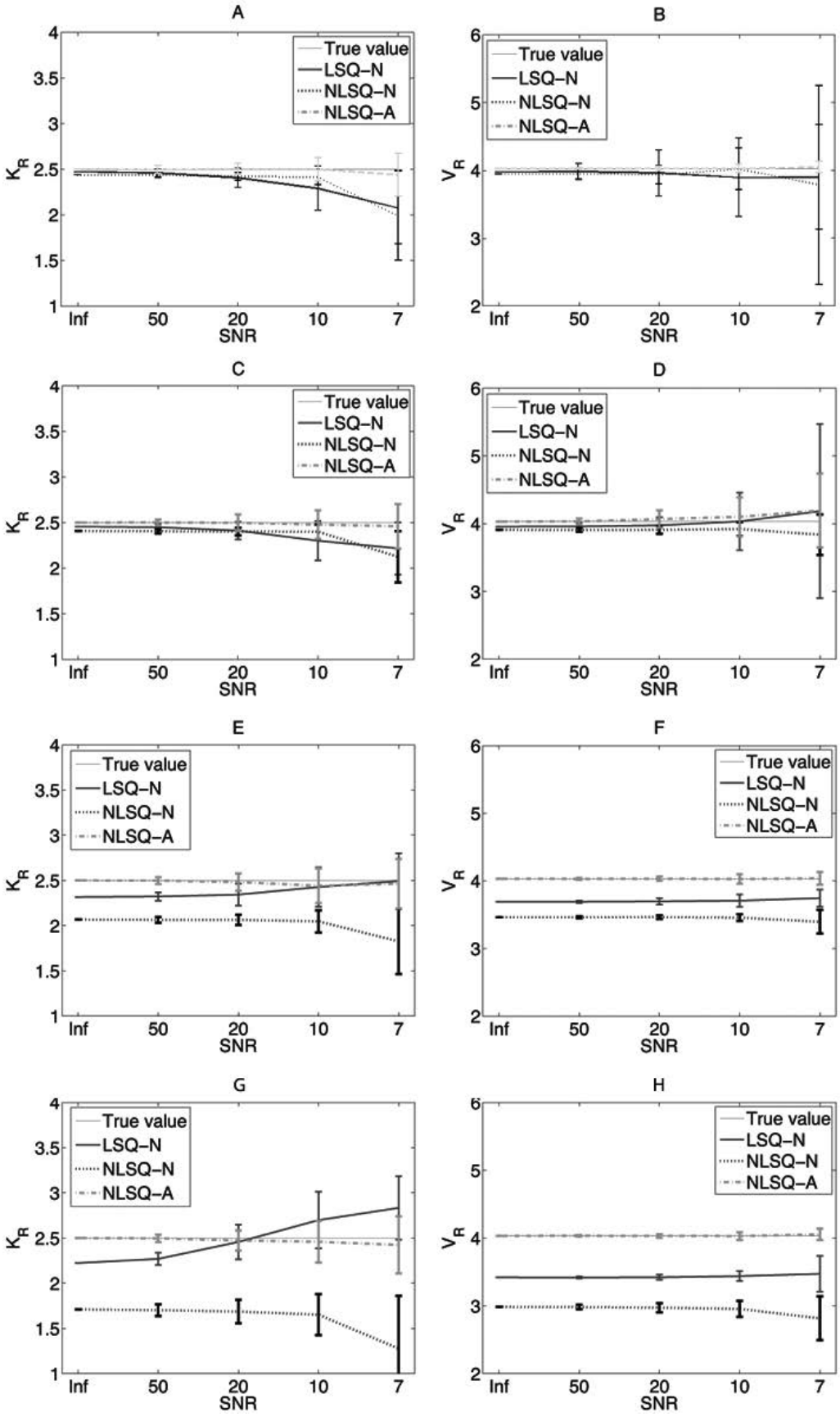
A
B
C
D
E
F
G
H
True value
LSQ–N
NLSQ–N
NLSQ–A
K_R
V_R
SNR
Inf
50
20
10
7

Figure 4.2 The pharmacokinetic parameter ratios K_R (first column) and V_R (second column) were estimated from the simulation study as a function of various temporal sampling rates of 4 sec. (first row), 6 sec. (second row), 30 sec. (third row), and 60 sec. (fourth row) and SNR levels. The x-axis displays the SNR levels (SNR decreases from left to right), where "Inf" represents that no noise was added. The horizontal solid line labeled as "true value" represents the value used to construct the simulation.

be 3.98, 3.95, and 4.03 by the LLSQ-N, NLSQ-N, and NLSQ-A methods, respectively, which were close to the value of 4.032 that was used in the simulations. For comparison, at a low temporal resolution of 60 seconds without noise, K_R was estimated to be 2.22, 1.71, and 2.50, and V_R was estimated to be 3.42, 2.98, and 4.03 by the respective methods. This result indicated that only the NLSQ-A method was insensitive to temporal resolution.

To investigate the precision of the three methods at various noise levels and temporal resolutions, we evaluated the results in terms of the mean value and the standard deviation (Table 4.1). The estimated values of K_R and V_R using NLSQ-A were very close to the original assigned values of 2.5 and 4.03, respectively. This trend persisted over the studied temporal resolutions from 4 seconds to 60 seconds, respectively. The results for the LLSQ-N and NLSQ-N shows that the numerical method systematically underestimated the ratios K_R and V_R, and these systematic errors increased as the temporal resolution was decreased. The MPE was calculated for the case without added noise to investigate the systematic error and was shown in the last column of Table 4.1. For the high temporal resolution of 4 sec., MPE of K_R and V_R for LLSQ-N were 1.20 % and 1.29 %, respectively. For the low temporal resolution, 60 sec., MPE of K_R and V_R for LLSQ-N were 11.20 % and 15.14 %, respectively. The NLSQ-N method has the highest MPE of K_R and V_R among the three methods, while the NLSQ-A method has the lowest values of MPE for both K_R and V_R, which are less than 7.0×10^{-5} % for all temporal resolutions.

Table 4.1 Results of simulated dataset for K_R (Table 4.1A) and V_R (Table 4.1B), with different SNRs (in columns) and temporal resolutions (in rows)

Table 4.1A

Temporal resolution	Ratio	No noise	SNR 50	SNR 20	SNR 10	SNR 7	MPE (%)
				LLSQ-N			
4 sec.	K_R	2.47	2.46± 0.04	2.40± 0.11	2.29± 0.24	2.07± 0.38	1.20
6 sec.	K_R	2.45	2.45± 0.04	2.41± 0.10	2.30± 0.22	2.22± 0.29	2.00
30 sec.	K_R	2.32	2.33± 0.05	2.35± 0.12	2.43± 0.22	2.49± 0.31	7.20
60 sec.	K_R	2.22	2.27± 0.07	2.46± 0.19	2.70± 0.31	2.83± 0.35	11.20
				NLSQ-N			
4 sec.	K_R	2.44	2.43± 0.02	2.42± 0.05	2.41± 0.08	2.00± 0.49	2.50
6 sec.	K_R	2.41	2.40± 0.02	2.40± 0.04	2.40± 0.08	2.12± 0.28	3.60
30 sec.	K_R	2.07	2.06± 0.03	2.06± 0.06	2.05± 0.12	1.83± 0.36	17.20
60 sec.	K_R	1.71	1.70± 0.06	1.69± 0.13	1.65± 0.23	1.28± 0.58	31.60
				NLSQ-A			
4 sec.	K_R	2.50	2.50± 0.03	2.50± 0.08	2.50± 0.16	2.43± 0.28	3.5×10^{-5}
6 sec.	K_R	2.50	2.50± 0.03	2.50± 0.09	2.48± 0.16	2.46± 0.24	3.6×10^{-5}
30 sec.	K_R	2.50	2.50± 0.04	2.48± 0.10	2.44± 0.19	2.46± 0.27	4.5×10^{-6}
60 sec.	K_R	2.50	2.50± 0.04	2.47± 0.11	2.46± 0.23	2.42± 0.31	3.3×10^{-5}

Table 4.1B

Temporal resolution	Ratio	No noise	SNR 50	SNR 20	SNR 10	SNR 7	MPE (%)
				LLSQ-N			
4 sec.	V_R	3.98	3.98± 0.12	3.99± 0.34	3.97± 0.50	3.90± 0.77	1.29
6 sec.	V_R	3.96	3.96± 0.05	3.97± 0.12	4.03± 0.43	4.18± 1.28	1.74
30 sec.	V_R	3.69	3.69± 0.02	3.70± 0.05	3.71± 0.09	3.75± 0.13	8.44
60 sec.	V_R	3.42	3.42± 0.02	3.42± 0.04	3.44± 0.07	3.47± 0.26	15.14
				NLSQ-N			
4 sec.	V_R	3.95	3.95± 0.08	3.94± 0.14	4.02± 0.31	3.86± 0.96	2.02
6 sec.	V_R	3.91	3.91± 0.03	3.91± 0.06	3.92± 0.10	3.84± 0.30	2.98
30 sec.	V_R	3.46	3.46± 0.01	3.46± 0.03	3.46± 0.05	3.40± 0.18	14.14
60 sec.	V_R	2.98	2.98± 0.03	2.97± 0.07	2.96± 0.12	2.81± 0.32	26.05
				NLSQ-A			
4 sec.	V_R	4.03	4.04± 0.04	4.05± 0.12	4.19± 0.36	4.20± 0.82	4.2×10^{-5}
6 sec.	V_R	4.03	4.03± 0.04	4.07± 0.13	4.10± 0.29	4.19± 0.54	4.3×10^{-5}
30 sec.	V_R	4.03	4.03± 0.01	4.03± 0.03	4.03± 0.07	4.04± 0.09	6.4×10^{-5}
60 sec.	V_R	4.03	4.03± 0.01	4.03± 0.03	4.03± 0.06	4.05± 0.08	6.8×10^{-5}

The mean percentage error (MPE) listed in the last column was only evaluated for the case when no noise was added (the 3rd column).

For the case of added noise, there is a small difference between the three methods in terms of standard error as shown in Table 4.1. Regarding the performance when realistic levels of noise are included, e.g. at SNR level of 10, the numerical methods in the simulation study showed that there is a big difference between high temporal resolution and low temporal resolution (regarding K_R, 16.0% differencefor LLSQ-N and 37.0% difference for NLSQ-N; regarding V_R, 15.8% difference for LLSQ-N and 27.9% difference for NLSQ-N), while analytical method does not have such a difference between high and low temporal resolutions (0.008% and 0.034% differences for K_R and V_R, respectively).

In vivo Experiments

For the in vivo experiments of seven canine brain lesions, the data were analyzed on a voxel-by-voxel basis to calculate K_R and V_R. Fig. 4.3 shows images of the seven canine brain lesions, indicated with arrows, and Fig. 4.4 shows the representative R_1 curves of the TOI and RR corresponding to each in vivo dataset. The SNR of the seven datasets ranged from 10 to 18 for the TOI and RR of the all datasets, and this range was within the SNRs tested in the simulation study.

The K_R and V_R obtained from NLSQ-A have a higher value than those from the other two methods, except the values of K_R and V_R estimated from dataset 5 (Table 4.2A). Specifically, K_R estimated from the numerical analysis methods has a much smaller value than the K_R estimated from the analytical analysis method, which is consistent with the simulation using different C_p curves. V_R from LLSQ-N has a much smaller value than the V_R from the NLSQ-N and NLSQ-A.

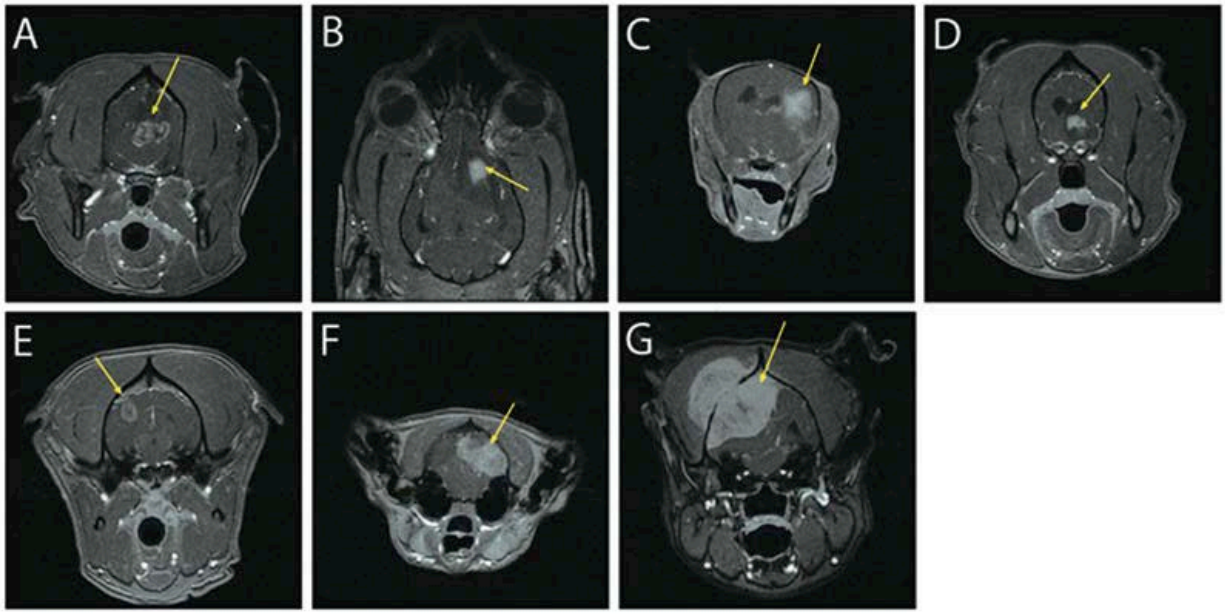

Figure 4.3 Seven canine brain images with 3 cases (A, C, and D) of presumptive glioma, 2 cases (B and D) of presumptive meningloma, 1 case (E) of meningloma, and 1 case (G) of multilobulated tumor of bone. The enhanced tumor area in each case was pointed with an arrow. The presumptive diagnosis was reached based on the MRI characteristics of the lesion including anatomic location, discrete margins, singal intensity on T_1-weighted images, and enhancement pattern after administration of contrast medium. Data 1 through Data 7 in Table 3 correspond to Fig. 3A through Fig. 3G.

The results for the Kruskal-Wallistest test, where the p-value is close to zero for both K_R and V_R, indicates that there is a statistically significant difference among the three methods (Table 4.2B). A Kolmogorov-Smirnov test showed that the p-values for both K_R and V_R between three methods for all datasets are less than 0.05, indicating that the methods are statistically different with a 5% significance level.

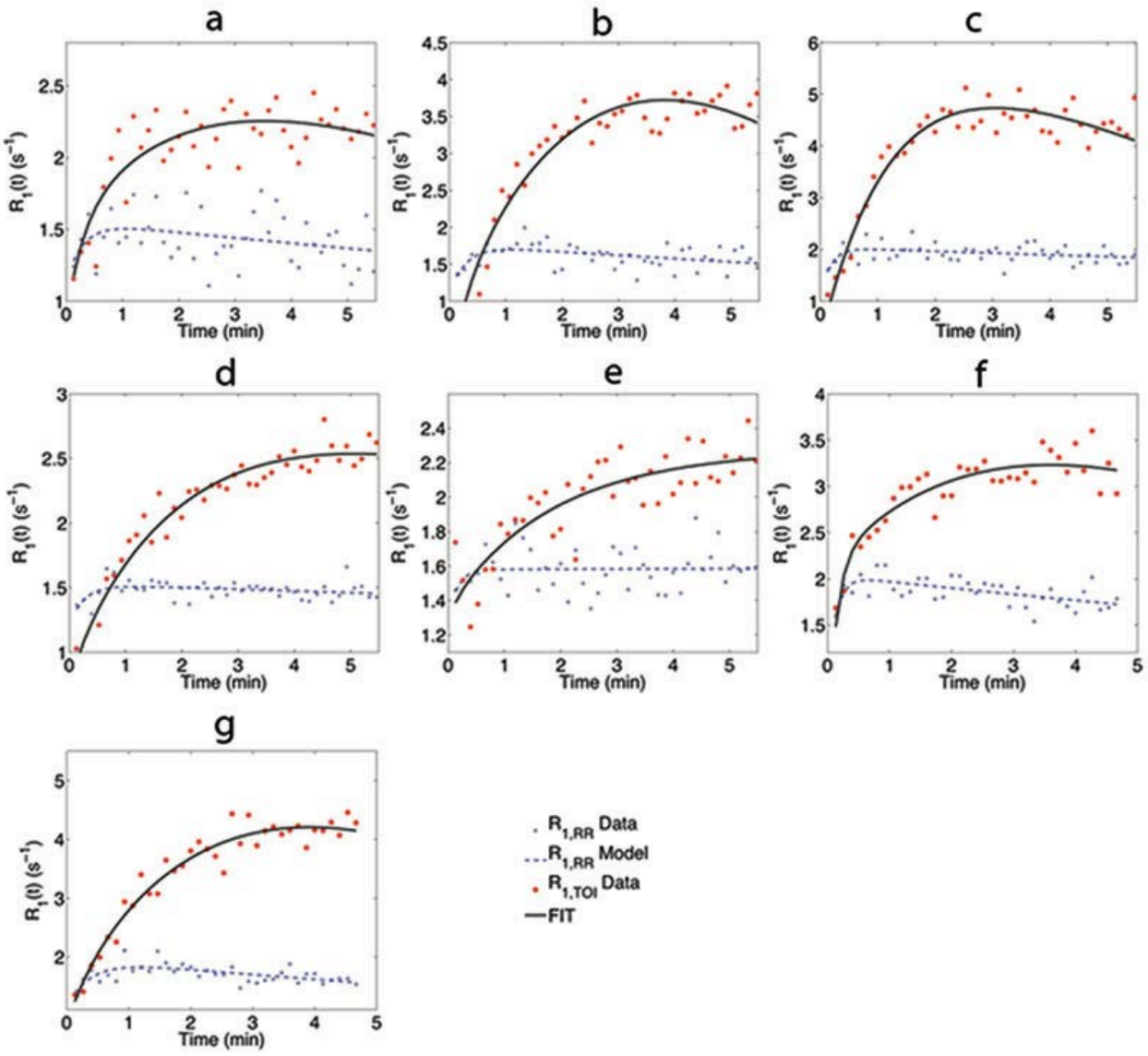

Figure 4.4 Representative R_1 curves corresponding to each canine dataset for TOI and RR in Fig. 3 (A~G). Each R_1 curve is plotted from one representative voxel randomly selected from the dataset.

4.6 Discussion

Several models have been developed for the analysis of DCE-MRI data including reference region model (11,24-26). In this study, we compared three different methods, LLSQ-N, NLSQ-N, and NLSQ-A, for analyzing the kinetic parameter ratios, K_R and V_R. For different temporal resolutions, the results from our simulations indicated that both LLSQ-N and NLSQ-N method produce a systematic error, and the error increases when temporal resolution is decreased. Meanwhile, the NLSQ-A method does not show this systematic error. When the temporal resolution is low (60 sec.), the NLSQ-N method has the biggest systematic error for both K_R and V_R.

One drawback of the NLSQ-A method is that a regression model with the proper form of the AIF for the TOI and RR is required to accurately estimate the kinetic parameter ratios K_R and V_R. In this study, we have performed the simulation based on a biexponential AIF form (Eq. [4.8]) from a low-molecular-weight contrast agent such as the gadolinium diethylenetriamine pentaacetic acid (Gd-DTPA), which is in widespread clinical use. This biexponential form was used to find regression model (Eq. [4.11]). If a macromolecular contrast agent such as albumin-(Gd-DTPA) is used, a monoexponential form should be used to find a different regression model (27-29). Also, when R_1 curves of the TOI and the RR do not follow the same trend, for example one curve increasing while another one decreasing, the resulting reference region model cannot fit the R_1 curve of the TOI well. This is likely for cases when the TOI and reference regions do not share the same artery for blood supply, or the same AIF.

Table 4.2 Results of K_R and V_R and Kruskal-Wallis test for in vivo dataset

Table 4.2A. Results of in vivo dataset

Data sets	SNR	K_R			V_R		
		LLSQ-N	NLSQ-N	NLSQ-A	LLSQ-N	NLSQ-N	NLSQ-A
Data 1	10.80 ± 1.13	0.81 ± 0.06	0.52 ± 0.13	1.70 ± 0.27	1.48 ± 0.12	3.63 ± 0.47	4.80 ± 1.28
Data 2	11.43 ± 0.91	0.28 ± 0.08	0.26 ± 0.18	3.11 ± 0.98	2.43 ± 1.47	19.59± 2.09	19.16± 2.13
Data 3	13.80± 1.82	0.47 ± 0.12	0.01 ± 0.05	1.77 ± 0.41	2.31 ± 0.21	12.23± 1.47	13.55± 1.70
Data 4	13.39± 1.82	0.67 ± 0.06	0.66 ± 0.18	1.75 ± 0.43	2.02 ± 0.30	9.26 ± 1.84	10.67± 2.35
Data 5	13.11± 1.28	0.91 ± 0.08	0.12 ± 0.08	0.63 ± 0.27	1.58 ± 0.13	2.85 ± 0.44	2.82 ± 0.46
Data 6	17.98± 1.88	1.10 ± 0.11	1.29 ± 0.11	2.44 ± 0.53	2.02 ± 0.17	2.75 ± 0.29	7.73 ± 1.73
Data 7	17.98 ± 2.02	0.65 ± 0.06	0.41 ± 0.17	1.08 ± 0.27	2.56 ± 0.11	8.31 ± 0.56	9.12 ± 0.76

Table 4.2B. Kruskal-Wallis test for in vivo dataset

		Data 1	Data 2	Data 3	Data 4	Data 5	Data 6	Data 7
K_R	χ^2	78.4	71.8	78.4	59.3	25.5	56.1	70.5
	p	9.3×10^{-18}	2.6×10^{-16}	2.6×10^{-17}	1.3×10^{-13}	2.9×10^{-6}	6.8×10^{-13}	5.0×10^{-16}
V_R	χ^2	73.5	28.6	74.7	62.3	24.6	73.0	66.9
	p	1.8×10^{-16}	6.2×10^{-7}	5.9×10^{-17}	3.0×10^{-14}	4.5×10^{-6}	1.4×10^{-16}	2.9×10^{-15}

Chi-squared (χ^2) distribution and p-values are listed for K_R and V_R for each in vivo dataset, respectively.

For in vivo experiments, the estimated ratios from the numerical analyses were lower than those from the analytical analysis. Particularly, the K_R from the numerical analyses has a much smaller value than the K_R from the analytical analysis. This is similar to the simulation results, with the exception of dataset 5 (which seems to be an outlier). Also, it is noted that the

V_R from the LLSQ-N has a much smaller value than the V_R from NLSQ-A methods, but the V_R from the NLSQ-N is close to the V_R from the NLSQ-A. In dataset 5, the K_R from NLSQ-A is 0.63, which is smaller than the K_R from LLSQ-N; in addition, the V_R from NLSQ-N has a higher value than the other two methods. There might be several factors that may contribute to these errors. For example, the dataset 5 did not show a complete enhancing curve due to the short total scan time. Another possibility is that the TOI and RR may not share the same artery (i.e., leading to different C_p).

In summary, we have compared three different methods to analyze the DCE-MRI data and estimate pharmacokinetic parameter ratios on a voxel-by-voxel basis using both simulation and in vivo studies. We have shown that the NLSQ-A method can estimate pharmacokinetic parameter ratios K_R and V_R more accurately than the numerical methods, without representing systematic errors over various temporal resolutions and SNRs. The major limitation for the NLSQ-A, however, is that it requires a proper regression model for the RR to analyze the data accurately.

4.7 References

1. Tofts PS, Brix G, Buckley DL, Evelhoch JL, Henderson E, Knopp MV, Larsson HB, Lee TY, Mayr NA, Parker GJ and others. Estimating kinetic parameters from dynamic contrast-enhanced T(1)-weighted MRI of a diffusable tracer: standardized quantities and symbols. J Magn Reson Imaging 1999;10(3):223-32.
2. Padhani AR, Leach MO. Antivascular cancer treatments: functional assessments by dynamic contrast-enhanced magnetic resonance imaging. Abdom Imaging 2005;30(3):324-41.

3. Miller JC, Pien HH, Sahani D, Sorensen AG, Thrall JH. Imaging angiogenesis: applications and potential for drug development. J Natl Cancer Inst 2005;97(3):172-87.

4. Zhao Q, Lee S, Kent M, Schatzberg S, Platt S. Dynamic contrast-enhanced magnetic resonance imaging of canine brain tumors. Vet Radiol Ultrasound 2010;51(2):122-9.

5. Workie DW, Dardzinski BJ, Graham TB, Laor T, Bommer WA, O'Brien KJ. Quantification of dynamic contrast-enhanced MR imaging of the knee in children with juvenile rheumatoid arthritis based on pharmacokinetic modeling. Magn Reson Imaging 2004;22(9):1201-10.

6. Jansen JFA, Schoder H, Lee NY, Wang Y, Pfister DG, Fury MG, Stambuk HE, Humm JL, Koutcher JA, Shukla-Dave A. Noninvasive Assessment of Tumor Microenvironment Using Dynamic Contrast-Enhanced Magnetic Resonance Imaging and (18)F-Fluoromisonidazole Positron Emission Tomography Imaging in Neck Nodal Metastases. International Journal of Radiation Oncology Biology Physics 2010;77(5):1403-1410.

7. Evelhoch J, Garwood N, Vigneron D, Knopp N, Sullivan D, Menkens A, Clarke L, Liu GY. Expanding the use of magnetic resonance in the assessment of tumor response to therapy: Workshop report. Cancer Res 2005;65(16):7041-7044.

8. Benjaminsen IC, Brurberg KG, Ruud EB, Rofstad EK. Assessment of extravascular extracellular space fraction in human melanoma xenografts by DCE-MRI and kinetic modeling. Magn Reson Imaging 2008;26(2):160-70.

9. Rijpkema M, Kaanders JH, Joosten FB, van der Kogel AJ, Heerschap A. Method for quantitative mapping of dynamic MRI contrast agent uptake in human tumors. J Magn Reson Imaging 2001;14(4):457-63.

10. van Osch MJ, Vonken EJ, Viergever MA, van der Grond J, Bakker CJ. Measuring the arterial input function with gradient echo sequences. Magn Reson Med 2003;49(6):1067-76.

11. Yankeelov TE, Luci JJ, Lepage M, Li R, Debusk L, Lin PC, Price RR, Gore JC. Quantitative pharmacokinetic analysis of DCE-MRI data without an arterial input function: a reference region model. Magn Reson Imaging 2005;23(4):519-29.

12. Yang C, Karczmar GS, Medved M, Stadler WM. Estimating the arterial input function using two reference tissues in dynamic contrast-enhanced MRI studies: fundamental concepts and simulations. Magn Reson Med 2004;52(5):1110-7.

13. Lee J. Quantification of DCE-MRI: pharmacokinetic parameter ratio between TOI and RR in reference region model. Conf Proc IEEE Eng Med Biol Soc 2010;2010:2837-40.

14. Orton MR, d'Arcy JA, Walker-Samuel S, Hawkes DJ, Atkinson D, Collins DJ, Leach MO. Computationally efficient vascular input function models for quantitative kinetic modelling using DCE-MRI. Phys Med Biol 2008;53(5):1225-39.

15. Murase K. Efficient method for calculating kinetic parameters using T1-weighted dynamic contrast-enhanced magnetic resonance imaging. Magn Reson Med 2004;51(4):858-62.

16. Cardenas-Rodriguez J, Howison CM, Pagel MD. A linear algorithm of the reference region model for DCE-MRI is robust and relaxes requirements for temporal resolution. Magn Reson Imaging 2012;doi: 10.1016/j.mri.2012.10.008.

17. Larsson C, Kleppesto M, Rasmussen I, Jr., Salo R, Vardal J, Brandal P, Bjornerud A. Sampling requirements in DCE-MRI based analysis of high grade gliomas: Simulations and clinical results. J Magn Reson Imaging 2013;37(4):818-29.

18. Planey CR, Welch EB, Xu L, Chakravarthy AB, Gatenby JC, Freehardt D, Mayer I, Meszeoly I, Kelley M, Means-Powell J and others. Temporal sampling requirements for reference region modeling of DCE-MRI data in human breast cancer. J Magn Reson Imaging 2009;30(1):121-34.

19. Lee J, Platt S, Kent M, Zhao Q. An analysis of the pharmacokinetic parameter ratios in DCE-MRI using the reference region model. Magn Reson Imaging 2012;30(1):26-35.

20. Tofts PS. Modeling tracer kinetics in dynamic Gd-DTPA MR imaging. J Magn Reson Imaging 1997;7(1):91-101.

21. Tofts PS, Cutajar M, Mendichovszky IA, Peters AM, Gordon I. Precise measurement of renal filtration and vascular parameters using a two-compartment model for dynamic contrast-enhanced MRI of the kidney gives realistic normal values. Eur Radiol 2012;22(6):1320-30.

22. Landis CS, Li X, Telang FW, Coderre JA, Micca PL, Rooney WD, Latour LL, Vetek G, Palyka I, Springer CS. Determination of the MRI contrast agent concentration time course in vivo following bolus injection: Effect of equilibrium transcytolemmal water exchange. Magnetic Resonance in Medicine 2000;44(4):563-574.

23. Kruskal WH, Wallis WA. Use of ranks in one-criterion variance analysis. Journal of the American statistical Association 1952;47(260):583-621.

24. Kuwatsuru R, Shames DM, Muhler A, Mintorovitch J, Vexler V, Mann JS, Cohn F, Price D, Huberty J, Brasch RC. Quantification of tissue plasma volume in the rat by contrast-enhanced magnetic resonance imaging. Magn Reson Med 1993;30(1):76-81.

25. Tofts PS, Kermode AG. Measurement of the blood-brain barrier permeability and leakage space using dynamic MR imaging. 1. Fundamental concepts. Magn Reson Med 1991;17(2):357-67.

26. Brix G, Semmler W, Port R, Schad LR, Layer G, Lorenz WJ. Pharmacokinetic parameters in CNS Gd-DTPA enhanced MR imaging. J Comput Assist Tomogr 1991;15(4):621-8.

27. Irrechukwu ON, Lin PC, Fritton K, Doty S, Pleshko N, Spencer RG. Magnetic resonance studies of macromolecular content in engineered cartilage treated with pulsed low-intensity ultrasound. Tissue Eng Part A 2011;17(3-4):407-15.

28. Schmiedl U, Ogan MD, Moseley ME, Brasch RC. Comparison of the contrast-enhancing properties of albumin-(Gd-DTPA) and Gd-DTPA at 2.0 T: and experimental study in rats. AJR Am J Roentgenol 1986;147(6):1263-70.

29. Bauer WR, Schulten K. Theory of contrast agents in magnetic resonance imaging: coupling of spin relaxation and transport. Magn Reson Med 1992;26(1):16-39.

CHAPTER 5

TUMOR SEGMENTATION USING TEMPORAL INDEPENDENT COMPONENT ANALYSIS FOR DCE-MRI[1]

[1] Lee J, Kent M, Platt S, and Zhao Q. To be submitted to *NeuroImage*

5.1 Abstract

Purpose: To introduce the temporal independent component analysis (ICA) to solve partial volume effect (PVE) in brain tumor segmentation. Also, the performance of the temporal ICA is compared to spatial ICA and expert's manual delineation of tumor.

Theory and Methods: Comparison was performed based on three methods: percent volume overlap or Dice's coefficient, percent volume difference, and Pearson correlation coefficient between two areas in size. Seven in vivo DCE-MRI datasets from a canine model of spontaneously occurring brain tumors were segmented with each method.

Results: Pearson's correlation coefficient between the lesion areas segmented by spatial ICA and the expert's manual delineation, between temporal ICA and manual delineation, and between spatial ICA and temporal ICA were 0.9957, 0.9937, and 0.9844, respectively. The results of each method were also compared using the percent volume overlap and the percent volume difference between two regions. The mean values of percent volume overlap and percent volume difference were, respectively, 76.00% and 38.07% between spatial ICA and manual segmentation; 81.11% and 24.84% between temporal ICA and manual segmentation; and 79.44% and 29.94% between the two ICA segmentation methods.

Conclusion: The performance of two ICA methods for segmenting tumor is very close to that of the expert's delineation method. However, the temporal ICA has the benefit over the spatial ICA method in its ability to separate independent tissue signals in a voxel containing two or more types of tissues.

Key Words:

DCE-MRI; Independent component analysis; temporal ICA; spatial ICA; Brain tumors

5.2 Introduction

Dynamic Contrast-enhanced magnetic resonance imaging (DCE-MRI) is widely used in a cancer-imaging tool. It is a noninvasive, clinical imaging technique that involves the study of tumor angiogenesis (1) and in the development and trial assessment of antiangiogenic and vascular disrupting compounds (2). Also, the studies of DCE-MRI includes, but are not limited to, noninvasive assessment of tumor microenvironment (3), predictors of clinical outcomes including treatment response to chemotherapy (4,5), detection of rheumatoid arthritis (6,7), differentiation of tumor histopathology (8,9), and analysis of the pharmacokinetic parameters (10). With a high sensitivity of MRI, it has been widely applied to improve tumor detection and diagnosis (11). In particular, the tissue classification and anatomical segmentation are increasingly studied through MRI. Due to a growing the amount of MRI data, the automated method is required to develop accurate and reliable image analysis for classifying image regions. As a result, many automated computer-aided methods are proposed such as the region-growing method to segment lesions (12), automated segmentation methods based on artificial intelligence techniques (13), segmentation based on statistical pattern recognition techniques (14), a semiautomatic algorithm based on the fuzzy c-means clustering (15), a user-interaction-threshold method to extract the region of interest (ROI) (16), and a detection of deviations from normal brains using a multi-layer Markov random field framework (17). Recently, independent component analysis (ICA) has been introduced to the field of DCE-MRI for the detection and characterization of breast lesions (18), and identification of breast lesions as separate hemodynamic sources (19).

In DCE-MRI, it requires repeated acquisition of T_1-weighted images of a particular tissue of interest (TOI) before, during and after an intravenous administration of a bolus of a

paramagnetic contrast agent (CA), typically a low-molecular weight gadolinium (Gd) compound. The contrast uptake curves in a TOI or voxels are often fitted using a pharmacokinetic model to give physiological information about blood flow, capillary leakage and related physiological parameters. In general, tumor tissues show a high and fast contrast uptake due to abundance of angiogenic microvessels in tumor tissues and normal tissues or benign tissues show no enhancement curves or slow sustained enhancement curves. In the studies of the detection and classification of tumor on DCE-MRI data, the independent component analysis (ICA) methods were recently used to identify breast tumor (19). Also, application of ICA on DCE-MRI includes calculation of intravascular signal (20), removing undersampling artifacts (21), and assessment of cerebral blood perfusion (22).

Independent component analysis (ICA) is a special case of blind source separation (BSS) that separates a set of signals from a set of mixed signals without information of the source signals. During the last decade, ICA becomes one of the most widely used statistical and computational method that can separate a multivariate signal into the original source signals by assuming that components are both statistically independent and nongaussian. Several different algorithms have been proposed from different approach such as the maximum likelihood estimation (MLE) that is a method of estimating the parameters of a statistical model, nonlinear PCA (NLPCA) algorithm that is the nonlinear equivalent of classical PCA, and reduces the observed variables to a number of uncorrelated principal component developed by Karhunen and Joutsensale (1994) and Oja (1995), the information maximization algorithm (infomax algorithm) by Bell and Sejnowski (23), Joint approximate diagonalization of eigen-matrices (JADE) that is equivalent to informatics approaches and employs approximate joint diagonalization of fourth-order cumulant matrices proposed by Cardoso and Souloumiac (24), and FastICA that is an

efficient and popular algorithm based on fixed-point iteration and maximizing non-Gaussianity proposed by Aapo Hyvärinen (25).

In the studies of tumor segmentation using MR data, partial volume effect (PVE) is one of the major difficulties and may result in inaccurate segmentation results due to inherent low spatial resolution of images (26). PVE occurs when more than one tissue type presents in a voxel and it blurs the intensity distinction at the border of two tissues such as the tumor and normal tissues. Previously, ICA has been used to solve the PVE on large blood vessel (27) and arterial input function (28) in microPET.

In this study, seven in vivo DCE-MRI datasets from a canine model of spontaneously occurring brain tumors were used with ICA. There are two complementary ways in ICA to decompose signals into original source signals, spatial ICA and temporal ICA. The Spatial ICA finds a set of mutually independent spatial images such as tumor or normal tissue (29), while temporal ICA finds a set of independent time courses such as enhancing time curves in DCE-MRI (23,30-32). To resolve this difficulty presented by PVE in the segmentation of the canine brain tumor, this study uses temporal ICA, which intends to separate two intrinsic tissues at the border. Although ICA has been used to discriminate source signals from biological mixture signals for DCE-MRI data (20), to the best of our knowledge temporal ICA has never been implemented in the segmentation of DCE-MRI. The temporal ICA method was also compared with the spatial ICA and the manual delineation of the lesions by an expert was taken as a reference standard in evaluating the methods.

5.3 Theory

ICA is a statistical and computational technique that extracts individual source signals from the measured mixture signals by means of statistical independence of the non-Gaussian source signals. A simple form of the ICA problem can be expressed by the following linear model:

$$x_i = a_{i1}s_1 + a_{i2}s_2 + ... + a_{in}s_n, \quad (i = 1, 2, \ldots, n) \qquad [5.1]$$

where $s_1, \ldots, s_n$ are the original source signals, a_{ij} (j = 1,…,n) are weighting coefficients, and x_i is the mixture signal which is weighted sums of the s_j. In this basic ICA model, we assume that each mixture x_i and each independent component s_i is a random variable. To simplify the method and algorithm without loss of generality, we can perform centering the observable variables by subtracting their sample mean so that both the mixture variables and the independent components have zero mean. Another useful technique that is called whitening was performed as preprocessing using principal component analysis (PCA) and eigenvalue decomposition (EVD). The purpose of whitening is to make the components uncorrelated and their variances to be unity (31). For the convenience, we can rewrite this model into vector-matrix notation

$$\mathbf{X = AS} \qquad [5.2]$$

where **X** is the $m \times n$ measured data matrix and both **A** and **S** are unknown, and need to be estimated using ICA under the assumption that the component s_j are statistically independent. We can obtain the independent component simply by

$$\mathbf{Y = WX} \qquad [5.3]$$

where **Y** is the estimated independent source signals and W is the unmixing matrix, and Y can be estimated by setting up a cost function which either maximizes the nongaussianity of the calculated s_j or minimizes the mutual information. In this study, we have used the fastICA

method, which use a fixed-point algorithm and the negentropy as a cost function to estimate the original signals.

5.4 Material and Methods

MRI data acquisition

Seven canine brains with spontaneous occurring brain tumors were imaged using a 3.0 Tesla GE SIGNA HDX MR scanner (GE Medical Systems, Milwaukee, WI) and a transmit/receive coil. The paramagnetic contrast agent, gadopentetate dimeglumine or Gd-DTPA, was injected intravenously as a bolus (0.2 mMol/kg) after the first acquisition pulse. The DCE-MRI protocol employed a standard T_1-weighted, 2-D gradient refocused echo sequence to obtain dynamic serial images with the following parameters: TR of 34 ms, TE of 2.78 ms, 35° flip angle, matrix size of 192×192, field of view (FOV) of 182.25 cm^2, a total of 5 slices, slice thickness of 3 mm, and NEX=1, scan time of 5.9 minutes (a total of 41 acquisitions and a temporal resolution of 8.7 seconds).

Manual segmentations by expert

The most clearly visible contrast enhanced tumor image was selected for the manual segmentation. An expert (MK, an experienced neurologist) manually traced the outline of the seven brain lesions. The size of image is 256 × 256 with a 256-gray level. In this study, we take the manual delineation by an expert as a standard reference and compared with the temporal ICA and the spatial ICA, respectively.

Segmentations using spatial ICA

In this study, we have selected the whole brain region as a mixture and assumed that there are three spatially independent components: normal brain tissue, tumor tissue, and noise. A three-source example of Eq. [5.1] can be rewritten as

$$x_i = a_{i1}s_1 + a_{i2}s_2 + a_{i3}s_3 \ , \qquad (i = 1, 2, \text{and } 3) \qquad [5.4]$$

where s_1, s_2, and s_3 are spatially independent source components, respectively. The measured mixture data x_1, x_2, and x_3 were sampled from the dynamic series at three different points in time. First, the preprocessing was performed to make x_i a zero-mean variable by centering x_i. Whitening was performed as a preprocessing by transforming the observed vector x_i linearly so that its components are uncorrelated and their variances to be unity. Then, each frame of the mixture images, x_i (i = 1, 2, and 3), was converted into a 1D row vector. The matrix form can be expressed as Eq. [5.2]

where

$$\mathbf{X} = \begin{pmatrix} x_1 \\ x_2 \\ x_3 \end{pmatrix}, \ \mathbf{A} = \begin{pmatrix} a_{11} & a_{12} & a_{13} \\ a_{21} & a_{22} & a_{23} \\ a_{31} & a_{32} & a_{33} \end{pmatrix}, \ \mathbf{S} = \begin{pmatrix} s_1 \\ s_2 \\ s_3 \end{pmatrix} \qquad [5.5]$$

The estimated independent component of the matrix form can be expressed as Eq. [5.3]

where

$$\mathbf{Y} = \begin{pmatrix} y_1 \\ y_2 \\ y_3 \end{pmatrix}, \ \mathbf{W} = \begin{pmatrix} w_{11} & w_{12} & w_{13} \\ w_{21} & w_{22} & w_{23} \\ w_{31} & w_{32} & w_{33} \end{pmatrix}, \ \mathbf{X} = \begin{pmatrix} x_1 \\ x_2 \\ x_3 \end{pmatrix} \qquad [5.6]$$

The estimated independent component can be obtained by iteratively updating the unmixing matrix **W**. Each row vector y_i is then reformed into 2D image to construct the independent component map. To differentiate between normal brain tissue and tumor tissue, we

calculated standard deviations, σ, of the background signals randomly selected from x_1 (i.e., independent component map of tumor), and then we chose the 3σ as the threshold of the background signals based on the three-sigma rule (33), which indicates that most of the signals (about 99.7%) of the background lie within three standard deviations of the mean for a normal distribution.

Segmentations using a temporal ICA

Regarding MR data, brain tissue segmentation is usually complicated by PVE because a voxel may contain two tissue types. DCE-MRI data is measured over a period of time, where a dynamic contrast-enhanced time curve is acquired from each voxel of the image. It is assumed that the observed time curve signal is a linear mixture of different source signals, e.g., tumor tissue and normal brain tissue. In a partial volume voxel, the signal intensity can be determined by the following linear mixture

$$S_{voxel} = \alpha S_A + \beta S_B \qquad [5.7]$$

where α and β are weighted coefficient, and S_A and S_B represent signal intensity of tissue A and tissue B, respectively.

In the temporal ICA of the DCE-MRI data, we have selected a region covering brain tumor as a ROI, and assumed that there are two independent components: tumor tissue and background signal that is normal brain tissue. A two-source example of Eq. [5.1] can be rewritten as

$$x_i = a_{i1}s_1 + a_{i2}s_2 \qquad (i = 1, 2) \qquad [5.8]$$

where s_1 and s_2 are temporally independent source components, respectively.

The measured mixture data x_1 was sampled from a voxel in TOI and x_2 was sampled from each voxel in entire image. The matrix form of Eq. [5.7] can be expressed as Eq. [5.2]

where

$$\mathbf{X}=\begin{pmatrix} x_1 \\ x_2 \end{pmatrix},\ \mathbf{A}=\begin{pmatrix} a_{11} & a_{12} \\ a_{21} & a_{22} \end{pmatrix},\ \mathbf{S}=\begin{pmatrix} s_1 \\ s_2 \end{pmatrix} \qquad [5.9]$$

The estimated independent component of the matrix form for a two-sample case can be expressed as Eq. [5.3]

where

$$\mathbf{Y}=\begin{pmatrix} y_1 \\ y_2 \end{pmatrix},\ \mathbf{W}=\begin{pmatrix} w_{11} & w_{12} \\ w_{21} & w_{22} \end{pmatrix},\ \mathbf{X}=\begin{pmatrix} x_1 \\ x_2 \end{pmatrix} \qquad [5.10]$$

The estimated independent component **Y** can be obtained by iteratively updating the inverse of the mixing matrix $\mathbf{W} = \mathbf{A}^{-1}$, also known as the unmixing matrix by means of statistical independent properties. We have set y_1 as a TOI signal and y_2 as a normal brain tissue signal. A mixing matrix **A** was then converted from the unmixing matrix **W** and then obtained the a_{11} map, where a_{11} is the weighting coefficient of s_1 from each voxel in the frame.

The segmentation threshold was determined based on the binary mask map created from comparing the weighting coefficient ratio between a_{11} and a_{12}. If the weighting coefficient ratio a_{11}/a_{12} of a certain voxel is greater than one, then that voxel was assigned the value of one as TOI, otherwise zero as a normal brain tissue. The final segmented TOI mask was calculated by maximizing the Pearson's correlation coefficient between the tumor sizes from an a_{11} map and a binary mask map. In this way, an incorrect assignment of the voxel at the background when the weighting coefficient ratio is close to one will be removed based on the threshold that is obtained from the Pearson's correlation coefficient with a_{11} map.

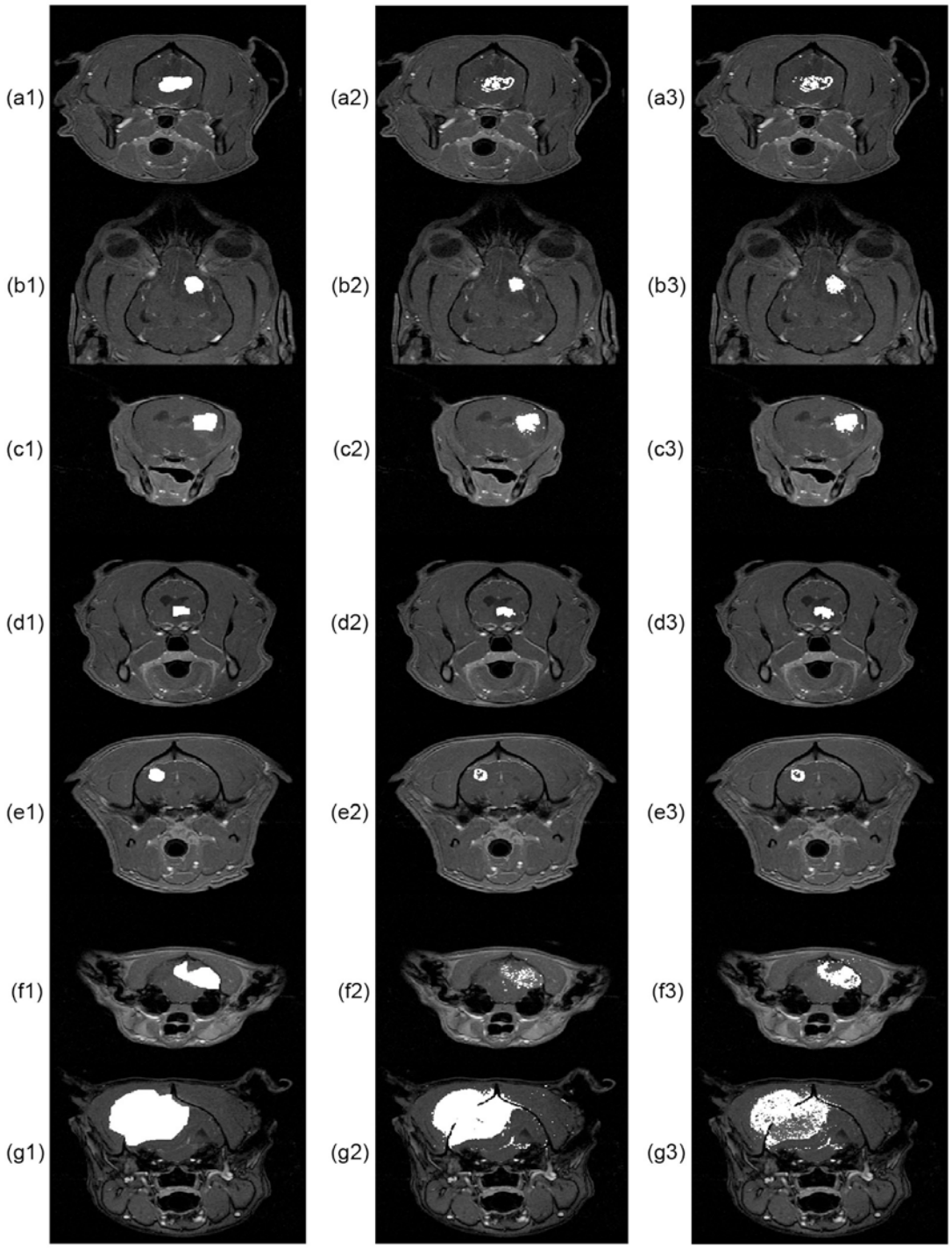

Figure 5.1 The results of each segmentation method: (a1~g1) expert's delineation segmentation, (a2~g2) spatial ICA segmentation, and (a3~g3) temporal ICA segmentation.
and Pearson correlation coefficient between two areas in size as defined in Eq. [5.13] (34).

Comparison

The segmented area estimated by the temporal ICA was compared with the area extracted by the spatial ICA. Comparison was performed based on three methods: percent volume overlap or Dice's coefficient as defined in Eq. [5.11], percent volume difference as defined in Eq. [5.12],

$$O(A_1, A_2) = \frac{A_1 \cap A_2}{\frac{1}{2}(A_1 + A_2)} \times 100\% \quad [5.11]$$

where $A_1 \cap A_2$ means an overlapped area between two regions from each method. The maximum value of 100 represents that they overlapped perfectly. It is noted that the overlap coefficient between two different areas can be slightly decreased by the spatial location shifts. We have also calculated area difference between two regions, which is insensitive to spatial shift.

$$D(A_1, A_2) = \frac{|A_1 - A_2|}{\frac{1}{2}(A_1 + A_2)} \times 100\% \quad [5.12]$$

For the identical volume size, $D(A_1,A_2)$ will have the value of zero indicating that there is no difference between two area in volume. To measure the correlation between two areas in volume size, we performed Pearson's correlation coefficient.

$$\rho(A_1, A_2) = \frac{\mathrm{cov}(A_1, A_2)}{\sigma_{A_1}\sigma_{A_2}} \quad [5.13]$$

where $\mathrm{cov}(A_1,A_2)$ is the covariance of the two areas and σ is the standard deviation.

5.5 Results

Segmentation of the lesion volumes using spatial ICA and temporal ICA were compared to an expert's manual delineation. Figure 5.1 represents the results of the manual, spatial ICA, and temporal ICA segmentation, respectively, for all seven canine objects used in this study. The first column represents the manual segmentation and the second and third columns represent the segmentations from spatial ICA and temporal ICA, respectively.

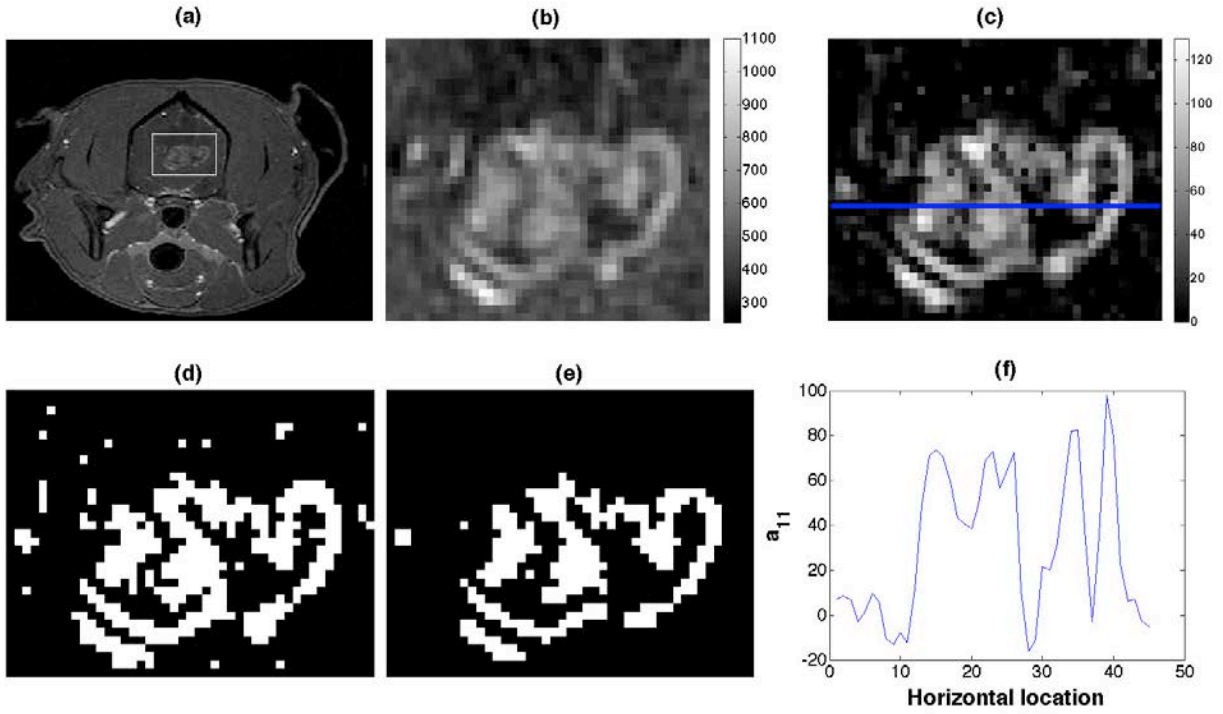

Figure 5.2 (a) Original canine brain tumor image. (b) A small frame that contains tumor and normal brain tissue. (c) a_{11} map from temporal ICA. (d) Binary map from the weighting coefficient ratio, a_{11}/a_{12}, which is bigger than 1. (e) Final segmented mask from temporal ICA. (f) a_{11} profile plot at the horizontal center of TOI showing that the values of the coefficient of tumor tissue a_{11} have high values and low values at the normal brain tissues.

Figure 5.2 shows an example of one original canine brain tumor image (a), a_{11} map (b), and binary map (c). The incorrect assignment of the voxel at the background and final segmented mask after the threshold are shown in Figure 5.1(d) and (e), respectively. Figure 5.1(f) represents a_{11} profile of the TOI at the center as a function of a_{11} value vs. horizon location in the frame. a_{11} profile plot at the horizontal center of TOI showing that the values of the coefficient of tumor tissue a_{11} have high values and low values at the normal brain tissues. The a_{11} profile of the TOI at the horizontal and vertical cross section of another two more homogeneous tumor cases are shown in Figure 5.3. It is shown that the values of a_{11} at the border between tumor and normal

brain tissues increase or decrease gradually indicating that the PVE occurs at the border of tumors. By comparing coefficients of each source (tumor or normal brain tissue), the tumor borderline can be determined from the coefficient ratio a_{11}/a_{12} of each voxel, where the values of the ratio bigger than 1 belong to tumor tissues and the values of the ratio less than 1 belong to normal tissues.

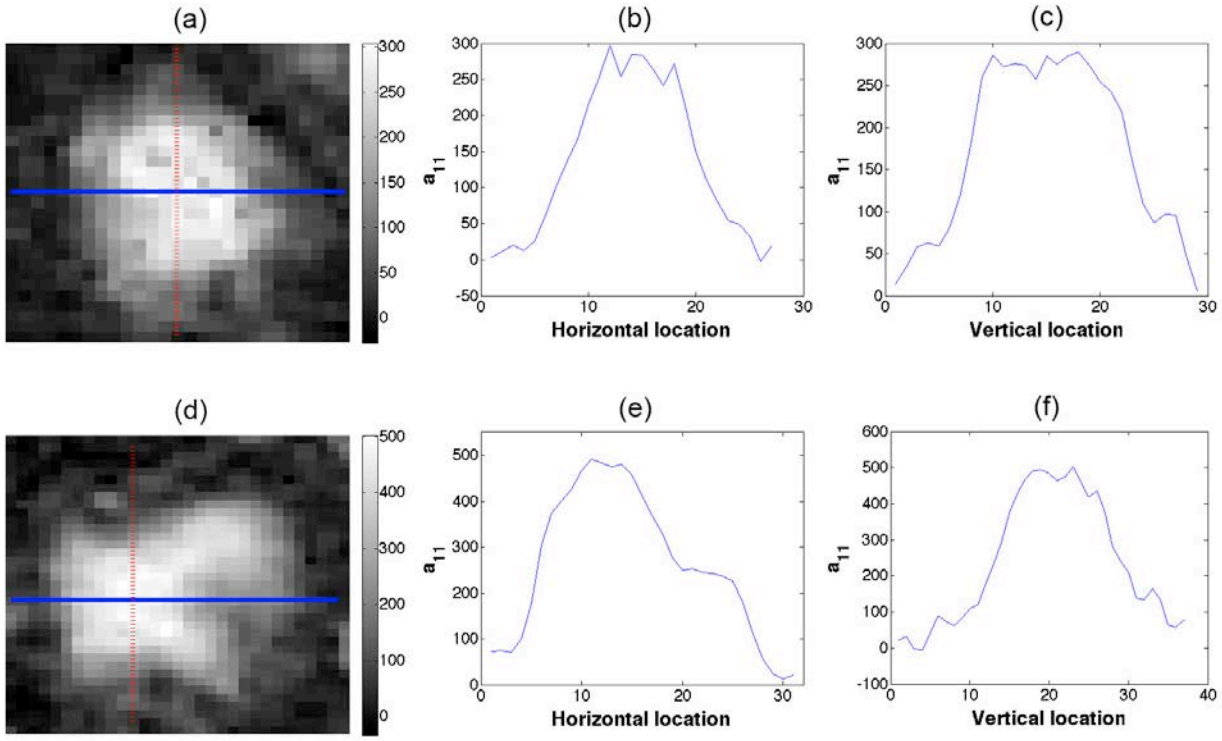

Figure 5.3 a_{11} profile plots at the horizontal and vertical cross section of TOI for dataset 2 (a~c) and dataset 3 (d~f). It is shown that the values of a_{11} at the border between tumor and normal brain tissues increase or decrease gradually indicating that the PVE occurs at the border of tumors.

Table 5.1. Segmented Area

Datasets	Segmentation Method		
	Spatial ICA (cm^2)	Temporal ICA (cm^2)	Manual (cm^2)
Data 1	1.74	1.76	2.79
Data 2	0.66	1.13	1.01
Data 3	1.04	1.02	1.09
Data 4	0.92	1.02	0.96
Data 5	0.68	0.71	1.18
Data 6	0.63	2.70	2.23
Data 7	17.84	11.62	17.47

Sizes of each segmented area are shown in Table 5.1. The differences between the automated method and expert's manual delineation are analyzed using the Pearson's correlation coefficient and summarized in Table 5.2. Pearson's correlation coefficient between the lesion areas segmented by spatial ICA and the expert's manual delineation was 0.9957 and the Pearson's correlation coefficient between the lesion areas segmented by temporal ICA and the manual delineation was 0.9937. These results indicate that the areas from each method are highly correlated without a significant difference in volume size. The Pearson's correlation coefficient

Table 5.2. Overlap (%), Difference (%), and Pearson Correlations between three methods

	sICA and Manual		tICA and Manual		sICA and tICA	
	$O(A_1,A_2)$	$D(A_1,A_2)$	$O(A_1,A_2)$	$D(A_1,A_2)$	$O(A_1,A_2)$	$D(A_1,A_2)$
Data 1	74.15	46.46	72.10	45.39	88.42	1.13
Data 2	77.64	42.58	90.45	2.39	76.59	40.29
Data 3	90.27	4.97	89.68	6.47	93.05	1.50
Data 4	85.04	3.67	81.25	13.46	90.46	17.11
Data 5	72.73	54.55	77.44	44.10	86.11	11.11
Data 6	40.55	112.14	83.62	21.83	44.82	96.19
Data 7	91.58	2.10	73.25	40.23	76.60	42.24
Mean & STD	76.00±17.33	38.07±39.63	81.11±7.34	24.84±18.30	79.44±16.57	29.94±33.68
Pearson Correlations	0.9957		0.9937		0.9844	

sICA and tICA represent spatial and temporal ICA, respectively.

between the spatial ICA and temporal ICA was 0.9844, indicating that both spatial and temporal ICA methods are highly correlated.

The results of each method were also compared using two indexes, the percent volume overlap or Dice's coefficient (Eq. [5.11]) and the percent volume difference between two regions (Eq. [5.12]). Table 5.2 summarizes these results, including the mean value and the standard deviation. The mean values of percent volume overlap and percent volume difference between spatial ICA and manual segmentation were 76.00% and 38.07%, respectively. The mean values of percent volume overlap and percent volume difference between temporal ICA and manual segmentation were 81.11% and 24.84%, respectively. Between the two ICA segmentation methods, the percent volume overlap and percent volume difference were 79.44% and 29.94%, respectively. According to these results, the overlap volume percentage between temporal ICA and manual segmentation has a slightly higher percentage rate than that between spatial ICA and manual segmentation. Meanwhile, the percent volume difference between temporal ICA and manual segmentation has a smaller percentage rate than that between spatial ICA and manual segmentation.

5.6 Discussion

DCE-MRI has been widely used in the study of tumor assessment, diagnosis, and angiogenesis. In DCE-MRI, malignant tumors show faster and higher enhancement than normal tissue. In general, no enhancement curves or slow sustained enhancement curves are typically associated with normal or benign tissues. Rapid initial and stable late enhancement curves can be classified as suspicious, and rapid initial and decreasing late enhancement curves can be classified as malignant. In this study, spatial ICA and temporal ICA methods were used for the

segmentation of canine brain tumors using spatial and temporal independency of tumor characteristics shown in the DCE-MRI data.

ICA was originally proposed to solve the blind source separation (BSS) problems and it finds the independent components by using statistical independence (35). The application of ICA has been found in many areas such as electrical recordings of brain activity as given by an electroencephalogram (EEG) device, analysis of functional MRI (fMRI), feature extraction, and medical image processing (36-38). For application of the ICA in DCE-MRI, spatial ICA was commonly used to detect and classify tissue types by assuming the spatial independence of different types of tissues. In this paper, we have used 3σ of the background signals from the independent component map of tumor as a threshold for the spatial ICA for the purpose of the segmentation, and compared results with that of manual segmentation by an expert as well as that by temporal ICA method. For temporal ICA, the segmentation threshold was determined by the mixing matrix, or equivalently, weighting coefficients of estimated source signals. The difference of the two methods is that spatial ICA can provide spatial information by separating the DCE-MRI data into physiologically meaningful components, while temporal ICA can provide temporal information from the corresponding time courses. In addition, temporal ICA is potentially capable of solving the problem of PVE, one of the major difficulties in tumor segmentation. The difficulty with PVE is that it blurs the intensity distinction at the border of the tumor and normal tissues. In a voxel with PVE (i.e., two tissues reside in one voxel), the MR signal results from both tissues and signal intensity of this voxel can be expressed as the sum of the signal from each tissue, as shown in the PVE model (Eq. [5.7]). In principle, ICA can separate this mixed signal into individual tissue signals, if they are statistically independent, to

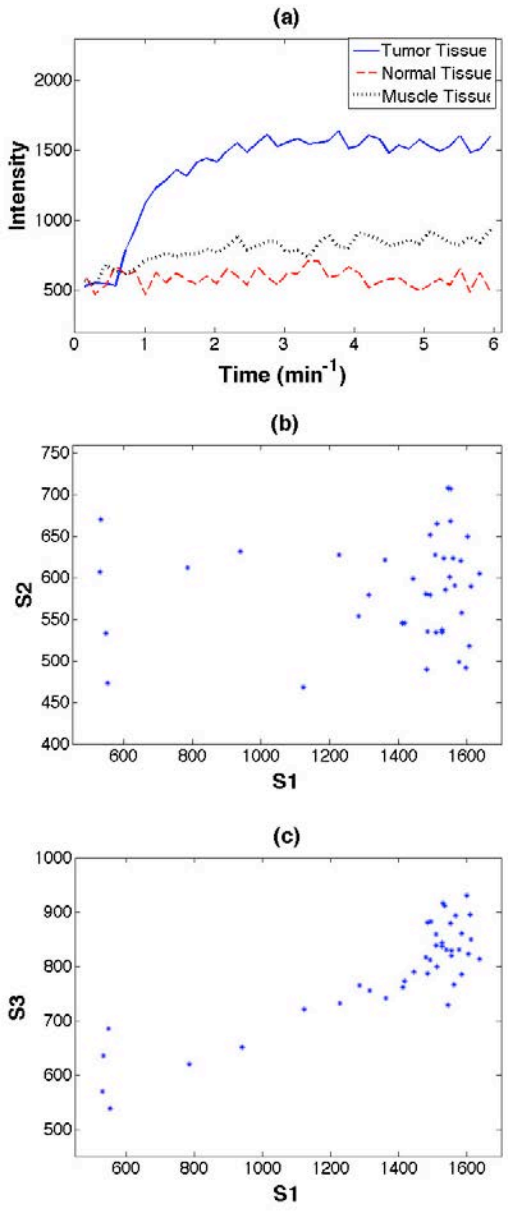

Figure 5.4 (a) Three enhancing curves from tumor, muscle, and normal brain tissues. (b) The scatter plot of the independent components S1 (tumor) and S2 (normal brain tissue). (c) The scatter plot of the independent components S1 and S3 (muscle tissue).

resolve this PVE. If the two signals do not meet the statistical independency condition, this method will likely fail.

One drawback of the temporal ICA method for segmentation is that one has to identify the actual number of source signals in advance. In this work, we have selected a small frame that only contains two different tissue types, i.e., tumor and non-tumor tissues, so that we can limit the number of source signals to two. If one needs to further segment non-tumor tissues, the number of source, *i*, should be increased in Eq. [5.8]. In this case, the size of the unmixing matrix will be $i \times i$ and this could make segmentation more difficult and current study only confirms that the number of source signals are limited to two for the feasibility of the temporal ICA segmentation. The reason for this is that the enhancing curves of tumor and muscle tissues look similar to each other and there might be some correlation between them. Figure 5.4 shows that the scatter plot of the independent components S_1 (enhancing curve from tumor) and S_2 (enhancing curve from normal brain tissue) has a small correlation coefficient (0.08±0.07) while the scatter plot of the independent component S_1 and S_3 (enhancing curve from muscle tissue) has a high correlation coefficient (0.85±0.03). Five voxels were selected from each tissue (tumor, muscle, and normal brain tissue), respectively, from data 2. Mean values and standard deviations of correlation coefficients are calculated from 25 possible pairwise combinations and listed in Table 5.3.

Table 5.3. Pearson's correlation coefficient between two enhancing time curves

	S1 – S2	S1 – S3
Pearson's correlation coefficient	0.07, 0.01, 0.19, 0.10, 0.04	0.87, 0.89, 0.89, 0.84, 0.83
	0.08, 0.04, 0.18, 0.09, 0.05	0.88, 0.89, 0.88, 0.84, 0.83
	0.06, 0.01, 0.19, 0.08, 0.05	0.86, 0.90, 0.88, 0.82, 0.82
	0.06, 0.01, 0.20, 0.11, 0.02	0.84, 0.88, 0.86, 0.78, 079
	0.08, 0.01, 0.22, 0.13, 0.02	0.86, 0.88, 0.86, 0.81, 0.82
Mean / Standard deviation	0.08 ± 0.07	0.85 ± 0.03

S1, S2, and S3 represent the independent component of the time enhancing curve from tumor, normal brain, and muscle tissue, respectively.

In summary, we have applied the temporal ICA method for the segmentation of the brain tumor using the DCE-MRI data, and conducted the spatial ICA method for segmentation as well. These two ICA methods were compared with an expert's manual delineation, which was used as a standard reference. We have shown that the performance of two ICA methods for segmenting tumor is very close to that of the expert's delineation method. For the two ICA methods, we have shown that the temporal ICA has the benefit over the spatial ICA method because of its ability of separating independent tissue signal in a voxel that contains two or more types of tissues.

5.6 References

1. Zwick S, Strecker R, Kiselev V, Gall P, Huppert J, Palmowski M, Lederle W, Woenne EC, Hengerer A, Taupitz M and others. Assessment of vascular remodeling under antiangiogenic therapy using DCE-MRI and vessel size imaging. J Magn Reson Imaging 2009;29(5):1125-33.
2. O'Connor JP, Jackson A, Parker GJ, Jayson GC. DCE-MRI biomarkers in the clinical evaluation of antiangiogenic and vascular disrupting agents. Br J Cancer 2007;96(2):189-95.
3. Jansen JF, Schoder H, Lee NY, Wang Y, Pfister DG, Fury MG, Stambuk HE, Humm JL, Koutcher JA, Shukla-Dave A. Noninvasive assessment of tumor microenvironment using dynamic contrast-enhanced magnetic resonance imaging and 18F-fluoromisonidazole positron emission tomography imaging in neck nodal metastases. Int J Radiat Oncol Biol Phys 2010;77(5):1403-10.

4. Evelhoch J, Garwood M, Vigneron D, Knopp M, Sullivan D, Menkens A, Clarke L, Liu G. Expanding the use of magnetic resonance in the assessment of tumor response to therapy: workshop report. Cancer Res 2005;65(16):7041-4.

5. Ahmed A, Gibbs P, Pickles M, Turnbull L. Texture analysis in assessment and prediction of chemotherapy response in breast cancer. J Magn Reson Imaging 2012.

6. Workie DW, Dardzinski BJ, Graham TB, Laor T, Bommer WA, O'Brien KJ. Quantification of dynamic contrast-enhanced MR imaging of the knee in children with juvenile rheumatoid arthritis based on pharmacokinetic modeling. Magn Reson Imaging 2004;22(9):1201-10.

7. Li X, Yu A, Virayavanich W, Noworolski SM, Link TM, Imboden J. Quantitative characterization of bone marrow edema pattern in rheumatoid arthritis using 3 Tesla MRI. J Magn Reson Imaging 2012;35(1):211-7.

8. Zhao Q, Lee S, Kent M, Schatzberg S, Platt S. Dynamic contrast-enhanced magnetic resonance imaging of canine brain tumors. Vet Radiol Ultrasound 2010;51(2):122-9.

9. Selnaes KM, Heerschap A, Jensen LR, Tessem MB, Schweder GJ, Goa PE, Viset T, Angelsen A, Gribbestad IS. Peripheral zone prostate cancer localization by multiparametric magnetic resonance at 3 T: unbiased cancer identification by matching to histopathology. Invest Radiol 2012;47(11):624-33.

10. Lee J, Platt S, Kent M, Zhao Q. An analysis of the pharmacokinetic parameter ratios in DCE-MRI using the reference region model. Magn Reson Imaging 2012;30(1):26-35.

11. Renz DM, Bottcher J, Diekmann F, Poellinger A, Maurer MH, Pfeil A, Streitparth F, Collettini F, Bick U, Hamm B and others. Detection and classification of contrast-

enhancing masses by a fully automatic computer-assisted diagnosis system for breast MRI. J Magn Reson Imaging 2012;35(5):1077-88.

12. Chen W, Giger ML, Lan L, Bick U. Computerized interpretation of breast MRI: investigation of enhancement-variance dynamics. Med Phys 2004;31(5):1076-82.

13. Clark MC, Hall LO, Goldgof DB, Velthuizen R, Murtagh FR, Silbiger MS. Automatic tumor segmentation using knowledge-based techniques. IEEE Trans Med Imaging 1998;17(2):187-201.

14. Kaus MR, Warfield SK, Nabavi A, Chatzidakis E, Black PM, Jolesz FA, Kikinis R. Segmentation of meningiomas and low grade gliomas in MRI. Medical Image Computing and Computer-Assisted Intervention, Miccai'99, Proceedings 1999;1679:1-10.

15. Chen W, Giger ML, Bick U. A fuzzy c-means (FCM)-based approach for computerized segmentation of breast lesions in dynamic contrast-enhanced MR images. Acad Radiol 2006;13(1):63-72.

16. Liney GP, Sreenivas M, Gibbs P, Garcia-Alvarez R, Turnbull LW. Breast lesion analysis of shape technique: semiautomated vs. manual morphological description. J Magn Reson Imaging 2006;23(4):493-8.

17. Gerig G, Styner M, Chakos M, Lieberman JA. Hippocampal shape alterations in schizophrenia: Results of a new methodology. Schizophrenia Research 2002;53(3):102-103.

18. Yoo SS, Gil Choi B, Han JY, Hee Kim H. Independent component analysis for the examination of dynamic contrast-enhanced breast magnetic resonance imaging data: preliminary study. Invest Radiol 2002;37(12):647-54.

19. Koh TS, Thng CH, Ho JT, Tan PH, Rumpel H, Khoo JB. Independent component analysis of dynamic contrast-enhanced magnetic resonance images of breast carcinoma: a feasibility study. J Magn Reson Imaging 2008;28(1):271-7.

20. Mehrabian H, Chopra R, Martel AL. Calculation of Intravascular Signal in Dynamic Contrast Enhanced-MRI Using Adaptive Complex Independent Component Analysis. IEEE Trans Med Imaging 2013;32(4):699-710.

21. Martel AL, Chan RW, Ramsay E, Plewes DB. Removing undersampling artifacts in DCE-MRI studies using independent components analysis. Magn Reson Med 2008;59(4):874-84.

22. Wu XY, Liu GR. Application of independent component analysis to dynamic contrast-enhanced imaging for assessment of cerebral blood perfusion. Med Image Anal 2007;11(3):254-65.

23. Bell AJ, Sejnowski TJ. An information-maximization approach to blind separation and blind deconvolution. Neural Comput 1995;7(6):1129-59.

24. Cardoso J-F, Souloumiac A. Blind beamforming for non-Gaussian signals. 1993. IET. p 362-370.

25. Hyvarinen A. Fast and robust fixed-point algorithms for independent component analysis. IEEE Trans Neural Netw 1999;10(3):626-34.

26. Kumazawa S, Yoshiura T, Honda H, Toyofuku F, Higashida Y. Partial volume estimation and segmentation of brain tissue based on diffusion tensor MRI. Med Phys 2010;37(4):1482-90.

27. Carroll TJ, Haughton VM, Rowley HA, Cordes D. Confounding effect of large vessels on MR perfusion images analyzed with independent component analysis. American journal of neuroradiology 2002;23(6):1007-1012.

28. Su KH, Lee JS, Li JH, Yang YW, Liu RS, Chen JC. Partial volume correction of the microPET blood input function using ensemble learning independent component analysis. Phys Med Biol 2009;54(6):1823-46.

29. McKeown MJ, Jung TP, Makeig S, Brown G, Kindermann SS, Lee TW, Sejnowski TJ. Spatially independent activity patterns in functional MRI data during the stroop color-naming task. Proc Natl Acad Sci U S A 1998;95(3):803-10.

30. Chen H, Yao D, Zhuo Y, Chen L. Analysis of fMRI data by blind separation of data in a tiny spatial domain into independent temporal component. Brain Topogr 2003;15(4):223-32.

31. Hyvarinen A, Oja E. Independent component analysis: algorithms and applications. Neural Netw 2000;13(4-5):411-30.

32. Abell JL, Lee J, Zhao Q, Szu H, Zhao Y. Differentiating intrinsic SERS spectra from a mixture by sampling induced composition gradient and independent component analysis. Analyst 2012;137(1):73-6.

33. Mendenhall W, Scheaffer RL, Wackerly DD. Mathematical statistics with applications. Duxbury Press Boston; 1981.

34. Dice LR. Measures of the amount of ecologic association between species. Ecology 1945;26(3):297-302.

35. Comon P. Independent Component Analysis, a New Concept. Signal Processing 1994;36(3):287-314.

36. Attias H. Independent factor analysis. Neural Comput 1999;11(4):803-51.

37. McKeown MJ, Sejnowski TJ. Independent component analysis of fMRI data: examining the assumptions. Hum Brain Mapp 1998;6(5-6):368-72.

38. Hao J, Zou X, Wilson MP, Davies NP, Sun Y, Peet AC, Arvanitis TN. A comparative study of feature extraction and blind source separation of independent component analysis (ICA) on childhood brain tumour 1H magnetic resonance spectra. NMR Biomed 2009;22(8):809-18.

CHAPTER 6

CONCLUSIONS

The primary purpose of the studies discussed in this dissertation was to develop new methodologies in both quantification and segentation of brain tumors in DCE-MRI. Specifically, the first study introduced new pharmacokinetic parameter ratios, K_R and V_R, to overcome the problem that the traditional reference region model requires literature values of pharmacokinetic parameters of reference region tissues; the second study presented an analytical approach to reduce systematic errors caused by traditional numerical analysis; lastly, the third study introduced temporal ICA algorithm to resolve partial volume effect (PVE) in the studies of the segmentation of brain tumors.

6.1 An analysis of the pharmacokinetic parameter ratios in DCE-MRI

The reference region model has been used to estimate the pharmacokinetic parameters without the information of AIF. However, the original RR method sometimes generates systematic errors in estimating the kinetic parameters with incorrect assignments of the parameters for the reference regions. To improve the reference region model approach, the new pharmacokinetic parameter ratios, K_R and V_R, between tissue of interest (TOI) and RR were introduced in this study. The results from both simulation and in vivo studies of canine brain lesions revealed that the ratios are independent of $K^{trans,RR}$, implying that acquiring the information about literature values from reference regions may not be needed for future

pharmacokinetic modeling. Kruskal-Wallis test and Kolmogorov-Smirnov test were conducted to determine whether any two lesions differed significantly. According to the statistical tests, there is a significant difference between any two given data distributions. These results may potentially assist physicians in the differentiation of tumor histopathology and correlate them with the pharmacokinetic parameter ratios K_R and V_R. A potential problem of the proposed method is that the regression model for the reference region data cannot fit the R_1 curve in the TOI well, when the R_1 curves of the TOI and the reference region do not follow the same trend (one increasing while the other one decreasing). This is likely due to the cases when the TOI and reference regions do not share the same artery for blood supply. In this case, the kinetic parameter ratios will fail to represent the true information. Additionally, future studies are needed to verify the correlation between tumor histopathology and the pharmacokinetic parameter ratios K_R and V_R.

6.2 Analytical vs. Numerical analysis of DCE-MRI

In this study, we compared three different methods, LLSQ-N, NLSQ-N, and NLSQ-A, for the analysis of the kinetic parameter ratios, K_R and V_R . As we have shown from our simulation studies , the numerical methods produce a systematic error with various temporal resolutions while the analytical method does not. A regression analysis was used for the NLSQ-A method; however, this regression model requires the proper form of the AIF for the TOI and RR in order to accurately estimate the kinetic parameter ratio K_R and V_R . In the simulation study, the biexponential AIF form was generated based on a low-molecular-weight contrast agent, gadolinium diethylenetriamine pentaacetic acid (Gd-DTPA), which is in widespread clinical use. The regression analysis was used to find the regression model (Eq. [4-11]) based on this

biexponential form. However, this model would not be appropriate for analyses using other contrast agents; in other words, finding the proper model is essential.

To summarize, The NLSQ-A method of estimating pharmacokinetic parameter ratios K_R and V_R was found to be more accurate than the numerical methods in that the latter methods created systematic errors over various temporal resolutions and SNRs.

6.3 Tumor Segmentation using temporal ICA for DCE-MRI

In this study, temporal ICA was introduced to segment canine brain tumor in DCE-MR images. In medical images, PVE occurs when more than one tissue type is present in the same voxel, and this blurs the intensity distinction at the border of two tissues such as the tumor and normal tissues. In the studies of tumor segmentation using MR data, PVE is one of the major difficulties that may result in inaccurate segmentation due to inherent low spatial resolution of images. The MR signal intensity of a voxel with two tissues can be expressed as the sum of the signal from each tissue (Eq. [5-7]). If the two tissue signals are statistically independent, then the ICA can resolve this PVE.

Additionally, we conducted the spatial ICA method for segmentation. The temporal and spatial ICAs were compared with an expert's manual delineation as the standard reference. It was demonstrated that although the performance of the two ICA methods for segmenting tumor is very close to that of the expert's delineation method, the temporal ICA has the advantage over the spatial ICA method in its ability to separate independent tissue signals in a voxel with PVE. One potential problem of the temporal ICA method for segmentation is that one has to identify the actual number of source signals in advance. In this study, we have selected a small ROI that only contains two different tissue types, i.e., tumor and non-tumor tissues, so that we can limit

the number of source signals to two. The reason for this is that the enhancing curves of tumor and muscle tissues look similar to each other and there might be some correlation between them.

In conclusion, the studies presented in this dissertation may potentially contribute to DCE-MRI field by introducing new parameter ratios to improve the reference region model, and by introducing the analytical method for analysis of DCE-MRI data. Also, temporal ICA was introduced to solve PVE in brain tumor segmentation.